SEARCH FOR NEW PHYSICS IN THE COMPACT MUON SOLENOID (CMS) EXPERIMENT AND THE RESPONSE OF THE CMS CALORIMETERS TO PARTICLES AND JETS

by

KAZIM ZIYA GUMUS

A DISSERTATION

IN

PHYSICS

Submitted to the Graduate Faculty
of Texas Tech University in
Partial Fulfillment of
the Requirements for
the Degree of

DOCTOR OF PHILOSOPHY

Approved

Nural Akchurin
Committee Chair

Walter Borst

M. A. K. Lodhi

Richard Wigmans

Accepted

Fred Hartmeister
Dean of Graduate School

August, 2008

ACKNOWLEDGEMENTS

I would like to thank my dear supervisor Nural Akchurin for his precious guidance and support during this study. It was pleasure for me to be his student and to work with him. He has been not only a mentor to me but also a model scientist to imitate.

I am grateful to Robert Harris for his supervision and teachings in dijets study. It was joy to collaborate with him and to benefit from his expertise.

I would like to thank Richard Wigmans for his invaluable guidance in the test beam study. The daily meetings we had for almost a year gave me a chance to learn a lot from him, and I greatly admired and appreciate his vast expertise.

I also would like to thank Heejong Kim for being an older brother to me during my study, helping me with technical problems. I acknowledge his collaborative contribution to the test beam study.

I am thankful to Alan Sill for his efforts to provide us with better computational opportunities and to the TTU HPCC group for their valuable technical assistance.

I would like to thank my other dissertation committee members: Arfin Lodhi, Walter Borst, Beth Thacker, and Hamed Sari-Sarraf for their valuable comments on my dissertation.

Special thanks to old and new TTU HEP group members: Sung-Won, Igor, Jack, Mario, Lin, Kenneth, Ray, Lisa, Efe, Sorina, Chiyoung, Youn, Mohammad, George, and Brian for the valuable discussions we had and all kinds of support they provided me.

My deepest gratitude is to my dear father Müslüm and mother Yeter, my brother İbrahim, and sister Arzu for their unconditional love and encouragement throughout my life. Last, but not least, thanks to my family: my beloved wife Hülya for sharing this journey with me and making it enjoyable and my two-year-old daughter Büşra Naz for being the joy of my life.

CONTENTS

ABSTRACT

A Monte Carlo study of a generic search for new resonances beyond the Standard Model (SM) in the CMS experiment is presented. The resonances are axigluon, coloron, E_6 diquark, excited quark, W', Z', and the Randall-Sundrum graviton which decay to dijets. The dijet resonance cross section that the CMS can expect to discover at a 5σ significance or to exclude at 95% confidence level for integrated luminosities of 100 pb^{-1}, 1 fb^{-1}, and 10 fb^{-1} is evaluated. It is shown that a 5σ discovery of a multi-TeV dijet resonance is possible for an axigluon, excited quark, and E_6 diquark. However, a 5σ discovery can not be projected with confidence for a W', Z' and the Randall-Sundrum graviton. On the other hand, 95% CL exclusion mass regions can be measured for all resonances at high luminosities. In the second part of this dissertation, the analyses of the 2006 test beam data from the combined electromagnetic and hadronic barrel calorimeters are presented. The CMS barrel calorimeters' response to a variety of beam particles in a wide momenta range (1 to 350 GeV/c) is measured. Furthermore, using these beam data, the expected performance of the barrel calorimeters to jets is predicted.

LIST OF TABLES

LIST OF FIGURES

CHAPTER 1
INTRODUCTION

"Everything should be made as simple as possible but not simpler."

Anonymous

The Standard Model (SM) is the current theory of quarks and leptons and their electromagnetic, weak, and strong interactions. However, it is not a complete theory because it has left many important questions unanswered: Why do quarks come in different flavors? Why are the quarks arranged in generations? Why are there four different forces? How do we unify gravitation with the other forces? Why is gravity so weak?

There are new theories that try to address these questions. As these theories attempt to answer these questions, they often predict extremely short-lived particles called "resonances." Theoretical ideas behind the concepts of technicolor and extended technicolor attempt to explain the reason and origin for different quark flavors. They predict two new resonances named "color octet technirho" and "coloron." Compositeness explains the reason behind quark families by proposing a composite structure for quarks and postulates the existence of excited quarks. Grand unified theories address the question "Why are there different forces?" and in doing so, require new heavy Z and W bosons. The unification of gravity with other fundamental forces is generally dealt with by string theories. Some superstring models predict that at low energies the SM originates from the E_6 gauge group that contains diquarks. The theory of extra dimensions attempts to explain the reason why gravity is so weak. It postulates that the strength of gravity is reduced by leaking into an extra dimension and predicts a new particle called "graviton."

This dissertation contains two major studies. The first one is a Monte Carlo study of these new particles in the Compact Muon Solenoid (CMS) experiment at the Large Hadron Collider (LHC). The LHC will collide protons at 14 TeV center-of-mass

energy, that is seven times larger than what exists today at the Tevatron at Fermilab. I estimate the CMS sensitivity to these new resonances when they decay into two jets (dijets). In the second study, I present my analysis of 2006 CMS combined (electromagnetic and hadronic) calorimeter test beam data. This analysis highlights the combined calorimeter response to a variety of particles from 1 to 350 GeV/c. I also extend this analysis to jets by using the test beam data. I present the CMS calorimeter response to jets from 10 GeV to 4 TeV.

CHAPTER 2
MODELS AND CALCULATIONS

In this chapter, the details of the resonance models and their lowest order cross section values are presented [1]. The resonance properties are summarized in Table 2.1, and the cross sections are listed in Tables 2.3 and 2.4. Fig. 2.7 shows the relative cross section of the narrow dijet resonances. The code that calculates the lowest order cross section values for the models was developed by the CDF collaboration [2]. The cross section calculations were carried out using the CTEQ6L parton distributions [3] from LHAPDF [4].

Name	Symbol	Spin Parity (J^P)	Color Multiplet	$\Gamma/(2M)$	Channel
Axigluon	A	axial-vector (1^+)	octet	0.05	$q\bar{q}$
Coloron	C	vector(1^-)	octet	0.05	$q\bar{q}$
Excited Quark	q^*	fermion ($1/2^+$)	triplet	0.02	qg
Octet Technirho	ρ_{T8}	vector (1^-)	octet	0.01	$q\bar{q}, gg$
E_6 Diquark	D	scalar (0^+)	triplet	0.004	ud
Heavy W	W'	vector (1^-)	singlet	0.01	$q_1\bar{q}_2$
Heavy Z	Z'	vector (1^-)	singlet	0.01	$q\bar{q}$
RS Graviton	G	tensor (2^-)	singlet	0.01	$q\bar{q}, gg$

Table 2.1: Properties of dijet resonances are summarized.

2.1 Axigluons

Chiral color, proposed by Frampton and Glashow [5], is an alternative theory to SM. In chiral color, the unbroken color symmetry $SU(3)_C$ of QCD results from the breaking of the larger chiral color group $SU(3)_L \times SU(3)_R$. One prediction of the chiral color model is the existence of the axigluon particle: a massive color-octet axial vector gluon. Axigluons are produced and decay strongly from quark-antiquark interactions, giving one of the largest cross section times branching ratio of any of the models considered. Fig. 2.1 shows the Feynman diagram for axigluons.

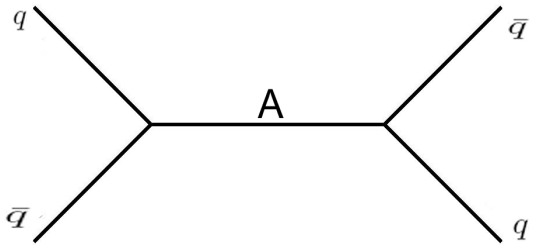

Figure 2.1: The Feynman diagram for an axigluon. It is produced from quarks and decays into quarks.

2.1.1 The Axigluon Lagrangian

The axigluon is constrained by gauge invariance to couple to all quark flavors according to the following interaction lagrangian [6]:

$$\mathcal{L}_A = -ig_s t^a_{ij} \bar{q}^i \gamma_5 \gamma_\mu A^{\mu a} q^j \tag{2.1}$$

where t^a_{ij} are the SU(3) color matrices. The axigluon cannot decay into two gluons because of parity conservation.

2.1.2 The Width and Branching Ratio

The width of the axigluon is given by [7]:

$$\Gamma_A = \frac{N_A \alpha_s M_A}{6} \tag{2.2}$$

where N_A counts the number of open decay channels, the number of quarks with mass less than the $M_A/2$. We will assume a SM version of axigluons in which $N_A = 5$ when the axigluon has a mass less than twice the top quark mass ($2M_t$) and $N_A = 6$ when the axigluon has a mass greater than $2M_t$ but less than a TeV. With this assumption, $\Gamma_A/2 \approx .05 M_A$. When $M_A < 2M_t$, the branching ratio to light quarks (u, d, s, c, b) is 1, and when $M_A > 2M_t$, the branching ratio is taken to be [6]:

$$BR(A \to q\bar{q}) = \frac{1}{5 + [1 - (2M_t/M_A)^2]^{3/2}} \tag{2.3}$$

2.1.3 The Axigluon Cross Section

The total cross section for axigluon production is given by integrating the differential cross section

$$\sigma = \int_{y^{min}}^{y^{max}} \frac{16\pi^2\alpha_s}{9s} L(x_p, x_{\bar{p}}) A(y, y_{cut}, \cos\theta^*_{cut}) dy \tag{2.4}$$

where the minimum rapidity is $y^{min} = \max(-y_{cut}, \ln\sqrt{\tau})$, the maximum rapidity is y^{max}=$\min(y_{cut}, -\ln\sqrt{\tau})$, and $\tau = M^2/s = x_p x_{\bar{p}}$. The parton luminosity is given by

$$L(x_p, x_{\bar{p}}) = \sum_i (q_i(x_p)\bar{q}_i(x_{\bar{p}}) + \bar{q}_i(x_p) q_i(x_{\bar{p}})) \tag{2.5}$$

and $A(y, y_{cut}, \cos\theta^*_{cut})$ is the acceptance for our jet rapidity and $\cos\theta^*$ cut which is evaluated at each value of y within the integral using the axial-vector decay angular distribution:

$$\frac{dN}{d\cos\theta^*} = 1 + \cos^2\theta^* \tag{2.6}$$

where θ^* is the scattering angle in the dijet center of mass frame and defined as

$$\cos\theta^* = |\tanh(\eta_1 - \eta_2)/2|. \tag{2.7}$$

This cross section is then multiplied by Eq. 2.3 to obtain the cross section times branching ratio presented in Table 2.4.

2.2 Colorons

The flavor-universal coloron model [8] is another approach to the explanation of different quark flavors. It proposes that the strong gauge group is extended to $SU(3)_1 \times SU(3)_2$. The original gauge bosons from each $SU(3)$ mix to form a color octet of massless gluons and a color octet of massive gluons that are called "colorons." The gluons interact with quarks through a conventional QCD coupling with strength

g_s. The colorons ($C^{\mu a}$) interact with quarks through a new QCD-like coupling

$$\mathcal{L} = -g_3 \cot\theta J^a_\mu C^{\mu a} \tag{2.8}$$

and where J^a_μ is the color current

$$\sum_f \bar{q}_f \gamma_\mu \frac{\lambda^a}{2} q_f \tag{2.9}$$

where θ is the mixing angle of the two $SU(3)$. The colorons decay to all sufficiently light quarks; assuming there are n flavors lighter than $M_c/2$, the decay width is given below:

$$\Gamma_c \approx \frac{n}{6}\alpha_s \cot^2\theta\, M_c. \tag{2.10}$$

Colorons are produced from quarks and decay to quarks similar to axigluon as in Fig. 2.1. The flavor universal coloron is thus a massive gluon that couples equally to all quarks. It is apparent that for the value of mixing $\cot\theta = 1$, the coloron has the same width as the axigluon, the same coupling strength to quarks as the axigluon, and the same production cross sections times branching ratio for jets. This follows from the similarity of the axial-vector and vector interactions, as noted in reference [8]. Thus, in our search, we use the axigluon cross section discussed in the previous section for colorons, as well.

2.3 E_6 Diquarks

The superstring theory employs both supersymmetry and string theories and attempts to unify gravity with the other fundamental forces. It requires 10 dimensions, 6 of which are compactified. The superstring model predicts that at low energies the SM originates from the E_6 gauge group that contains diquarks. A diquark is an hypothetical state of two quarks grouped inside a baryon. The E_6 diquarks are color triplet and scalar $D(D^c)$ and they carry $-1/3(+1/3)$ charge. They couple to $\bar{u}\bar{d}(ud)$. Fig. 2.2 shows the Feynman diagram for E_6 diquarks.

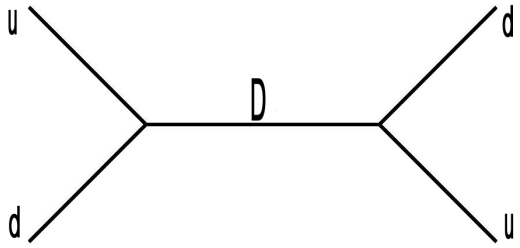

Figure 2.2: The Feynman diagram for an E_6 diquark. It is produced from and valence u and d quarks and decay into them.

2.3.1 The E_6 Diquark Lagrangian

The interaction lagrangian for transitions between E_6 diquarks and up and down quarks is [9]:

$$\mathcal{L}_D = \lambda\epsilon_{ijk}\bar{u}^{ci}\frac{1-\gamma_5}{2}d^j D^k + \frac{\lambda_c}{2}\epsilon_{ijk}\bar{u}^i\frac{1+\gamma_5}{2}d^{cj}D^{ck} + h.c. \tag{2.11}$$

where it is commonly assumed that the unknown couplings are of electromagnetic strength ($\lambda = \lambda_c = e$) and that the masses are degenerate ($M_{D^c} = M_D$).

2.3.2 The E_6 Diquark Width and Branching Ratio

Assuming electromagnetic-strength Yukawa couplings, the width of the E_6 diquarks is given by [9]:

$$\Gamma_D = \alpha M_D, \qquad \Gamma_{D^c} = \alpha M_{D^c}/4 \tag{2.12}$$

where $\alpha = \lambda^2/4\pi$ is the electromagnetic coupling constant, which is 1/128 after running to high masses. E_6 diquarks in the first family decay into u and d quarks only.

2.3.3 The E_6 Diquark Cross Section

The E_6 diquark cross section is obtained from integrating the subprocess differential cross sections over the Breit-Wigner resonance. Following reference [9], the

differential cross section for D is given by:

$$\frac{d^2\sigma}{dx_p dx_{\bar{p}}} = \frac{\hat{s}}{108\pi}\frac{16\lambda}{(\hat{s}-M_D^2)^2+\Gamma_D^2 M_D^2}[\bar{u}(x_p)\bar{d}(x_{\bar{p}})+\bar{u}(x_{\bar{p}})\bar{d}(x_p)]P \tag{2.13}$$

and similarly for $\bar{D}$ with $\bar{q} \to q$ in the parton distributions. The cross section for D^c is given by

$$\frac{d^2\sigma}{dx_p dx_{\bar{p}}} = \frac{s_h at}{108\pi}\frac{\lambda}{(\hat{s}-M_{D^c}^2)+\Gamma_{D^c}^2 M_{D^c}^2}(u(x_p)d(x_{\bar{p}})+u(x_{\bar{p}})d(x_p))P \tag{2.14}$$

and similarly for $\bar{D^c}$ with $q \to \bar{q}$ in the parton distributions. In Eqs. 2.13 and 2.14, $\hat{s} = sx_{\bar{p}}x_p$ and the variable P is the kinematic acceptance. In this equation, the kinematic acceptance is

$$P = P(y^{cut}, cos\theta^*) \tag{2.15}$$

which is the probability that both final state partons pass our cuts in rapidity and $cos\theta^* = \tanh(y^*) = \tanh(y_1 - y_2)$ as a function of the variable y_b.

2.4 Excited Quarks

If quarks are composite particles, then excited states are expected. Excited quarks are produced when a ground state quark absorbs a gluon, then returns to the ground state, emitting a gauge boson. As in reference [10], we only consider the simplest kind of excited quark, one with spin 1/2 and isospin 1/2. Fig. 2.3 shows the Feynman diagram for excited quarks.

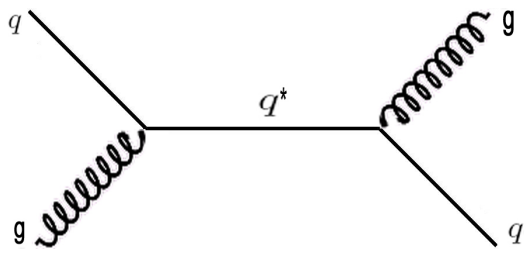

Figure 2.3: The Feynman diagram for an excited quark. A quark goes to an upper state by absorbing a gluon and returns to the ground state by emitting a gauge boson. The gauge boson is a gluon about 80% of the time [10].

2.4.1 The Excited Quark Lagrangian

The Lagrangian for transitions between an excited quark of mass M^* and a quark plus a gauge boson ($q^* \leftrightarrow q + [\gamma, g, W, Z]$) is given as [10]:

$$\mathcal{L} = \frac{1}{2M^*}\bar{q}^*_R\sigma^{\mu\nu}(g_s f_s \frac{\lambda_a}{2}G^a_{\mu\nu} + gf\frac{\tau}{2}W_{\mu\nu} + g'f'\frac{Y}{2}B_{\mu\nu})q_L + h.c. \tag{2.16}$$

where $G^a_{\mu\nu}$, $W_{\mu\nu}$, and $B_{\mu\nu}$ are the field-strength tensors of the gluon, the SU(2) and the U(1) are the gauge fields, $Y = 1/3$ is the weak hypercharge, and g_s, g, and g' are the gauge coupling constants. Finally f_s, f, and f' are unknown deviations of the couplings from their SM values, determined by the composite dynamics, and are all assumed to be equal to one, corresponding to no deviation from the SM.

2.4.2 The Excited Quark Width and Branching Ratios

Production of a single excited quark will take place in hadronic collisions via quark gluon fusion. The excited quark can then decay into a quark and any gauge boson. The relative decay rates [10] are listed in Table 2.2, assuming SM couplings.

Decay Mode	Br. Ratio(%)	Decay Mode	Br. Ratio(%)
$u^* \to ug$	83.4	$d^* \to dg$	83.4
$u^* \to u\gamma$	2.2	$d^* \to d\gamma$	0.5
$u^* \to dW$	10.9 ($e\nu$ 1.2)	$d^* \to uW$	10.9
$u^* \to uZ$	3.5 (ee .27)	$d^* \to dZ$	5.1

Table 2.2: The decay modes and branching ratios of excited up and down quarks for $f_s = f = f'$ and $\alpha_s = 0.1$.

Expressions for the partial decay rates are given in reference [10]. The q^* half-width for $f_s = f = f'$ is approximately given by

$$\frac{\Gamma(q^*)}{2} \approx 0.02 f^2 M^* \tag{2.17}$$

which for $f \leq 1$ is significantly narrower than our dijet mass resolution.

2.4.3 The Excited Quark Cross Section Calculation

The q^* total cross section is obtained by first explicitly calculating the Breit-Wigner differential cross section versus dijet mass, m, and then integrating over m. Following reference [10], the differential cross section is given by

$$\frac{d\sigma}{dm} = \frac{2}{m}\int_{y_b^{min}}^{y_b^{max}} dy_b\ \tau\mathcal{L}(x_1,x_2)\ \hat{\sigma}(m^2)\ P. \tag{2.18}$$

Here, τ is related to the initial state parton fractional momenta x_1 and x_2 by $\tau = x_1x_2 = m^2/s$. The kinematic variable y_b is given by $y_b = (y_{JET1} + y_{JET2})/2 = (1/2)\ln(x_1/x_2)$, and rapidity y and pseudorapidity η are equal because massless partons are assumed. The partonic "luminosity function" is just the product of parton distribution function:

$$\mathcal{L}(x_1,x_2) = q(x_1,m^2)g(x_2,m^2) + g(x_1,m^2)q(x_2,m^2). \tag{2.19}$$

Reference [10] states that "u^* and d^* should, to a good approximation, be degenerate in mass," and therefore the quark structure function is given by the sum of up, down, anti-up, and anti-down parton distributions: $q = u + d + \bar{u} + \bar{d}$. We used CTEQ6L [3] parton distributions.

The subprocess cross section is given by the following Breit-Wigner like resonance formula for an excited quark of mass M^*

$$\hat{\sigma}(m^2) = \pi\frac{\hat{\Gamma}^2(qg\to q^*)\hat{\Gamma}(q^*\to qg)}{(m^2-M^{*2})^2 + \hat{\Gamma}^2(q^*)M^{*2}} \tag{2.20}$$

where $\hat{\Gamma}(q^*)$, is the full width of the q^* resonance from all decay channels, and $\hat{\Gamma}(qg\to q^*)$ is approximately the partial width in the qg channel. The final variable P in Eq. 2.18 is the probability that both final state particles pass our cuts in rapidity and P_T as a function of the variables τ and y_b.

2.5 Color Octet Technirhos

Color octet technirhos exist in models of either extended technicolor or topcolor-assisted technicolor [12]. Tecnicolor is a model based on dynamical electroweak symmetry breaking. It attempts to explain W and Z gauge boson masses without a scalar Higgs field. Instead, it employs technipions, which is a bound state of two technifermions. Topcolor-assisted technicolor replaces tehnipions with a top and anti-top quark pair to explain electroweak symmetry breaking. Extended technicolor introduces new gauge bosons to explain masses of quarks and leptons. Both extended technicolor and topcolor-assisted technicolor models propose a color octet technimeson called "technirho," which is expected to be discovered at the LHC if it exists. Color octet technirhos are produced via a vector-meson dominance model of mixing between the gluon and the color octet technirho ($q\bar{q}, gg \rightarrow g \rightarrow \rho_{T8}$). This mixing has the effect of reducing the cross section from what is expected for a normal color interaction, for example from axigluons or colorons. This mixing also moves the mass of the resonance value by a few percent, making the mean observed $\sqrt{\hat{s}}$ of any color octet technirho resonance always at least a few percent higher than the pole mass. Fig. 2.4 shows the Feynman diagram for color octet technirho.

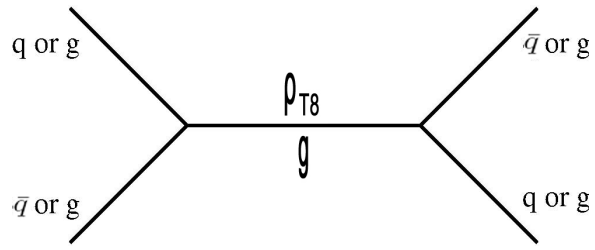

Figure 2.4: The Feynman diagram for a technirho. The initial state contains either quarks or gluons. The intermediate state contains a mix of a color octet technirho with gluon. In the final state, technirho decays to quarks or gluons.

PYTHIA 6.321 was used to simulate the lowest order cross section at the generator level for color octet technirhos decaying to dijets. The process is always simulated in the presence of QCD background because the color octet ρ is only produced by mixing with the s-channel gluon of the QCD background process. Two outgoing

partons (jets) are required to be central ($|\eta| < 1$). This gives the total resonance cross section as a function of the mean mass $M = \sqrt{\hat{s}}$, as shown in (Table 2.3).

M(pole) (GeV)	M (GeV)	Cross Section (pb)	Error (pb)
500	525	1.16E+03	3.3E+01
700	733	2.58E+02	7.4E+00
1000	1045	5.03E+01	1.4E+00
1500	1565	7.18E+00	1.9E-01
2000	2086	1.55E+00	4.2E-02
3000	3121	1.41E-01	4.0E-03
4000	4155	1.79E-02	5.6E-04
5000	5192	2.36E-03	9.1E-05
6000	6224	3.02E-04	1.5E-05
7000	7275	4.22E-05	2.5E-06
8000	8318	5.77E-06	3.6E-07

Table 2.3: The cross section for Color Octet Technirhos decay into dijets in $|\eta| < 1$. As a function of the pole mass, the mean mass of the resonance, $M = \sqrt{\hat{s}}$, the cross section for the resonance decaying into two partons, each in the region $|\eta| = 1$, and the statistical error on that cross section are tabulated.

2.6 W' and Z'

The sequential SM extends SM in an attempt to unify the fundamental forces. It proposes new quarks, leptons, and gauge bosons that are sequential replicas of the known ones. The additional Z' and W' are similar to the SM Z and W except that they are heavier. We calculate cross sections for the W' and Z' of the sequential standard model. We assume that the W' has the same production cross section as the W (with M_W replaced by $M_{W'}$) and the same fractional width as the W. The same relations holds between the Z' and the Z. Fig. 2.5 shows the Feynman diagram for W' and Z'.

We use the subprocess cross section expression for W and Z production in [14] with the Fermi constant, G_F, replaced by

$$G'_F = G_F(\frac{M}{M'})^2 \tag{2.21}$$

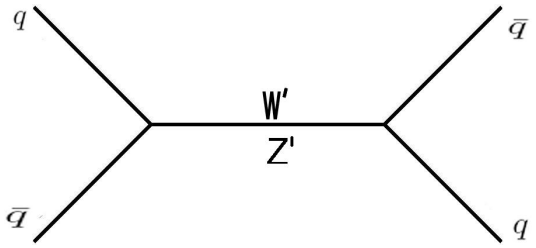

Figure 2.5: The Feynman diagram for a W' and Z'.

where M is the mass of the W or Z and M' is the mass of the W' or Z' respectively. The angular decay distribution of these vector particles is handled in the same way as for the axigluon previously discussed. The half width of the W' is

$$\frac{\Gamma}{2} = \frac{\Gamma_W}{2}\frac{M'_W}{M_W} \tag{2.22}$$

where $\Gamma_W \sim 2$ GeV [15]. The half width of the Z' is

$$\frac{\Gamma}{2} = \frac{\Gamma_Z}{2}\frac{M'_Z}{M_Z} \tag{2.23}$$

where $\Gamma_Z \sim 2.5$ GeV [15]. Both are significantly less than our dijet mass resolution.

2.7 Randall-Sundrum Gravitons

The Randall-Sundrum model addresses the question of why gravity is so weak compared to other fundamental forces. It proposes new extra dimensions and "branes", as in string theory. A brane is a lower dimensional subspace of a higher dimensional space. There are two branes. The theory claims that gravity stays localized near one brane rather than the other and it is stronger in the nearer brane and weaker in the other. The Randall-Sundrum model predicts massive spin-2 graviton. Fig. 2.6 shows the Feynman diagram for Randall-Sundrum graviton.

There are effectively only two parameters in the model. The parameter choices of most phenomenological interest are the mass, M, of the lightest graviton resonance, G, a coupling strength parameter $k/\bar{M}_{PL}$ where $\bar{M}_{PL}$ is Planck mass and k is a Planck

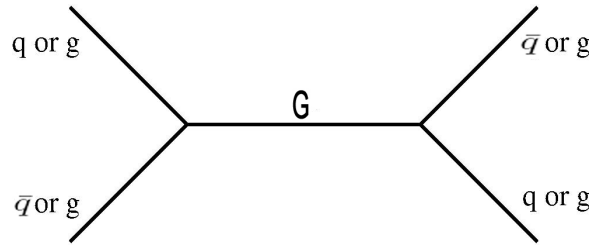

Figure 2.6: The Feynman diagram is shown for a Randall-Sundrum graviton.

scale constant. Our cross sections are calculated for $k/\bar{M}_{PL} = 0.1$ The lowest order differential cross section for the production of a spin-2 graviton resonance of mass M and width Γ per unit of center-of-mass scattering angle $\cos\theta$ and boost η is given by

$$\frac{d\sigma}{d\cos\theta d\eta_B} = \frac{1}{C_i}\left(\frac{2M}{s}\frac{\pi}{2}\Gamma\right)\left(\frac{20\pi}{M^2}B_i B_f \frac{1}{C_i}\right) F(\cos\theta^*) f(x_p^1) f(x_p^2) \tag{2.24}$$

where the boost $\eta_B = (\eta_1 + \eta_2)/2$ is the average pseudorapidity of the final state partons (jets), s is the square of the proton-proton collision energy, C_i is the color of the initial state (3 for $q\bar{q}$ and 8 for gg), B_i and B_f are the branching fractions for the initial state and the final state respectively, $f(x_p^1)$ and $f(x_p^2)$ are the parton distributions of the initial state, and $F(\cos\theta)$ are the normalized angular distributions of the sub-process

$$F(gg \to G \to q\bar{q}) = F(q\bar{q} \to G \to gg) = \frac{5}{8}(1 - \cos^4\theta), \tag{2.25}$$

$$F(gg \to G \to gg) = \frac{5}{32}(1 + 6\cos^2\theta + \cos^4\theta), \tag{2.26}$$

$$F(q\bar{q} \to G \to q\bar{q}) = \frac{5}{8}(1 - 3\cos^2\theta + 4\cos^4\theta). \tag{2.27}$$

The final state branching fractions are given by the ratio of the partial widths to the full widths, where the partial width [16] for photons is

$$\Gamma(G \to \gamma\gamma) = \frac{2x_1^2}{160\pi}\left(\frac{k}{\bar{M}_{Pl}}\right)^2 M, \tag{2.28}$$

for gluons is

$$\Gamma(G \to gg) = \frac{2x_1^2}{20\pi}\left(\frac{k}{\bar{M}_{Pl}}\right)^2 M, \tag{2.29}$$

for each variety of lepton is

$$\Gamma(G \to l\bar{l}) = \frac{2x_1^2}{320\pi}\left(\frac{k}{\bar{M}_{Pl}}\right)^2 M, \tag{2.30}$$

for each variety of light quark (u, d, s, c or b) is

$$\Gamma(G \to q\bar{q}) = \frac{6x_1^2}{320\pi}\left(\frac{k}{\bar{M}_{Pl}}\right)^2 M, \tag{2.31}$$

for the top quark is

$$\Gamma(G \to t\bar{t}) = \frac{6x_1^2}{320\pi}\left(\frac{k}{\bar{M}_{Pl}}\right)^2 M \left(1 - \frac{4m_t^2}{M^2}\right)^{3/2}\left(1 + \frac{8m_t^2}{3M^2}\right), \tag{2.32}$$

for the W boson is

$$\Gamma(G \to W^+W^-) = \frac{2x_1^2}{80\pi}\left(\frac{k}{\bar{M}_{Pl}}\right)^2 M \left(1 - \frac{4m_W^2}{M^2}\right)^{3/2}\left(\frac{13}{12} + \frac{14m_W^2}{3M^2} + \frac{4m_W^4}{M^2}\right), \tag{2.33}$$

and for the Z boson is

$$\Gamma(G \to ZZ) = \frac{x_1^2}{80\pi}\left(\frac{k}{\bar{M}_{Pl}}\right)^2 M \left(1 - \frac{4m_Z^2}{M^2}\right)^{3/2}\left(\frac{13}{12} + \frac{14m_Z^2}{3M^2} + \frac{4m_Z^4}{M^2}\right), \tag{2.34}$$

where $x_1 = 3.8317$ is the first zero of the Bessel function $J_1(x)$ of order 1. The full width Γ is the sum of the partial widths. For $\frac{k}{\bar{M}_{Pl}} = 0.1$, the percent width Γ/M is about 1%. The final state branching fractions B_f are just the partial widths divided by the full width. The initial state branching fractions for quarks are identical to the final state branching fractions for quarks. The initial state branching fractions for gluons are twice the final state branching fractions for gluons, removing a factor of 1/2 for identical particles in the final state. Other differences between initial state and final state spin and color statistics have already been accounted for in Eq. 2.24.

The differential cross section in Eq. 2.24 gives the same expression for graviton decays as can be found in the literature [16].

The total cross section at lowest order is given by the integration

$$\sigma = \int\int \frac{d\sigma}{d\cos\theta d\eta_B} d\cos\theta d\eta_B \tag{2.35}$$

over the angular range and the pseudorapidity boost range defined by our jet rapidity cuts, $|\eta_1| < \eta_{cut}$ and $|\eta_2| < \eta_{cut}$, and the fractional momentum of the partons, $\max(-\eta_{cut}, \ln\sqrt{\tau}) < \eta < \min(\eta_{cut}, -\ln\sqrt{\tau})$, where $\tau = M^2/s = x_p x_{\bar{p}}$, and $\eta_{cut} = 1$ in our search.

Mass (GeV)	q^* (pb)	A or C (pb)	E_6 Diquark (pb)	Z' (pb)	W' (pb)	G (pb)
500	0.2760E+04	0.1018E+04	0.1935E+03	0.2634E+02	0.4092E+02	0.1581E+03
600	0.1416E+04	0.5467E+03	0.1208E+03	0.1464E+02	0.2349E+02	0.7131E+02
700	0.7954E+03	0.3225E+03	0.8113E+02	0.8858E+01	0.1461E+02	0.3573E+02
800	0.4776E+03	0.2032E+03	0.5737E+02	0.5697E+01	0.9610E+01	0.1935E+02
900	0.3016E+03	0.1345E+03	0.4215E+02	0.3833E+01	0.6593E+01	0.1113E+02
1000	0.1981E+03	0.9240E+02	0.3189E+02	0.2669E+01	0.4671E+01	0.6719E+01
1200	0.9347E+02	0.4732E+02	0.1947E+02	0.1398E+01	0.2517E+01	0.2738E+01
1400	0.4812E+02	0.2618E+02	0.1262E+02	0.7874E+00	0.1450E+01	0.1250E+01
1600	0.2637E+02	0.1528E+02	0.8517E+01	0.4666E+00	0.8755E+00	0.6202E+00
1800	0.1514E+02	0.9274E+01	0.5917E+01	0.2868E+00	0.5464E+00	0.3283E+00
2000	0.9011E+01	0.5792E+01	0.4197E+01	0.1813E+00	0.3494E+00	0.1828E+00
2200	0.5514E+01	0.3698E+01	0.3023E+01	0.1170E+00	0.2275E+00	0.1059E+00
2400	0.3449E+01	0.2402E+01	0.2202E+01	0.7676E-01	0.1501E+00	0.6336E-01
2600	0.2197E+01	0.1581E+01	0.1618E+01	0.5102E-01	0.1001E+00	0.3889E-01
2800	0.1420E+01	0.1052E+01	0.1196E+01	0.3425E-01	0.6719E-01	0.2438E-01
3000	0.9281E+00	0.7055E+00	0.8876E+00	0.2318E-01	0.4533E-01	0.1554E-01
3200	0.6127E+00	0.4763E+00	0.6610E+00	0.1579E-01	0.3068E-01	0.1005E-01
3400	0.4077E+00	0.3233E+00	0.4931E+00	0.1081E-01	0.2081E-01	0.6565E-02
3600	0.2731E+00	0.2202E+00	0.3683E+00	0.7424E-02	0.1411E-01	0.4328E-02
3800	0.1838E+00	0.1504E+00	0.2751E+00	0.5113E-02	0.9567E-02	0.2873E-02
4000	0.1243E+00	0.1030E+00	0.2054E+00	0.3527E-02	0.6475E-02	0.1917E-02
4200	0.8429E-01	0.7054E-01	0.1532E+00	0.2435E-02	0.4371E-02	0.1284E-02
4400	0.5732E-01	0.4834E-01	0.1141E+00	0.1682E-02	0.2941E-02	0.8631E-03
4600	0.3905E-01	0.3312E-01	0.8481E-01	0.1160E-02	0.1970E-02	0.5810E-03
4800	0.2664E-01	0.2266E-01	0.6288E-01	0.7998E-03	0.1314E-02	0.3914E-03
5000	0.1819E-01	0.1548E-01	0.4648E-01	0.5501E-03	0.8717E-03	0.2637E-03
5500	0.7004E-02	0.5901E-02	0.2150E-01	0.2132E-03	0.3039E-03	0.9767E-04
6000	0.2684E-02	0.2194E-02	0.9677E-02	0.8044E-04	0.1012E-03	0.3555E-04
6500	0.1017E-02	0.7874E-03	0.4209E-02	0.2923E-04	0.3192E-04	0.1255E-04
7000	0.3792E-03	0.2695E-03	0.1756E-02	0.1011E-04	0.9494E-05	0.4245E-05
7500	0.1386E-03	0.8693E-04	0.6969E-03	0.3291E-05	0.2661E-05	0.1358E-05
8000	0.4954E-04	0.2610E-04	0.2604E-03	0.9947E-06	0.7087E-06	0.4051E-06

Table 2.4: The cross sections for dijet resonances (excited quark (q^*), axigluon (A) and coloron (C),...) are shown for jet pseudorapidity $|\eta| < 1$.

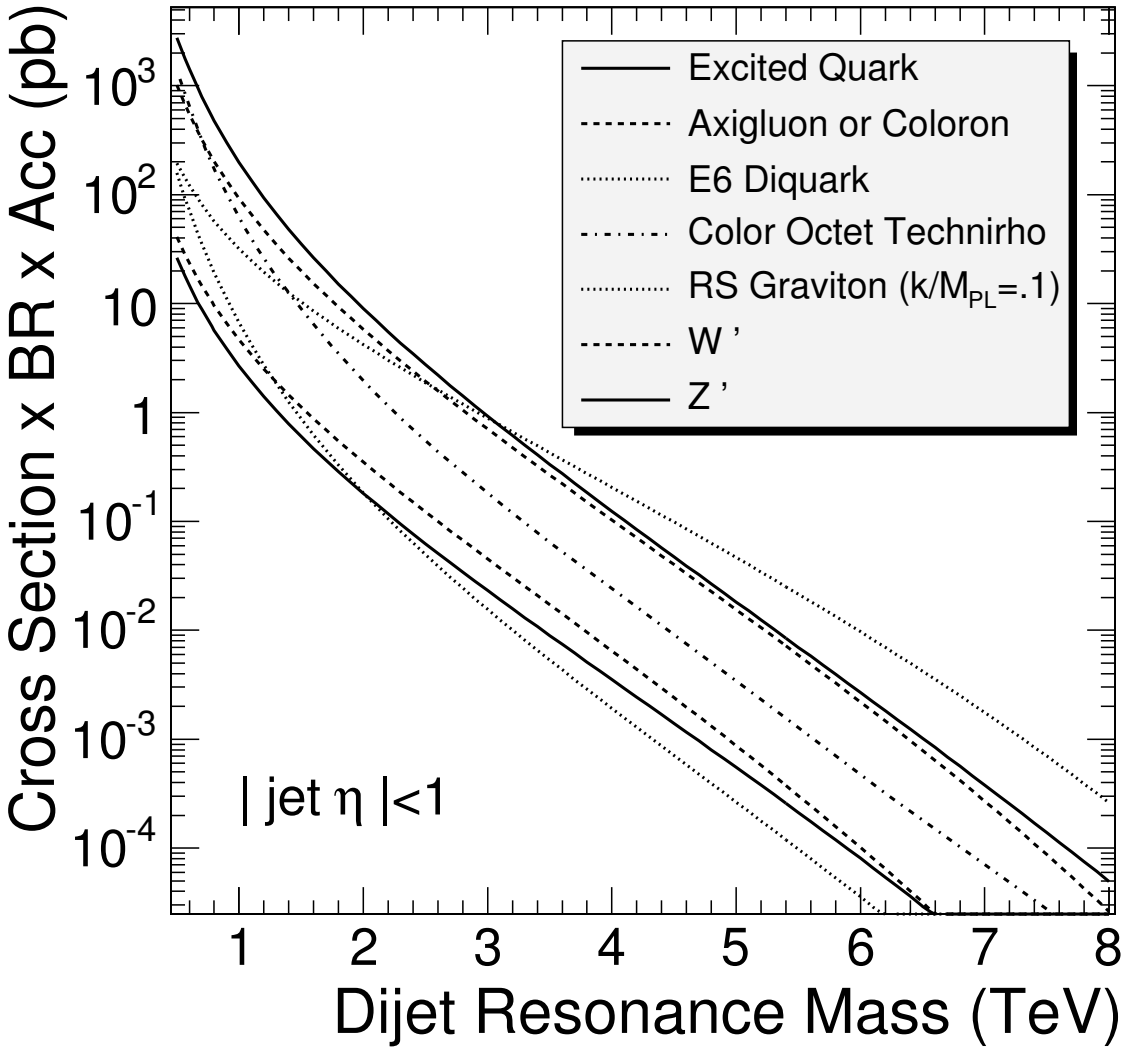

Figure 2.7: The cross section for dijet resonances with $|\eta| < 1$ is shown as a function of resonance mass for the following models: excited quarks (upper solid), axigluons or colorons (upper dashed), E_6 diquarks (upper dotted), color octet technirhos (dot-dashed), Randall-Sundrum gravitons (lower dotted), W' (lower dashed) and Z' (lower solid).

CHAPTER 3
THE CMS EXPERIMENT AT THE LHC

3.1 The Large Hadron Collider

The Large Hadron Collider (LHC) is a circular proton-proton collider, that is housed in a tunnel on the Swiss-French border. The LHC tunnel is buried about 50 to 175 m underground. Its circumference is 27 km. It is expected to collide protons at 14 TeV in the summer of 2008 which will be the highest collision energy ever reached. The LHC is expected to help unfold the mysteries of the universe and answer the most significant questions of physics: What is matter? How do we explain electroweak symmetry breaking? What gives mass to particles?

There are four experiments at the LHC: the Compact Muon Solenoid (CMS), A Large Torodial LHC Apparatus (ATLAS), Large Hadron Collider b-quark experiment (LHC-b), and A Large Ion Collider Experiment (ALICE). The CMS and ATLAS are multipurpose experiments, probing new physics at the TeV scale. The LHC-b is a specialized experiment dedicated to the study of bottom quark physics. It will attempt to shed light on CP violation. The ALICE is dedicated to heavy ion collisions. It will primarily study quark-gluon plasma (QGP).

A schematic diagram of the LHC machine is given in Fig. 3.1.

Protons will be accelerated by a linear accelerator (LINAC) up to 50 MeV, up to 1.4 GeV by a booster, up to 25 GeV by the Proton Synchrotron (PS), and then up to 450 GeV by the Super Proton Synchrotron (SPS), and they will finally be injected into the LHC ring to accelerate up to 7 TeV.

Proton bunches will collide at 40 MHz frequency, or every 25 ns. These bunches will have transverse spread $\sigma_x = \sigma_y = 15\ \mu$m and longitudinal spread 7.5 cm at the collision. The rate of a physics process can be calculated by

$$R = \sigma L \tag{3.1}$$

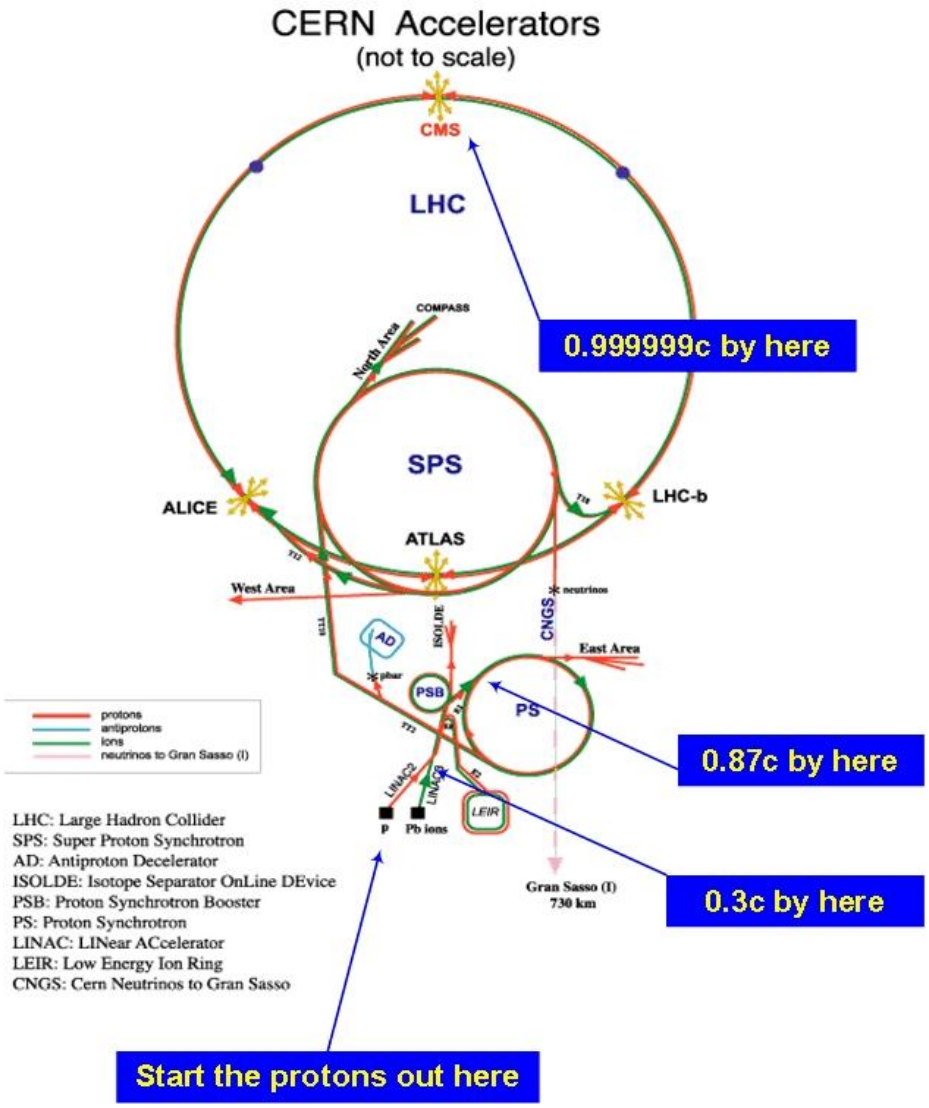

Figure 3.1: The LHC layout is shown.

where σ is the cross section and L is luminosity. The accelerator luminosity can be obtained by

$$L = \frac{f n_1 n_2}{4\pi\sigma_x\sigma_y} \tag{3.2}$$

where n_1 and n_2 are the number of particles in the bunches and f is collision frequency. The design luminosity of the LHC is $\mathcal{L} = 10^{34}\ \mathrm{cm}^{-2}\,\mathrm{s}^{-1}$. As seen from Eq. 3.1, the event rate of a certain process primarily depends on the cross section. Fig. 3.2 shows

the cross sections and rates of certain processes at proton-(anti)proton collisions for the Tevatron and LHC. The cross section for a 150 GeV/c^2 Higgs boson increases two orders of magnitude at the LHC compared to at the Tevatron, while the total cross section remains almost same (10^8 nb). High energy jets will also have at least a 100 times more cross section at the LHC than at the Tevatron. Since the occurrence of a physics process is directly proportional to the cross section, it is obvious that the LHC will produce many jets. This is why it is essential to understand jets if we want to discover new physics. More details about the LHC machine can be found at [17].

3.2 The Compact Muon Solenoid (CMS)

In this section, the different parts of the CMS detector are briefly explained. The CMS, a multipurpose detector, will explore new physics at TeV scale and discover the Higgs boson if it exists. Its main features are the following: First, it uses the most powerful solenoid magnet ($B = 4$T) ever constructed at its size. Second, the tracker and calorimeters are placed inside the coil, which makes the CMS a compact detector. Third, the CMS is optimized to detect muons efficiently because muons are signatures of interesting events; for example, Higgs decays to four muons: $H \rightarrow ZZ \rightarrow \mu\mu\mu\mu$.

An overall picture of the CMS can be seen in Fig. 3.3. The details of the CMS detector can be found at [19].

3.2.1 The Tracker

The CMS tracker is designed to reconstruct high p_{T} muons, electrons, and hadrons with high momentum resolution and efficiency and to measure the decay vertices of long-lived unstable particles. For this purpose, the all-silicon approach has been chosen for the tracking system. Finely segmented silicon sensors (pixels and strips) enable charged particles to be tracked and their momenta to be measured. Fig. 3.4 shows the tracking system.

The tracker covers the region $|\eta| < 2.5$. It reconstructs high p_{T} tracks with resolution $\delta P_T/P_T \approx (15P_T/\mathrm{TeV}/c + 0.5)\%$ in the central region $|\eta| < 1.6$, with

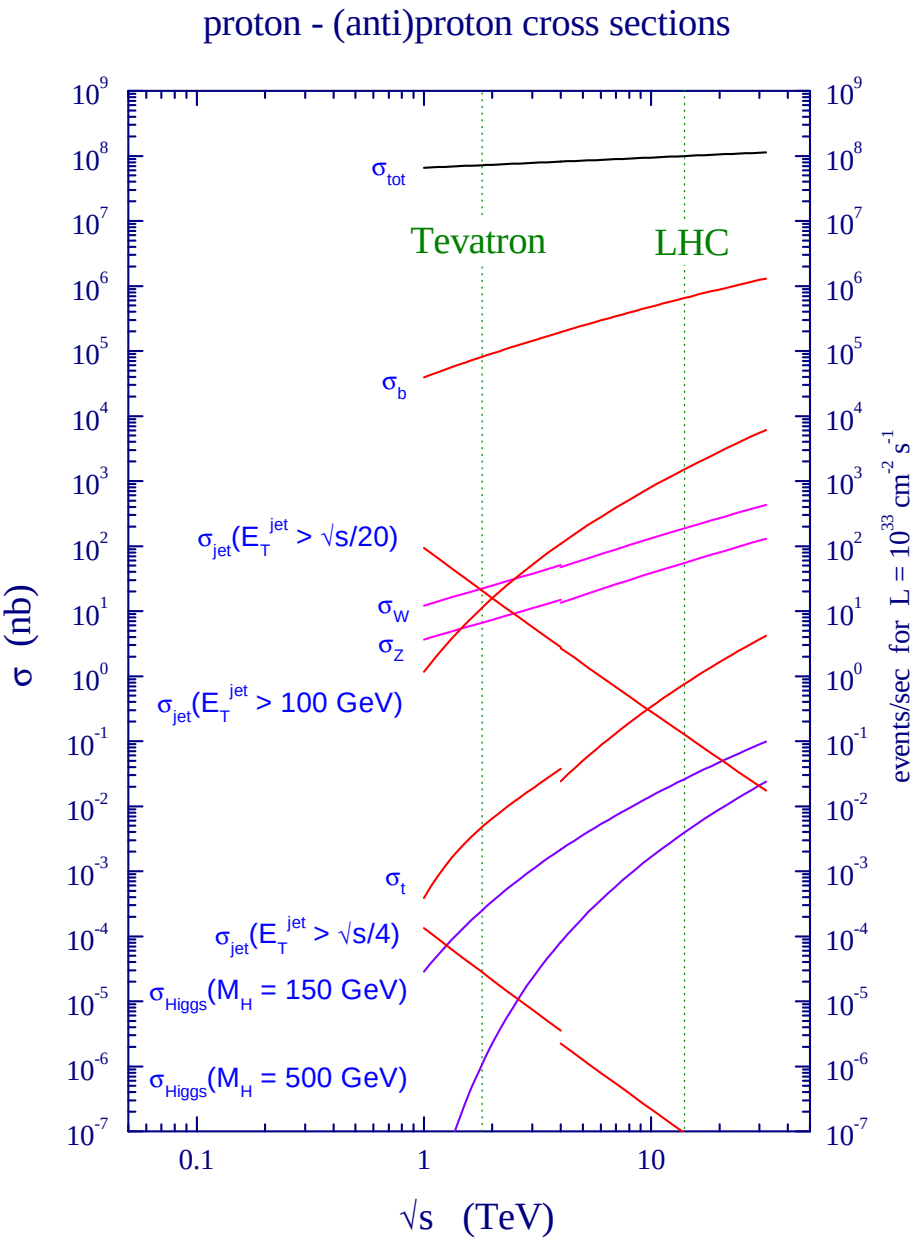

Figure 3.2: The Standard Model cross sections at the Tevatron ($\sqrt{s} \sim 2$ TeV) and LHC ($\sqrt{s} \sim 14$ TeV) colliders are given [18].

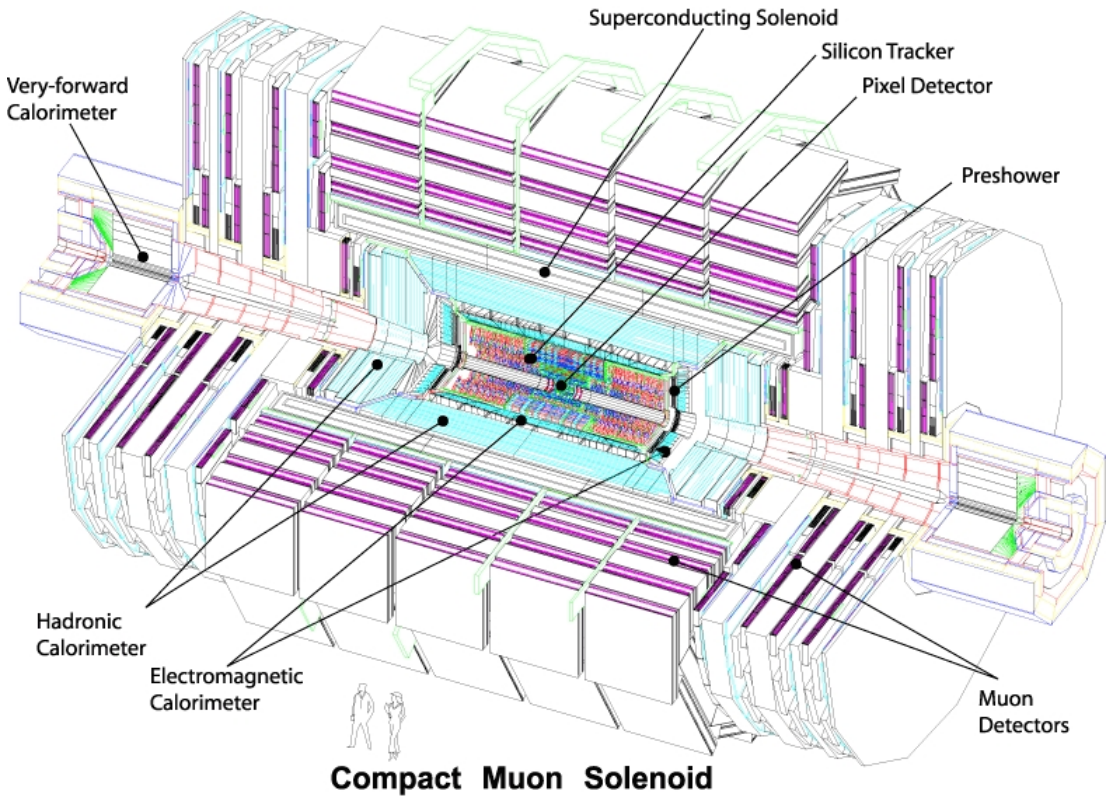

Figure 3.3: The CMS detector is depicted.

resolution $\delta P_T/P_T \approx (60 P_T/\mathrm{TeV}\,c + 0.5)\%$ as $|\eta|$ approaches 2.5.

Fig. 3.5 shows the CMS pixel detector. The pixel detector consists of 4.4 million pixels in a square measuring 150 μm per side. It provides spatial resolution of 15 μm. The silicon strip detector consists of 25,000 strips. There are three pixel layers and ten strip layers in the barrel part of the tracking system. In the endcaps, there are two pixel layers, three inner discs (TID) and nine outer forward silicon detectors. More information on the tracker can be found at [20].

3.2.2 The Electromagnetic Calorimeter (ECAL)

The electromagnetic calorimeter (ECAL) is designed to measure energies and positions of photons and electrons with high precision. It will also be used to measure the energies of hadrons and jets because they usually start showering in the ECAL and deposit some amount of their energy in it.

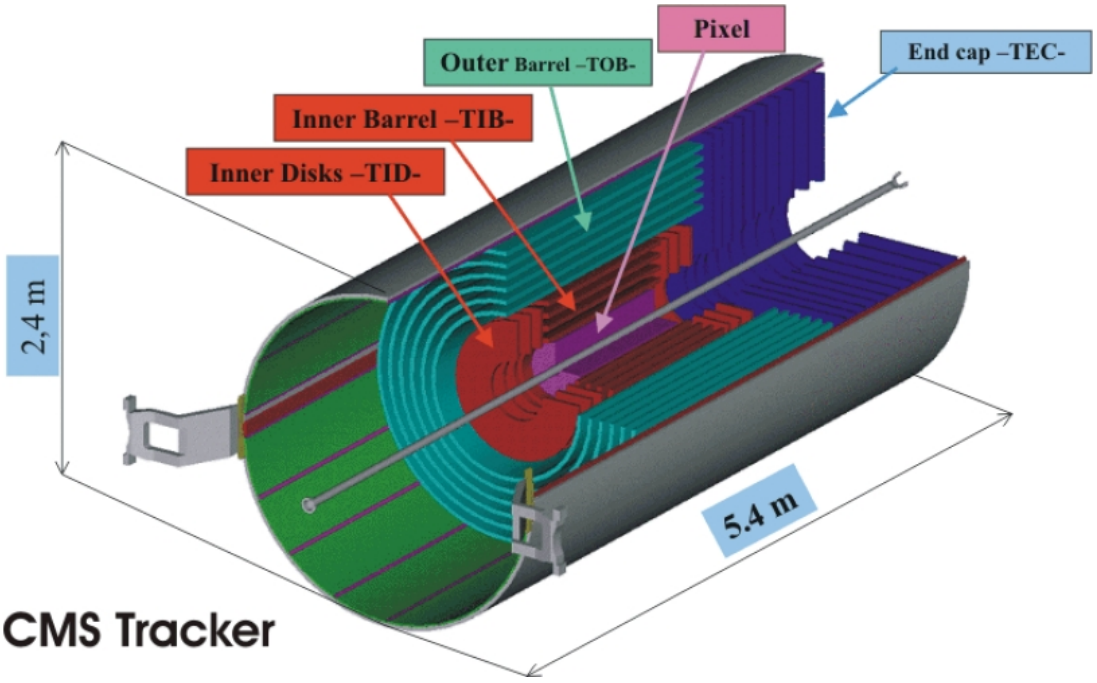

Figure 3.4: The CMS tracker is shown.

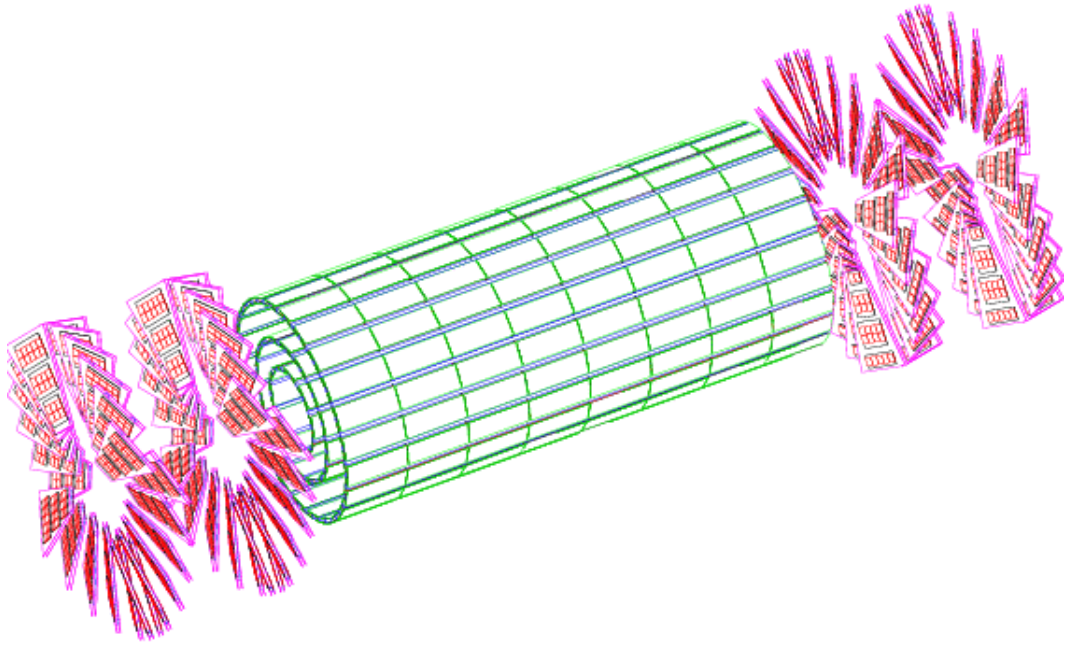

Figure 3.5: The CMS pixel detector is depicted.

The ECAL is a homogenous calorimeter. It is made of lead tungstate ($PbWO_4$) crystals. It has a high density (8.2 g/cm^3), short radiation length ($X_0 = 0.89$ cm),

and small Molière radius ($R_M = 2.19$ cm).

The ECAL consists of two parts: The barrel (EB) and endcap (EE). The EB covers the region $|\eta| < 1.48$. There are 36 supermodules in the EB, and each supermodule contains four modules. There are $61,000$ crystals in the EB. Each lead tungstate crystal has a front face area of 22×22 mm^2 and 26×26 mm^2 back face area. The length of each crystal is 23 cm, about $26X_0$). The crystals are tilted 3° with respect to the pointing axis. A picture of a crystal is shown in Fig. 3.6. Avalanche photo diodes (APD) are used to read out the signals at the back of the crystals in the EB.

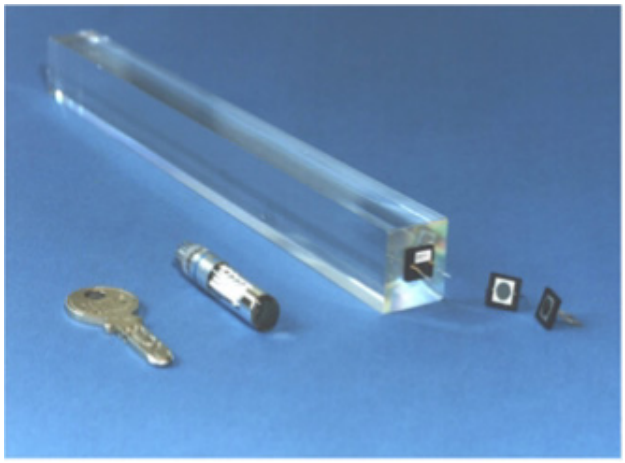

Figure 3.6: A sample of a lead tungstate crystal is shown.

The EE ranges between $1.5 < |\eta| < 3.0$. There are 7300 crystals in the EE. Vacuum photo triodes (VPT) will be used to read out the signals at the back of the crystals in the EE.

In front of the EE, there is a preshower detector (ES). It covers $1.6 < |\eta| < 2.6$. It is designed to reject π^0s which decay into two closely separated photons. The ES reduces one kind of background for the channel, which Higgs boson decays into two photons, by eliminating these π^0s [21].

3.2.3 The Hadronic Calorimeter

Together with the ECAL, the hadronic calorimeter (HCAL) is designed to identify hadrons and jets and to measure their energies. The HCAL consists of four

subdetectors: barrel (HB), endcap (HE), outer (HO) and forward (HF).

The HB and HE are located between the ECAL and the magnet. They are sampling calorimeters made of alternating layers of brass and plastic scintillator plates. The HB covers $|\eta| < 1.4$, and the HE extends to $1.5 < |\eta| < 3.0$. Each HB tower has a projective area of $\Delta\eta \times \Delta\phi = 0.087 \times 0.087$. Wavelength-shifting (WLS) fibers are embedded in the scintillator plates. Light collected from the scintillators are read out by the Hybrid Photo Diodes (HPD) detectors. The HB has about a 5.8 interaction length (λ_I) at $\eta = 0$.

The HB is not deep enough to contain a hadronic shower fully. Thus, the HO comes in to play to catch the tails of a hadronic shower. The HO is a scintillator detector, located between the magnet and muon system. It covers the region $|\eta| < 1.26$.

The HF, the last subdetector of HCAL, is located at $3.0 < |\eta| < 5.0$, outside the magnetic coil. It is made by steel as the absorber and quartz fibers as the active medium. Quartz fibers are chosen because of their radiation hardness, since the forward calorimeters will experience unprecedented particle fluxes. Short (1.43 m) and long (1.65 m) fibers are utilized. The short fibers start at a depth of 22 cm from the front of the detector. This arrangement makes it possible to distinguish showers generated by electrons and photons, which deposit a large fraction of their energy in the first 22 cm, from those generated by hadrons, which produce signals in both segments. HF calorimeters are designed to identify high energy jets with a good precision (20% to 30% at 1 TeV) [22].

The combined performance of the EB and HB based on 2006 test beam data is discussed in detail in Chapter 4. More information about the HCAL can be found at [23].

3.2.4 The Magnet

The superconducting solenoid will produce a four tesla uniform magnetic field. This field will be achieved by a 20 kA current. The solenoid is 13 m long and has a

radius of 5.9 m. Magnetic flux faces a 1.5 m thick iron yoke instrumented with four layers of muon chambers. A high magnetic field will enable the precise reconstruction of transverse momenta of charged particles. The design goal of the magnet is to achieve reconstruction of 1 TeV muons with a 15% p_{T} resolution. The relationship between the transverse momentum of a charged particle and the magnetic field is given by

$$P_T = 0.3BR \tag{3.3}$$

where B is the magnetic field in tesla and R is the radius of the curvature of the particle in m. Detailed information about the magnet can be found at [24].

3.2.5 The Muon System

Muons will be available in the final state of many events in the CMS. They transverse through the whole detector, leaving minimal ionizations behind. Thus, they are easy to identify in the detector. They also play an important role in interesting physics. Thus, identifying muons correctly and reconstructing their momenta precisely is one of the design goals of the CMS.

The CMS muon system consists of three detectors interleaved with iron return yoke plates that only muons and neutrinos can traverse: Drift Tubes (DT) in the barrel region, Cathode Strip Chambers (CSC) in the endcap region, and Resistive Plate Chambers (RPC) in both the barrel and endcap regions. A layout of the muon system is given in Fig. 3.7.

The DT and CSC will provide very accurate and precise position measurements while RPC provide precise time measurements. More information about the muon system can be found at [25].

3.2.6 The Trigger

The LHC will cross proton bunches 40 million times in a second at a design luminosity of $\mathcal{L} = 10^{34}\ \mathrm{cm}^{-2}\,\mathrm{s}^{-1}$. Approximately 20 interactions will take place at

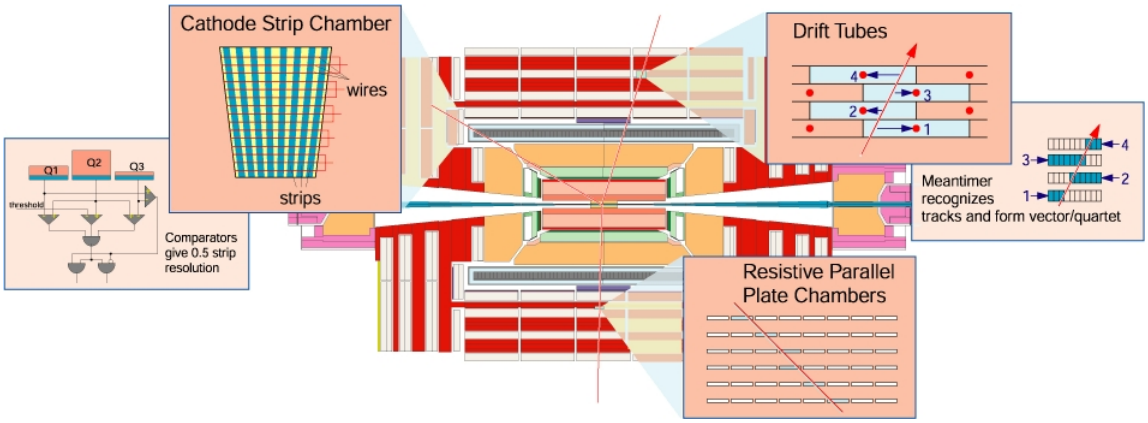

Figure 3.7: The CMS Muon system is depicted.

each crossing. Each event is estimated to have a 1 MB data size, from different parts of the detector. This is a huge amount of data, considering that the current data transfer rate is about 100 MB/s. Thus, selecting only interesting events and rejecting the others is important.

The CMS will utilize two trigger systems: The Level-1 (L1) and High Level Trigger (HLT). The L1 is a hardware trigger with fast event selection. It uses the calorimeters and muon system or both. It seeks signs of interesting events, for example, energy deposition above a threshold in a calorimeter cell. The L1 reduces the 40 MHz event rate to 100 KHz.

The HLT selects events by running software on a farm of computer processors. It uses information from all parts of the detector and completes the particle identification. The HLT takes a longer time ($\sim$ 1 ms) to decide to keep or reject an event and reduces event rate down to 100 Hz. Fig. 3.8 displays the trigger and data acquisition structure [26, 27, 28].

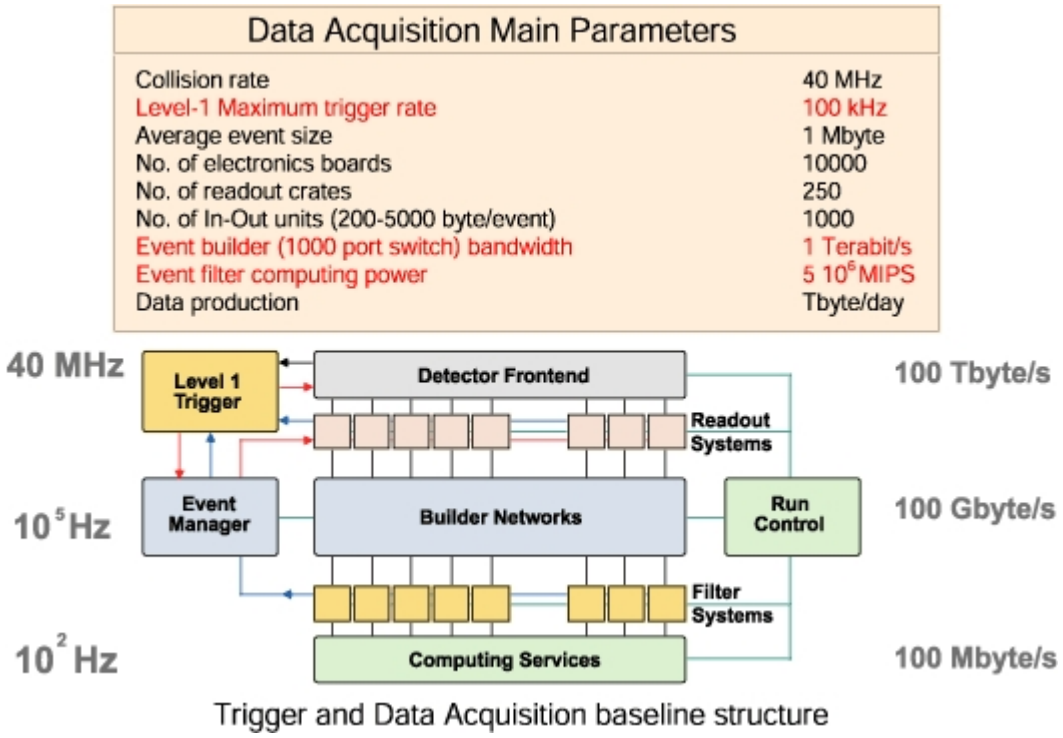

Figure 3.8: The CMS trigger and data acquisition structure are shown.

CHAPTER 4
THE CMS SENSITIVITY TO DIJET RESONANCES

4.1 Introduction

The theory of resonances (axigluon, coloron, excited quark, E_6 diquark, color octet technirho, W', Z', and Randall-Sundrum graviton) has already been discussed in Chapter 2. Dijet resonances are expected to be formed by the collisions of two partons (quarks and/or gluons) and to decay into two partons. In this chapter, I present the Monte Carlo study of our search for narrow resonances, X decaying to two jets: $pp \to X \to \text{jet} + \text{jet}$ (inclusive). Fig. 4.1 shows the Feynman diagram for a dijet resonance.

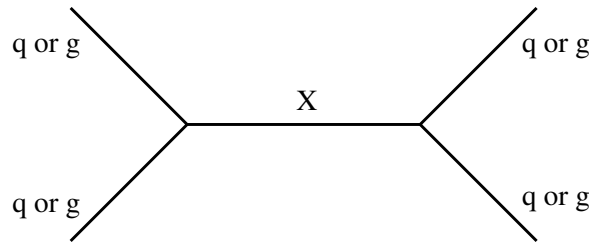

Figure 4.1: The Feynman diagram for a dijet resonance. The initial state and final state both contain two partons (quarks, antiquarks, or gluons), and the intermediate state contains an s-channel resonance X.

If new parton-parton resonances exist, the LHC will produce them copiously, and the resonances will appear as two jets (dijets) in the CMS detector. Hence, studying dijets is important and might be a gateway to new physics beyond SM.

4.2 General Strategy

All the resonances that I search for have narrow widths. Their widths are given in Table 2.1, and they are smaller than the dijet mass resolution that will be discussed in Section 4.4.1. Thus, they will all be observed with the same line shape in the dijet mass spectrum if they exist. I model the line shape for one of them (Z') and use it to

search for each resonance. In other words, this is a generic search for dijet resonances.

QCD dijet events are the biggest background in this search. If a resonance exists, it should appear as a bump on the QCD background. I simulate both signal (Z') and background (QCD) data. First, I use the QCD background as the data for a resonance search. The background's lack of signal enables me to determine the 95% confidence level (CL) upper limit on the cross section. This is later compared to the dijet cross section for any model of narrow resonance to determine the exclusion mass limits. Fig. 2.7 shows the relative cross sections of the narrow dijet resonances. Second, I add a 5σ signal to the QCD background and use both as the data. In this case, I measure the discovery cross section. Later, this is again compared to the theoretical cross sections of the dijet resonance models to determine the discovery mass region.

At the end of the analysis, I present the estimates for the narrow dijet resonance cross sections that can be excluded at 95% CL or discovered with 5σ significance. These cross section sensitivities are generic and can be applied to constrain the cross section of any model of narrow dijet resonances.

It is important to highlight a few points in Fig. 2.7. Resonances produced with strong interaction have higher cross sections than the others. Excited states of composite quarks [10] are strongly produced, so they have largest cross sections ($qg \to q^*$). Similarly, axigluons [7] or colorons [8] from an additional color interaction are also strongly produced. However, they require an antiquark in the initial state ($q\bar{q} \to A$ or C). They have slightly lower cross sections compared to the excited quarks. Diquarks [9] from superstring inspired E_6 Grand Unified Models are produced with electromagnetic coupling from the valence quarks of the proton ($ud \to D$). The cross section for E_6 diquarks at high mass is the largest of all the models considered because at high parton momentum, the probability of finding a quark in the proton is significantly larger than the probability of finding a gluon or antiquark. Color octet technirhos [12] from technicolor are produced for either gluons or quark-antiquark pairs in the initial state through a vector-dominance model of mixing between the gluon and the technirho ($q\bar{q}, gg \to g \to \rho_{T8}$). Randall-Sundrum gravitons [16] from a

model of large extra dimensions are produced from gluons or quark-antiquark pairs in the initial state ($q\bar{q}, gg \rightarrow G$). Heavy W' bosons [14] inspired by left-right symmetric Grand Unified Models have electroweak couplings and require antiquarks for their production ($q_1\bar{q}_2 \rightarrow W'$), thus giving small cross sections. Heavy Z' bosons [14] inspired by grand-unified models are widely anticipated by theorists, but they are electroweakly produced and require an antiquark in the initial state ($q\bar{q} \rightarrow Z'$), so their production cross section is about the lowest of the models considered.

Published lower limits from CDF [2] and D0 [29] on the mass of these models in the dijet channel are listed in Table 4.1.

q^*	A or C	D	ρ_{T8}	W'	Z'	G
0.78	0.98	0.42	0.48	0.8	0.6	-

Table 4.1: Published lower limits in TeV on the mass of new particles in the dijet channel. These 95% confidence level exclusions for q^*, W', and Z' are from D0 [29], and the rest are from the CDF [2] experiment.

4.3 Jets at CMS

4.3.1 Jet Definition

In high energy collider experiments, jet is commonly ascribed to one of three levels: parton, particle, or calorimeter level jet.

Partons (quarks and gluons) that are produced after the collisions are called "parton level jets" before they fragment into other particles.

A parton materializes into many particles (mostly mesons and baryons) through hadronization and fragmentation. The number of particles increases in a cone shape along the direction of the original quark or gluon. We define these particles as a "particle level jet."

When we want to measure the energy of a jet, the calorimeter comes into play. The hadronized particles deposit their energy in an approximate circle on the calorimeter. We use this "energy cluster" to measure the energy of the jet and conventionally refer

to it as a "calorimeter level jet." Fig. 4.2 depicts parton, particle and calorimeter level jets.

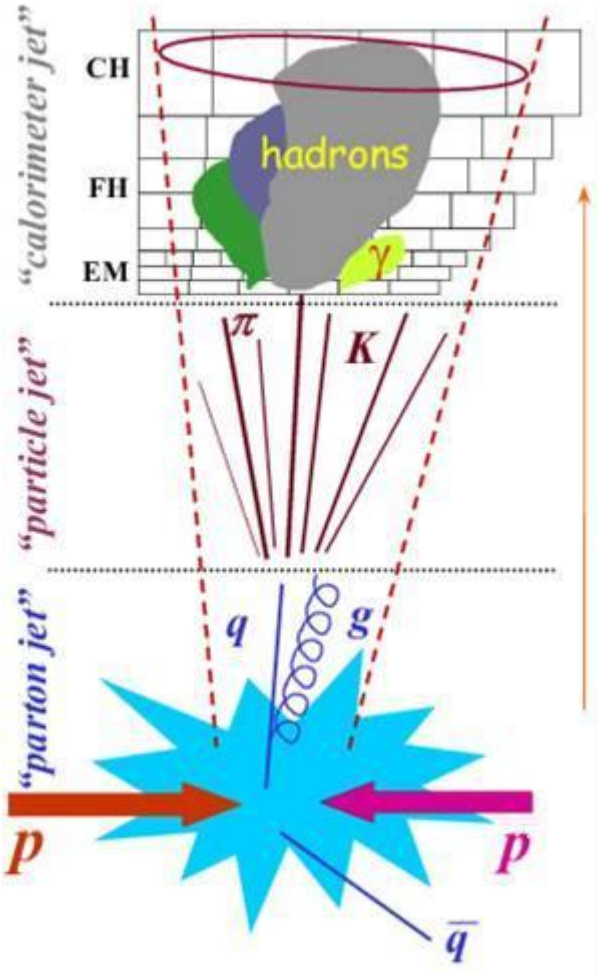

Figure 4.2: The jets at parton, particle, and calorimeter level are shown.

4.3.2 Jet Reconstruction

When a jet deposits its energy in a calorimeter, some portion of its energy is deposited into the electromagnetic calorimeter and some into the hadronic calorimeter. More specifically, the jet energy E is defined as the scalar sum of the calorimeter tower energies inside a cone of unitless radius $R = \sqrt{(\Delta\eta)^2 + (\Delta\phi)^2}$ (usually set to either 0.5 or 0.7) centered around the jet axis. The jet momentum $\vec{p}$ is the corre-

sponding vector sum of the calorimeter tower energies. The jet transverse energy is $E_T = E \sin\theta$, and the jet transverse momentum is $p_T = p \sin\theta$, where θ is the angle between the jet momentum and the proton beam.

We use the default CMS algorithm to reconstruct jets: The iterative cone algorithm with a cone size of $R = 0.5$. No seed threshold is used [30]. Each HCAL tower is required to have energy more than 0.5 GeV. Reconstructed jets are required to have p_T greater than 10 GeV/c.

4.3.3 Jet Correction

Both the reconstructed jet energy and momentum are corrected back to the energy and momentum of a particle level (generated) jet before pile-up. The correction is necessary because reconstructed jet energy depends on reconstructed jet p_{T} and η. When jet energy increases, less correction is needed. This is due to the nonlinear response of the calorimeter system to the hadrons. Reconstructed jet energy is also dependent on the jet rapidity because different parts of the detector have different response characteristics due to the materials and the noise factor. To obtain the jet energy correctly, we use a correction factor that is a function of both jet p_{T} and η in our analysis.

In the region $|\eta| < 1$, on average, a reconstructed p_{T} of 75 GeV/c is corrected by 33% to give 100 GeV/c, a p_{T} of 430 GeV/c by 16% to give 500 GeV/c, and a p_{T} of 2.8 TeV/c by 7% to give 3.0 TeV/c corrected jet p_{T}.

4.3.4 Jet Trigger

A proposal for a single jet trigger for the CMS is presented in Table 4.2 [31]. The trigger paths range from Level-1 (L1) to High Level Trigger (HLT). For low luminosity ($\mathcal{L} = 10^{32}$ cm^{-2} s^{-1}), three trigger paths are defined: low, medium, and high. When luminosity increases to $\mathcal{L} = 10^{33}$ cm^{-2} s^{-1}, a trigger path named ultra is added. When luminosity reaches $\mathcal{L} = 10^{34}$ cm^{-2} s^{-1}, another trigger path, super, is added. For each trigger path, E_T thresholds, prescales, estimates of resulting rates

at L1 and HLT and corresponding dijet mass ranges are presented. The dijet mass is calculated as $m = \sqrt{(E_1 + E_2)^2 - (\vec{p}_1 + \vec{p}_2)^2}$ where E_1 and E_2 are the energies of the two highest p_{T} jets and $\vec{p}_1$ and $\vec{p}_2$ are their momenta.

Path	L1				HLT		ANA
	E_T Cut (GeV)	Unpres. Rate (KHz)	Prescale (N)	Presc. Rate (KHz)	E_T Cut GeV)	Rate (Hz)	Dijet Mass (TeV)
Triggers for $\mathcal{L} = 10^{32}$ cm^{-2} s^{-1} and integrated luminosity = 100 pb^{-1}							
High	140	0.044	1	0.044	250	2.8	>0.67
Med	60	3.9	40	0.097	120	2.4	0.33-0.67
Low	25	2.9 $\times 10^2$	2,000	0.146	60	2.8	None
Triggers for $\mathcal{L} = 10^{33}$ cm^{-2} s^{-1} and integrated luminosity = 1 fb^{-1}							
Ultra	270	0.019	1	0.019	400	2.6	>1.13
High	140	0.44	10	0.044	250	2.8	0.67-1.13
Med	60	39	400	0.097	120	2.4	0.33-0.67
Low	25	2.9 $\times 10^3$	20,000	0.146	60	2.8	None
Triggers for $\mathcal{L} = 10^{34}$ cm^{-2} s^{-1} and integrated luminosity = 10 fb^{-1}							
Super	450	0.014	1	0.014	600	2.8	>1.80
Ultra	270	0.19	10	0.019	400	2.6	1.13-1.80
High	140	4.4	100	0.044	250	2.8	0.67-1.13
Med	60	3.9 $\times 10^2$	4,000	0.097	120	2.4	0.33-0.67
Low	25	2.9 $\times 10^4$	200,000	0.146	60	2.8	None

Table 4.2: The single jet trigger table previously proposed [31], showing path names, trigger thresholds in corrected E_T, prescales, and estimated rates at L1 and HLT for three different luminosity scenarios, and here I also list the corresponding range of corrected dijet mass used. The trigger in the Low path is not used to measure the dijet mass.

The lower value of the mass range is the lowest value of dijet mass for which the trigger is fully efficient [31]. The upper value of the mass range is the mass value at which the next highest threshold trigger becomes fully efficient.

4.4 Dijets at CMS

4.4.1 The Signal: Resonance Dijets

I simulated the inclusive process $pp \rightarrow Z' \rightarrow q\bar{q}$ at three different masses of Z', 0.7, 2.0, and 5.0 TeV/c^2. I used PYTHIA to generate the events, OSCAR 3_7_9 for the CMS detector simulation, and ORCA 8_7_1 for the digitization and reconstruction of events.

During the digitization, each Z' event was mixed with a number of minimum bias events corresponding to the anticipated number of multiple interactions for a luminosity of 2×10^{33} cm^{-2} s^{-1}. The same number of pile-up interactions were used when the jet corrections were formed. For these dijet mass values, the jet corrections removed practically all effects of pile-up, so these dijet mass distributions are applicable to all the luminosities considered.

The simulated shape of a 2 TeV narrow dijet resonance in the CMS is shown in Fig. 4.3. The shape is composed of a Gaussian region and a long tail to low dijet mass. The Gaussian component can be seen from a fit to the peak.

Fig. 4.3 also shows the dijet mass resolution with respect to resonance mass. The vertical axis is the standard deviation, σ, divided by the mean value of resonance histogram. It is well fit by the function $\sigma/M = 0.045 + 1.3/\sqrt{M}$ where M is given in GeV. I used this expression to define the bin widths of the dijet mass distributions for both signal and QCD events.

In the resonance shape, the long tail to low mass comes predominantly from final state QCD radiation. When a parton emits a hard gluon at an angle that is not inside the jet cone, it can produce particles far away from the jet. This causes a loss in the energy of the reconstructed jet and produces a low mass tail.

For high mass $Z' \sim 5$ TeV, in Fig. 4.5, the existence of parton distributions is another reason for the rise at low mass tail because the cross section to produce a resonance of mass M in a collision depends on the probability of finding a parton with a certain momentum fraction inside each proton and Breit-Wigner cross section. Since at low mass, the probability of finding a parton with a certain momentum

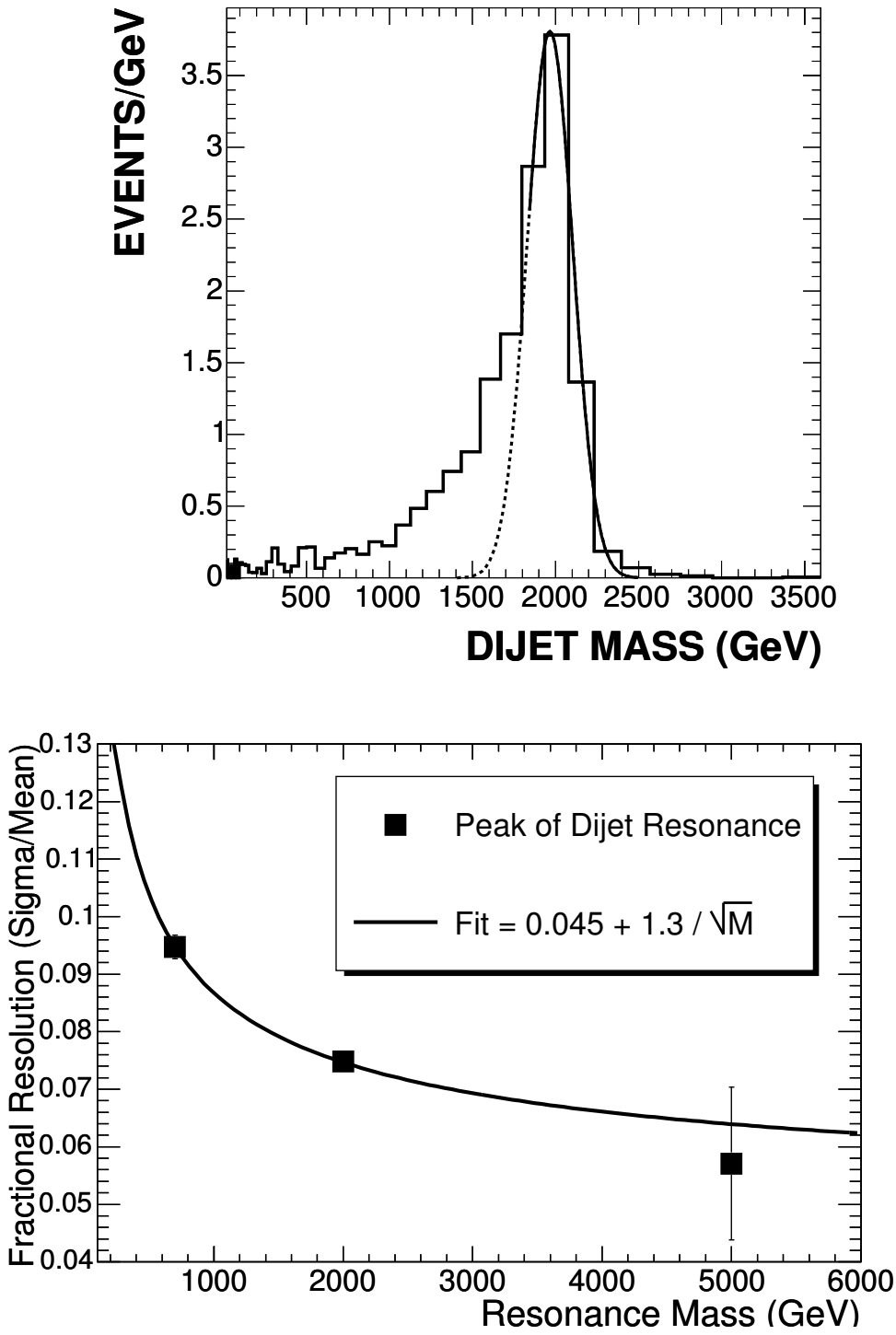

Figure 4.3: Top) The dijet mass distribution from a 2 TeV Z' (histogram) is fit with a Gaussian (solid curve) on its high mass edge and the Gaussian is extended to a lower mass (dashed curve). Bottom) The dijet mass resolution (squares) from Gaussian fits like one in the top plot are shown as a function of input Z' mass, M, and fit with a smooth parameterization (solid) of the form $p_0 + p_1/\sqrt{M}$.

fraction inside a proton is very high, the total cross section increases in this mass region. The low mass tail and associated systematic uncertainties will be discussed in greater detail in Section 4.7.

4.4.2 The Background: QCD Dijets

All physics processes that result in two jets in the final state are the background for dijet resonance searches. These can be QCD dijet events in which there are only partons in the initial, intermediate, and final state or they can be hadronic decays of W or Z bosons, *etc.* Among these events, QCD events take the biggest portion of the background and in this analysis, we consider QCD dijet events as the only background. The other processes, such as the hadronic decay of Z, have cross sections at least two orders of magnitude below the QCD cross sections for any given dijet mass.

I use a sample of QCD events produced at Fermilab, simulated with OSCAR 2_4_5, originally reconstructed with ORCA 7_6_1, and then re-reconstructed for jets with ORCA 8_7_3. A total of 210,000 events are used from 21 samples, each consisting of 10,000 events sub-samples in contiguous intervals in generator level of p_T spanning from 0 to 4000 GeV/c: 0-15, 15-20, 20-30, 30-50, 50-80, 80-120, 120-170, 170-230, 230-300, 300-380, 380-470, 470-600, 600-800, 800-1000, 1000-1400, 1400-1800, 1800-2200, 2200-2600, 2600-3000, 3000-3500, and 3500-4000.

The measured cross section as a function of dijet mass is shown in Fig. 4.4, taken from the reference [31]. The prescaled triggers allow us to measure mass down to 330 GeV/c^2. The mass measured with the prescaled triggers will allow us to connect to dijet masses measured at the Tevatron [13, 32]. Since there has been no new physics beyond the SM discovered in dijets at the Tevatron, this mass region can be a control region of the CMS measurement.

4.4.3 Event Selection

I select events in which each leading jet has $|\eta| < 1$. This cut is chosen because of the following fact: the resonances are s-channel objects that tend to decay isotrop-

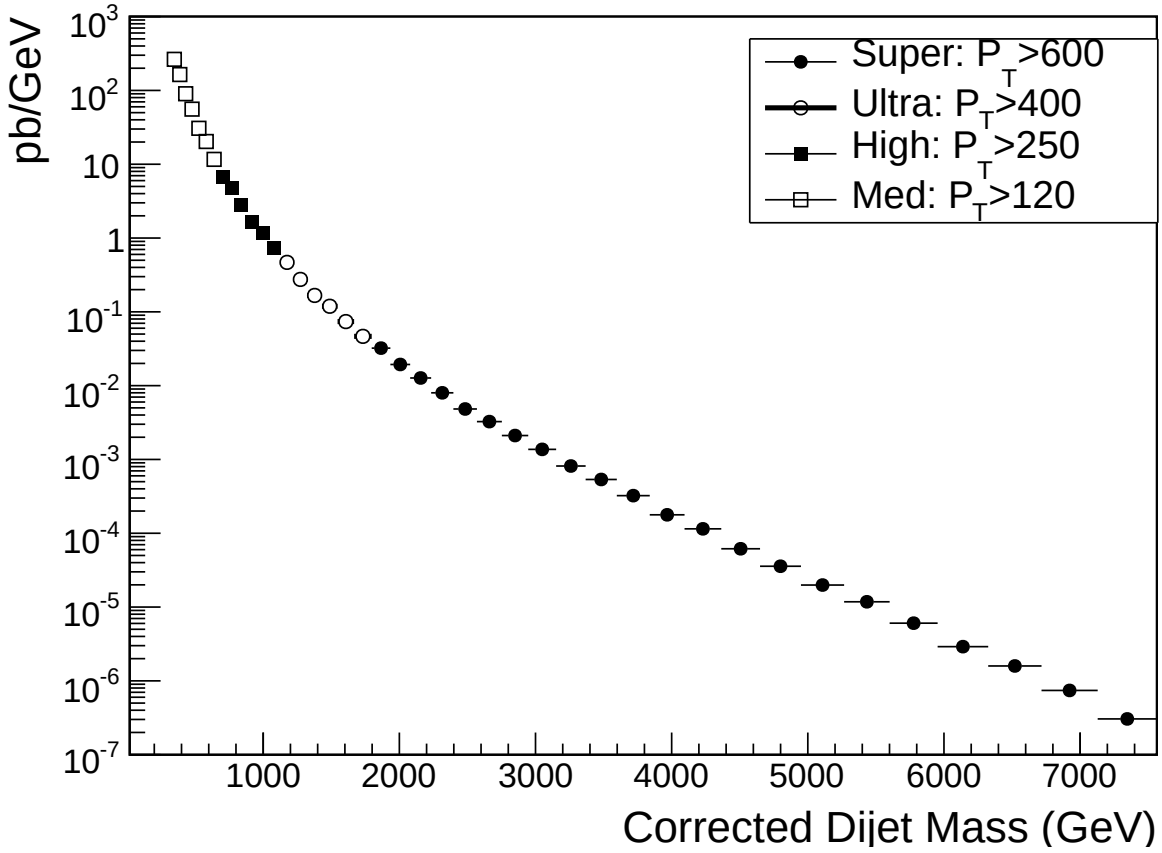

Figure 4.4: The QCD differential cross section vs. dijet mass, showing the contributing jet triggers with different symbols, listed with their path names and p_{T} thresholds at HLT in the legend.

ically in the detector. On the other hand, QCD events peak in the forward and backward directions. QCD is predominantly a t-channel exchange, like Rutherford scattering: it is the scattering of two objects that peak in the forward and backward directions. Hence, the $|\eta| < 1$ cut rejects much more background than the signal, usually gives a much better significance for our search. The value of the $|\eta|$ cut was also intended to be similar to the prior resonance searches at the Tevatron [2, 29]. Optimization of the $|\eta|$ cut for the LHC has not been done, but we expect from the Tevatron experience that the cut is reasonably close to the optimal value.

4.4.4 Signal and Background Comparison

Shown in the Fig. 4.5.a is the comparison of the simulated differential cross section of a Z' as a function of dijet mass with the QCD cross section. It is clear that this Z' model has a low rate compared to the QCD and will be difficult to discover. In the Fig. 4.5.b, the same signal shape but with the total cross section appropriate for an excited quark is shown; here the signal to background ratio is much better. In all plots that are a function of dijet mass, I plot in bins of width equal to the expected mass resolution discussed in Section 4.4.1.

Fig. 4.5.c shows the ratio of excited quark and E_6 diquark signals to the QCD background. The ratio indicates that the long tail to low mass is effectively lost in the large QCD background. We will only be sensitive to the Gaussian part of the distribution in the search. The signal to background ratio of any narrow resonance will have this shape in the CMS detector. I discuss how the tail to low mass affects our sensitivities in Section 4.7.

Fig. 4.5.c also shows that although the sensitivity to an excited quark is higher than the sensitivity to an E_6 diquark at low dijet mass, this situation is reversed at high dijet mass. The sensitivity to E_6 diquarks becomes higher than that of excited quarks. This can be explained by the fact that E_6 diquarks are produced from valence quarks in the proton while excited quarks require a gluon in their production; also at high momentum, the probability of finding a quark is larger than the probability of finding a gluon. This increases the sensitivity to E_6 diquarks at high dijet mass.

4.5 Search for Resonances

I use a Bayesian technique based on a binned likelihood [33] to search for resonances. I employ a binned likelihood which uses three distributions in dijet mass m: data, background, and signal. For each dijet mass bin, i,

1. Data: measured number of events, n_i, in data.

2. Background: expected number of events, $N_i(B)$, from background.

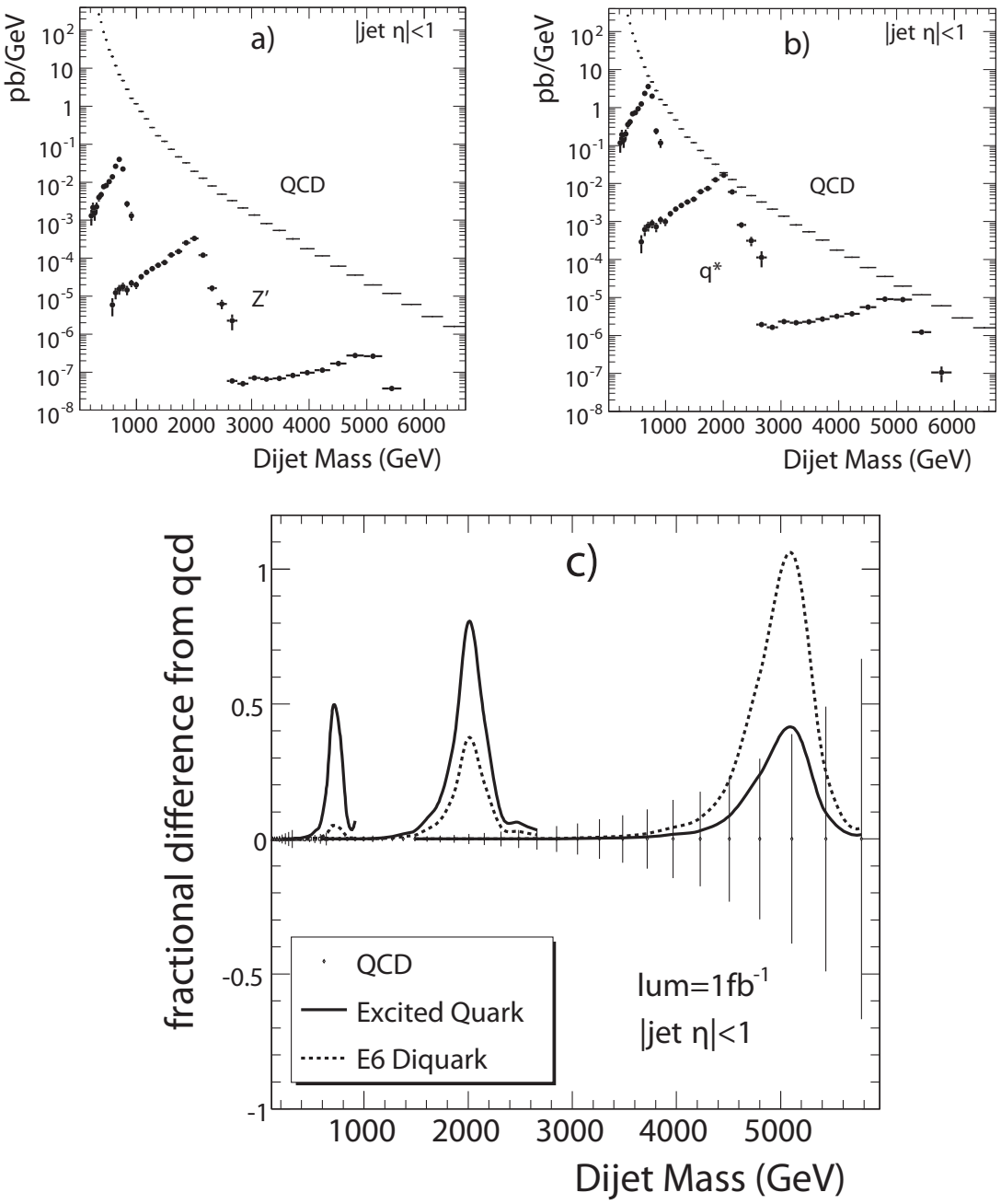

Figure 4.5: a) The differential cross section as a function of dijet mass for the QCD background and three Z' signals with a mass of 0.7, 2, and 5 TeV/c^2. b) An excited quark signal using the same resonance masses and shapes as the left plot but with the appropriate total cross section for an excited quark. c) Using the same resonance masses and shapes, I show the fractional difference between an excited quark (solid curve) or an E_6 diquark (dashed curve) and the QCD dijet background compared to the QCD statistical error (vertical lines) for 1fb^{-1}.

3. Signal: number of events, $N_i(S)$, from signal.

I form a signal likelihood as a function of signal cross section for any value of dijet resonance mass M. The normalization of the signal at this point is arbitrary. It could be a normalized distribution or a distribution in number of events. I multiply the size of the signal by the parameter α to get the mean number of expected events, μ_i, in bin i:

$$\mu_i = \alpha N_i(S) + N_i(B). \tag{4.1}$$

The probability P_i of observing n_i events when μ_i are predicted is given by Poisson statistics:

$$P_i = (\mu_i^{n_i} e^{-\mu_i})/(n_i!) \tag{4.2}$$

and the product of P_i over all bins in the mass spectrum is the likelihood function L for seeing the observation given the prediction:

$$L = \prod_i P_i. \tag{4.3}$$

This is the likelihood as a function of α for the existence of a dijet resonance of mass M with number of events $\alpha \sum_i N_i(S)$.

I use the likelihood distribution to find the signal cross section value that is excluded at 95% confidence and 5σ discovery cross section value. This process is repeated for each resonance mass value. The likelihood in the presence of systematics is determined by convoluting this likelihood with the systematic uncertainty as a function of signal cross section.

4.6 Sensitivity with Statistical Errors Only

Our search method needs two inputs - background and signal - that we use to search for a signal in data. We fit QCD data with a parameterization of the form

$$\frac{d\sigma}{dm} = \frac{p_0(1 - m/\sqrt{s})^{p_1}}{m^{p_2}} \tag{4.4}$$

where m is the dijet mass in GeV, $\sqrt{s} = 14000$ GeV, and the parameters found in the fit are $p_0 = 6 \times 10^{14}$ pb/GeV, $p_1 = 8.0$, and $p_2 = 4.8$. Fig. 4.6 shows the differential cross section and the fit. We prefer to use the fit function as a background instead of data sample. This way, we get rid of the statistical fluctuations particular to this data set. To find the number of events $N_i(B)$ in bin i, I multiply the value of the fit function, $d\sigma/dm$, at that bin by bin widths and integrated luminosity and then divide it by prescales.

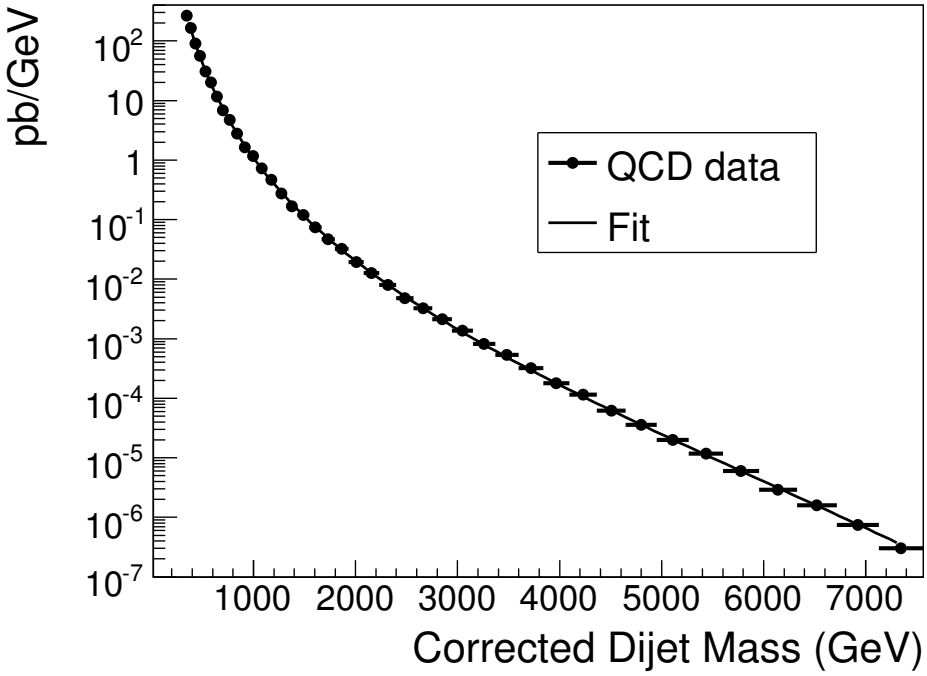

Figure 4.6: The full CMS simulation of the QCD differential cross section *vs.* dijet mass (points) is fit to a smooth parameterization (curve).

I use the simulated Z' sample for the signal and I perform the analysis with two classes of observed data:

1. Data with no signal, where I measure only QCD.

2. Data with a significant signal, where I measure QCD and a 5σ signal.

When the data is only QCD, I set the number of observed events, n_i, equal to the background, $N_i(B)$. In this case, the signal likelihood peaks at the zero cross section. Fig. 4.7 top plot shows the likelihood distribution for a narrow resonance of 2 TeV/c^2 narrow mass. The arrow indicates the cross section value above which no signal can be found with 95% CL.

When the data include a significant signal, I set the number of observed events, n_i, equal to background plus the signal $N_i(S)$ with an arbitrary signal rate. I then increase the size of the signal until our likelihood peaks 5σ away from zero, where σ is the Gaussian width of the final likelihood distribution. Fig. 4.7 bottom plot shows the discovery likelihood and 5σ discovery point for the 2 TeV/c^2 resonance. The peak point of the likelihoods is the signal cross section at which we can discover the resonance at 5σ significance.

Fig. 4.8 shows the comparison of resonance signals' size of 95% CL and the 5σ discovery cross section with the size of the statistical error bars of QCD. As can be seen, the 95% CL excluded mass bumps are just above the error bars. This is expected when the data agrees with the QCD. In only one out of 20 cases, we see such a signal in the data. In 19 out of 20 cases, we see no signal but QCD events. This is the meaning of the 95% CL exclusion cross section. On the other hand, 5σ discovery bumps are well above the statistical error bars. This is expected for a signal at this level of significance. A 5σ discovery signal should be very obvious in our data.

I simulated the signal data at three mass points : 0.7, 2, and 5 TeV/c^2 and interpolated the cross section *vs* dijet mass histograms for in between points, using the simulated ones. I followed a linear interpolation approach given in the reference [34] and the same procedure for interpolated points and, then produced the exclusion and discovery likelihood distributions for each value of the resonance mass from 0.7 TeV to 5.0 TeV in 0.1 TeV steps.

Fig. 4.9 compares the cross section sensitivities with statistical uncertainties only to the calculated resonance cross sections in seven different models. Mass sensitivities

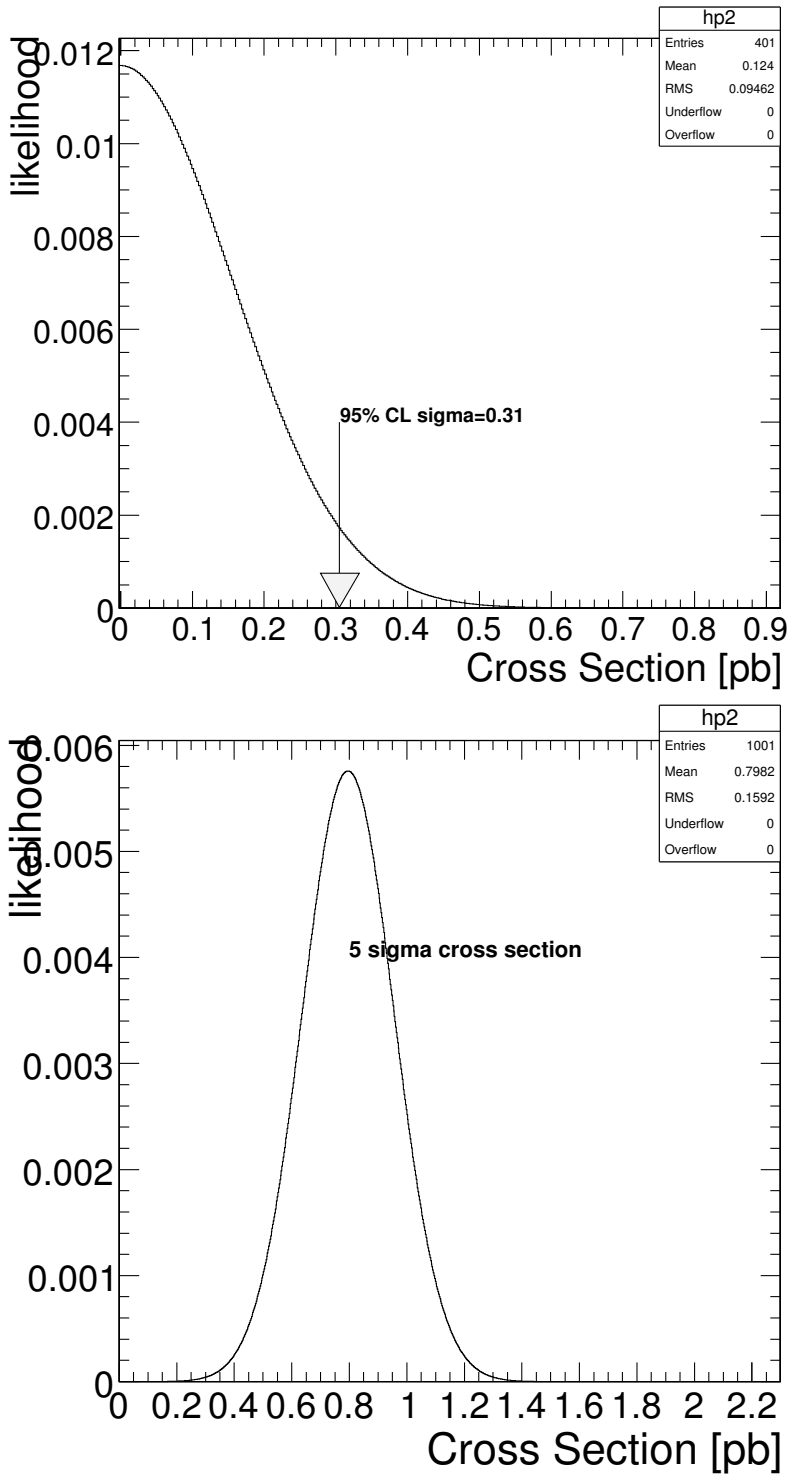

Figure 4.7: Likelihoods with statistical uncertainties only for observing a narrow dijet resonance of mass 2 TeV/c^2 in a 1 fb^{-1} data sample that contains only the QCD background (top) and a data sample that also contains a resonance with a significance of 5σ (bottom).

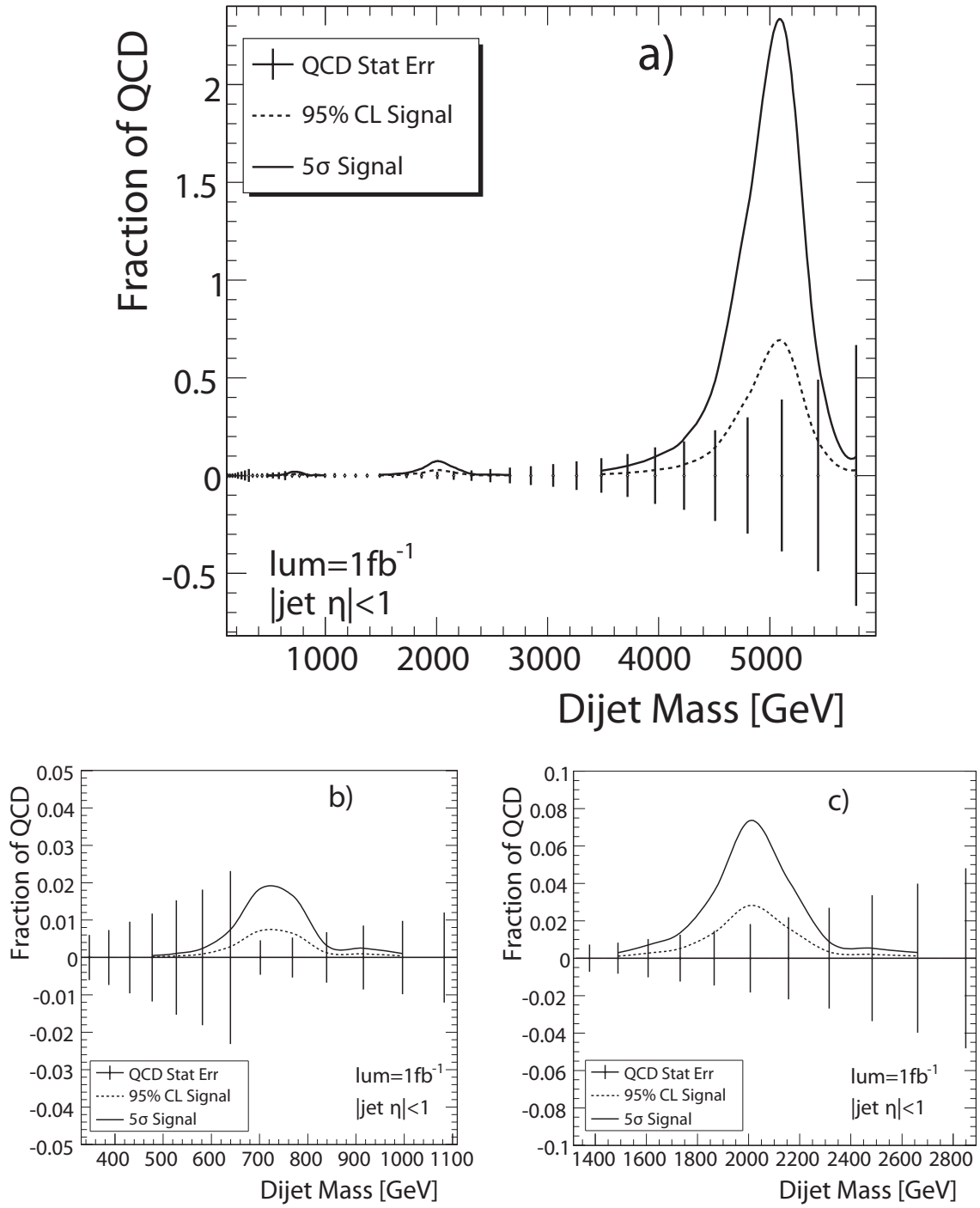

Figure 4.8: a) The cross section of resonance signals at 0.7, 2.0, and 5.0 TeV/c^2 that could be excluded at 95% CL (dashed) or discovered with 5σ significance (solid), including statistical uncertainties only, is shown as a fraction of the QCD background and compared to the statistical errors on the QCD background for a sample of size 1 fb^{-1}. b) The zoomed view for a 0.7 TeV/c^2 resonance. b) Zoomed view for a 2.0 TeV/c^2 resonance.

above 5 TeV were determined by linear extrapolation of the 95% CL and 5σ discovery cross sections in Fig. 4.9. I conclude that all the resonance models above the 95% CL exclusion line can be excluded with 95% CL and that all the models above the discovery line can be discovered at 5σ discovery. In this way, the mass regions for exclusion and discovery can be extracted. Table 4.3 shows the exclusion and discovery mass regions for each model.

Table 4.3 shows that the CMS can discover an excited quark with 5σ significance up to a mass as high as 5.0 TeV, for an integrated luminosity of 10 fb^{-1}. This agrees with the previous estimate of excited quark discovery mass reach at the LHC [35], which was 5.3 TeV for 10 fb^{-1} luminosity and the same level of significance. Multiple entries in Table 4.3 indicate multiple mass regions to exclude the resonance for the same integrated luminosity.

Resonance Model	95% CL Excluded Mass (TeV/c^2)			5σ Discovered Mass (TeV/c^2)		
	100 pb^{-1}	1 fb^{-1}	10 fb^{-1}	100 pb^{-1}	1 fb^{-1}	10 fb^{-1}
Excited Quark	0.7 - 3.8	0.7 - 4.8	0.7 - 5.8	0.7 - 2.9	0.7 - 3.9	0.7 - 5.0
Axigluon or Coloron	0.7 - 3.6	0.7 - 4.6	0.7 - 5.6	0.7 - 2.6	0.7 - 3.8	0.7 - 4.8
E_6 diquark	0.7 - 4.1	0.7 - 5.6	0.7 - 7.0	0.7 - 2.8	0.7 - 4.5	0.7 - 6.0
Color Octet Technirho	0.7 - 2.4	0.7 - 3.4	0.7 - 4.5	0.7 - 1.8	0.7 - 2.6	0.7 - 3.6
Randall-Sundrum Graviton	0.7 - 1.1	0.7 - 1.7	0.7 - 1.7 1.9 - 2.4	0.7 - 0.8	0.7 - 0.8	0.7 - 0.8
W'	0.7 - 1.0	0.7 - 1.0 1.2 - 2.1	0.7 - 1.0 1.2 - 3.4	N/A	N/A	2.0 - 2.3
Z'	N/A	1.2 - 1.5	1.3 - 1.5 1.9 - 2.6	N/A	N/A	N/A

Table 4.3: Sensitivity to dijet resonances with 100 pb^{-1}, 1 fb^{-1}, and 10 fb^{-1}. For each resonance model, I show the range of masses we expect to be able to exclude at a confidence level of 95% or greater and the range of masses we expect to be able to discover with a significance of 5σ or greater. Multiple entries indicate multiple mass regions to exclude the resonance for the same integrated luminosity. All estimates are with statistical uncertainties only.

4.7 Systematic Uncertainties

The sources of the systematic uncertainties for this analysis are the following:

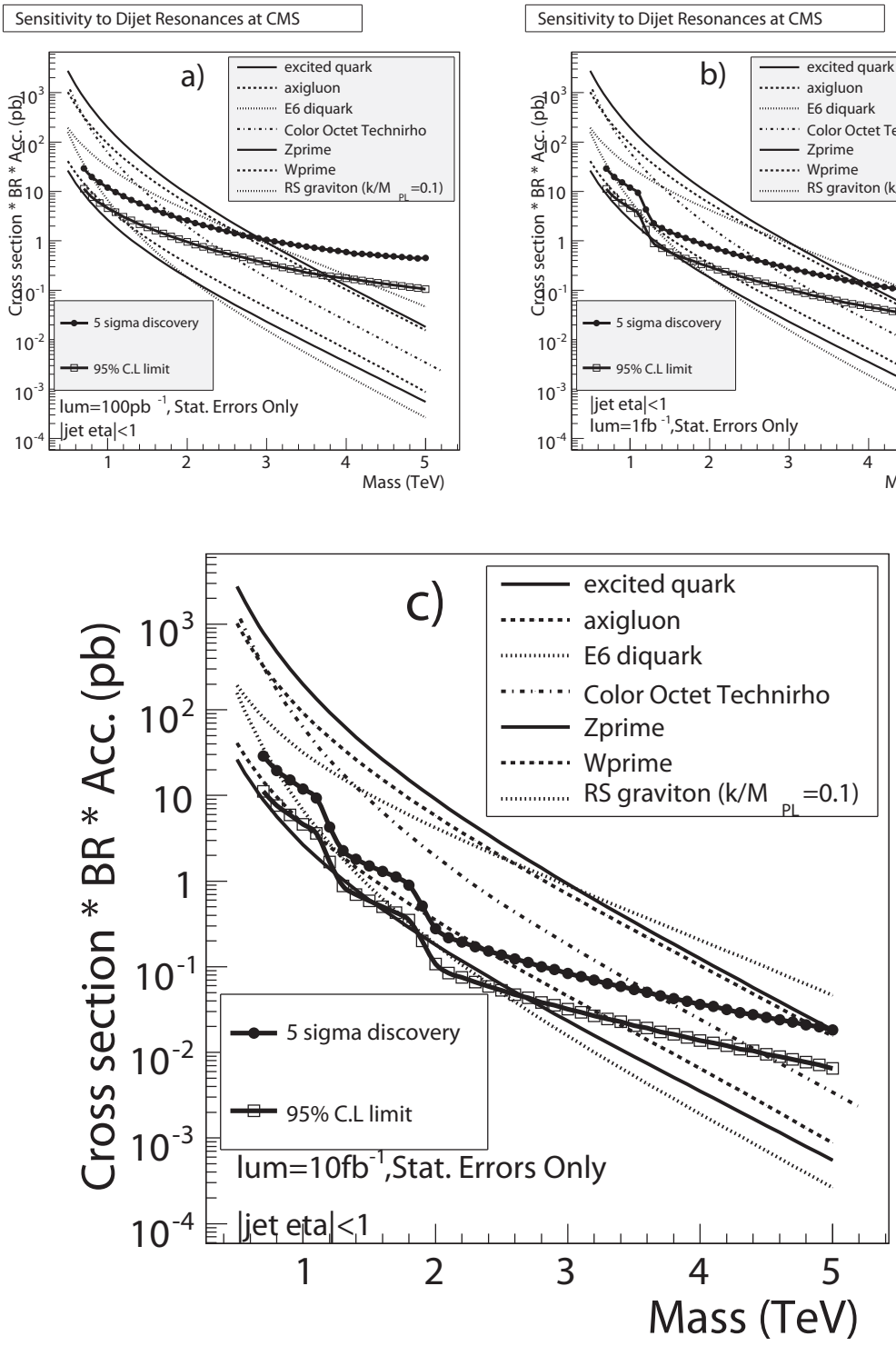

Figure 4.9: The dijet resonance sensitivity for 100 pb^{-1}(a), 1 fb^{-1}(b), and 10 fb^{-1}(c).The cross section of a resonance signal that could be discovered with 5σ significance (black dots) or excluded at 95% CL (open boxes) is compared to the cross section for various resonance models. These sensitivities contain statistical uncertainties only.

1. Jet energy scale

2. Jet energy scale and trigger prescales

3. Jet energy resolution

4. Radiation and resonance low mass tail

5. Luminosity

I determine each uncertainty due to each of the above source by measuring the 1σ change in the exclusion and discovery cross section. The total systematics is calculated by summing these 1σ changes in quadrature. Fig. 4.10 shows the individual systematics uncertainties and total systematic uncertainty as a fraction of signal cross section. One can measure the absolute uncertainty by multiplying this total systematics by the values of the exclusion or discovery cross section limits. Fig. 4.10 summarizes the individual systematic uncertainties and the total systematic uncertainty in our signal sensitivity for 10 fb^{-1}expressed as a fraction of the signal cross section.

4.7.1 Jet Energy Scale

There will be an uncertainty as to how well the jet energy scale in the simulation matches the jet energy scale in the experimental data. If the jet energy scale in the data is off by 5%, then the resonance could appear in our data at a 5% lower or higher mass than we expect. When it appears at 5% lower mass, it will be sitting on a much higher background. It will therefore be harder to find the resonance.

In this study, we use Monte Carlo for both the signal and background. Thus one might think that this uncertainty affects the background and the signal in the same way, shifting both to upper or lower dijet mass. However, in the actual experiment, we plan to use the data as background and Monte Carlo for the signal. We posit that we can not adequately determine the background by any Monte Carlo until we see the data. So there will be an uncertainty between the jet energy scales of signal

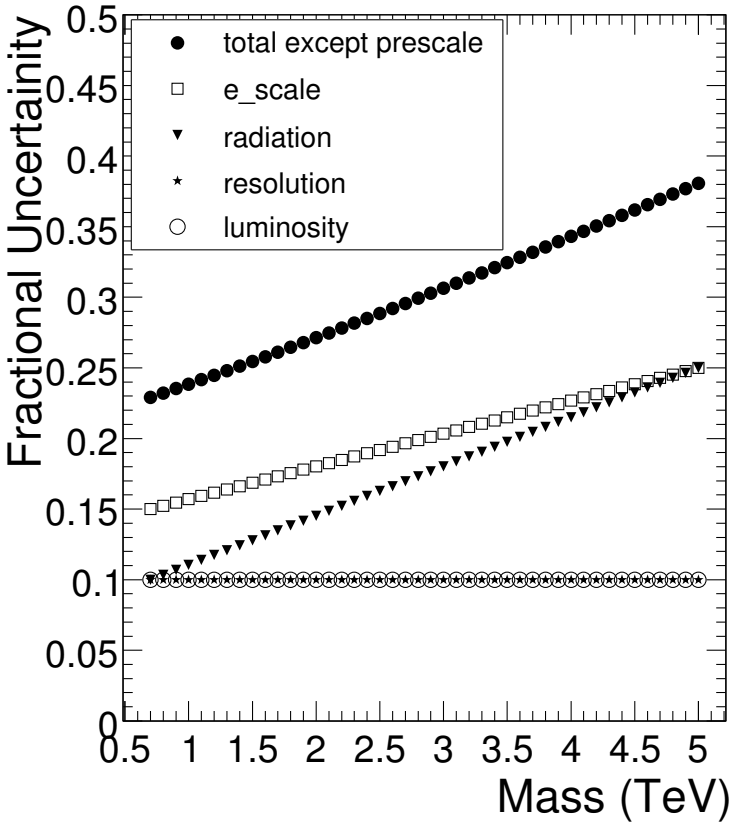

Figure 4.10: Fractional systematic uncertainties on signal cross section sensitivity. The uncertainties from smallest to largest are from luminosity (open circles), dijet mass resolution (stars), low mass tail of resonance including radiation (triangles), jet energy scale effect on QCD background (open boxes), and the total from these systematics added in quadrature (black dots). There is also a trigger prescale systematic from jet energy uncertainties which occurs for mass values of 0.7, 1.2, 1.3, 1.9, 2.0, and 2.1 TeV and is discussed in the text but not included in this plot.

(Monte Carlo) and the background (data). The jet energy scale uncertainty in the CMS is estimated to be ±5% [31, 36]. To estimate the effect of this systematic, I propagate it to our QCD events to see how much the QCD cross section changes if dijet mass changes ±5%. The systematic uncertainty on the cross section of the QCD background is given in [31]. It varies from about 30% at a dijet mass of 0.7 TeV to 60% at a dijet mass of 5 TeV.

I increase the QCD cross section by this systematics and recompute our cross

section limits for 10 fb^{-1}. Our cross section limits increase 15% at a resonance mass of 0.7 TeV to 25% at a resonance mass of 5 TeV, as shown in Fig. 4.10.

This is expected, because the increase in the background cross section will worsen our sensitivity and cause an increase in the cross section limits. Because the sensitivity is proportional to signal/$\sqrt{\text{background}}$, the increase in the limits should be approximately the value of the inverse of the square root of the increase in background.

Another way to check the jet energy scale systematic is to use the cross section sensitivity curves in Fig. 4.9. Moving each mass point to a point on the curve at 5% lower mass, we can see the effect of jet energy scale systematics on the signal cross section because moving the signal down to a 5% lower mass value while keeping the background is equivalent to raising the background underneath a fixed signal. Our check gives the same result as shown in Fig. 4.10 to within a few percent, except for the regions where the trigger prescale changes, which I discuss in the next section.

I repeat this check with the 1 $fb^{-1}$and the 100 pb^{-1} samples. The effects of the systematics are always equal to or lower than the one I observe in the 10 fb^{-1} sample, except the trigger prescale changes. These lower systematics effects are expected for lower integrated luminosity samples because the background number of events are smaller and the sensitivity is more accurately given by signal/$\sqrt{\text{signal} + \text{background}}$. To be conservative, I use the jet energy systematics of 10 fb^{-1}, for other integrated luminosity samples too.

4.7.2 Jet Energy Scale and Trigger Prescales

As mentioned in the previous section, I check the jet energy scale uncertainty by moving each mass point on the sensitivity curve to a point at 5% lower mass. Jet energy scale has its largest effect at dijet mass values just above where the trigger prescale changes. This is expected because if a resonance is contained within an unprescaled trigger, the sensitivity to the resonance will be more than if it is contained within a prescaled trigger. There will more events in the unprescaled region than in the prescaled region. An illustration of this is shown in the Fig. 4.8.b. The sensitivity

to the dijet resonance of 0.7 TeV gets better when the lower prescale region starts. This is essentially an edge effect of our measurement region.

The prescale changes at a dijet mass value of 0.67 TeV for the 100 pb^{-1} sample, at dijet mass values of 0.67 and 1.13 TeV for the 1 fb^{-1} sample, and at dijet mass values of 0.67, 1.13, and 1.80 TeV for the 10 fb^{-1} sample. The number of both signal and background events drops abruptly below these thresholds due to higher prescale. The amount of this effect is listed in Table 4.4. The systematic uncertainty is observed at 1.9, 2.0, and 2.1 TeV only for 10 fb^{-1}; at 1.2 and 1.3 TeV only for 1 fb^{-1} and 10 fb^{-1}; and at 0.7 TeV for 100 pb^{-1}, 1 fb^{-1}, and 10 fb^{-1}.

Mass (TeV)	energy-scale/prescale Systematic	Samples Affected
0.7	100%	100 pb^{-1}, 1 fb^{-1}, 10 fb^{-1}
1.2	70%	1 fb^{-1}, 10 fb^{-1}
1.3	60%	1 fb^{-1}, 10 fb^{-1}
1.9	70%	10 fb^{-1}
2.0	130%	10 fb^{-1}
2.1	30%	10 fb^{-1}

Table 4.4: Energy-scale/prescale systematic uncertainty. For the resonance masses where exists this systematic uncertainty, the value of the systematic uncertainty and the samples to which the systematic uncertainty applies are listed.

4.7.3 Jet Energy Resolution

There is an uncertainty in dijet mass resolution which affects our cross section limits. If the dijet mass resolution is wider than we expect, it may be harder to find a narrow resonance because it will be spread over more bins.

I investigate the full effect of the calorimeter to measure the uncertainty. For this purpose, I compare the resonance shape from reconstructed jets (RecJets) with the one from particle level jets (GenJets). Fig. 4.11 shows the dijet mass distribution from a resonance using GenJet and RecJets.

The calorimeter has two effects on the dijet mass resonances line shape: First, the GenJets have better resolution than the RecJets. It is clear that the GenJet

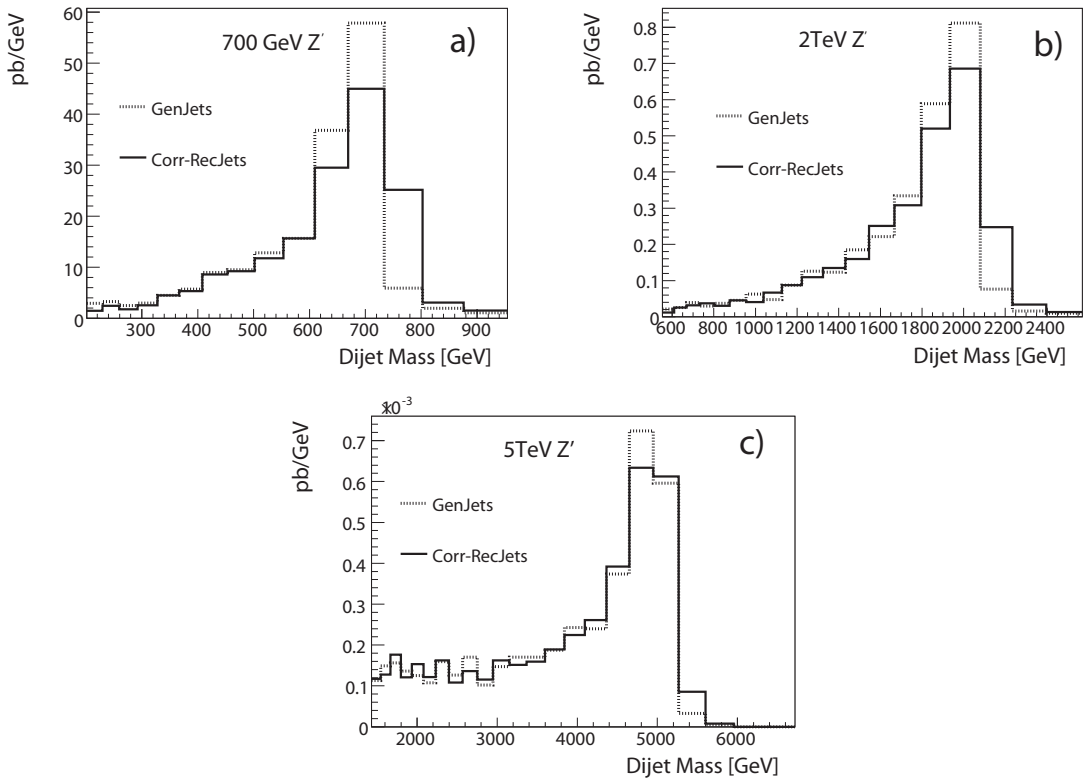

Figure 4.11: Dijet resonances of mass 0.7 TeV (a), 2.0 TeV (b) and 5.0 TeV (c) from GenJets reconstructed from MC particles (dotted) is compared to resonances reconstructed using the standard measured and corrected dijets (solid).

distribution is narrower. The events are spread over fewer bins. This lowers the cross section limits because the signal-to-background ratio increases. Second, the mean dijet mass from the GenJets peak is shifted slightly to lower mass. This raises the cross section limits because of the energy scale systematic.

We use the GenJets to compute new values for the cross section limits and discovery values for 10 fb^{-1}. Our cross section limits are reduced by only about 5% when using GenJets except near the prescale thresholds. The increase at the prescale thresholds confirms the small mass shift between dijet masses made with GenJets and those made with RecJets. This shift varies from about 2% at 0.7 TeV to about 0.6% at 5 TeV. By comparing this mass shift to the results of the jet energy scale systematics, I determine that the mass shift increases the cross section limits by about

5%.

The first 5% change comes from two effects: one from the small mass shift that raises the cross section limits by 5% and the other from the improved resolution that is found to be 10%. I take this 10% effect of the calorimeter as a systematic uncertainty on the resolution, which is most likely an overestimate, and use it as shown in Fig. 4.10 for all luminosities.

4.7.4 Radiation and Resonance Low Mass Tail

The long tail to low mass in the resonance shape constitutes another source of systematics. This tail is mostly caused by QCD radiation. When the final state quark emits a gluon with an angle far from quark direction, it causes a loss in the energy of the jet. The amount of this radiation is uncertain, and it could be somewhat different from model to model depending on the type of resonance, including whether the resonance decays to quarks or gluons. The second source of this tail is caused by the huge parton distributions at very low dijet mass for high mass resonances. In Fig. 4.12, we observe a long low mass tail at the generator level for a 5 TeV Z' resonance but not for a 2 TeV Z' resonance. The size of this tail also depends on the the kind of partons in the initial state.

To estimate all these uncertainties, in the long tail to low mass, I narrow the range of dijet mass from $0.3M < m < 1.3M$ to $0.7M < m < 1.3M$, forcing the total cross section to be the same in both cases. I use the symmetric dijet mass distribution $0.7M < m < 1.3M$ to compute the new values for the cross section limits and discovery values for 10 fb^{-1}. The cross sections decrease by the fractional values shown in Fig. 4.10.

Since the total cross section is the same in the symmetric case as in the default case, the total resonance cross section is concentrated around the resonance mass. Therefore, the signal-to-background ratio increases. So does the sensitivity. The sensitivity increases from 10% at $M = 0.7$ TeV to 25% at $M = 5.0$ TeV. I use this systematic for all luminosities.

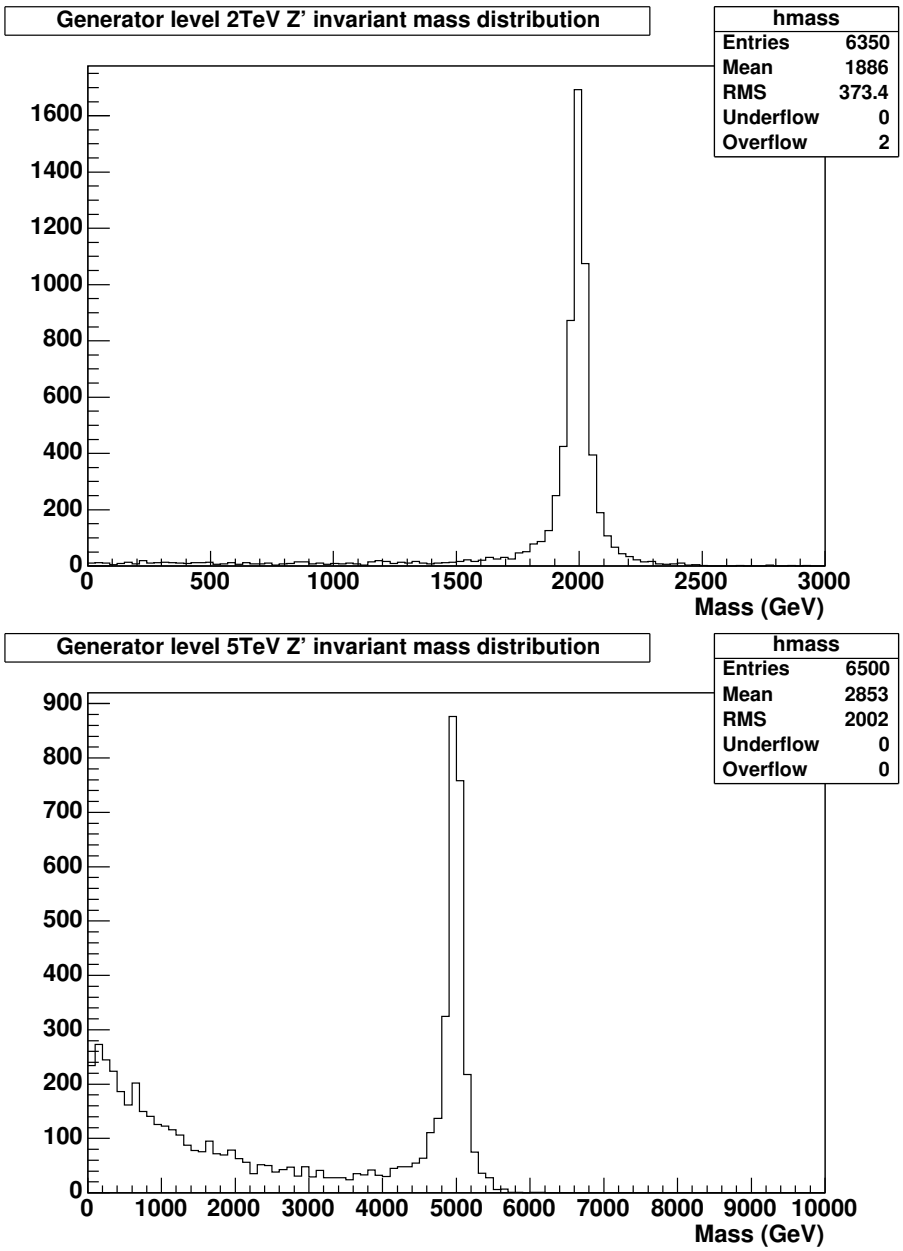

Figure 4.12: Z' resonances at the generator level for pole mass 2.0 TeV (Top Plot) and 5.0 TeV (Bottom Plot). The horizontal axis is the output resonance mass, $\sqrt{\hat{s}}$, resulting from the specified pole mass.

4.7.5 Luminosity

The CMS expects the uncertainty in luminosity to be around 10% [31]. This uncertainty in luminosity directly affects the number of events. Thus, it does affect

the cross sections, which we seek to estimate for our sensitivities and comparison of the models.

4.8 Sensitivity Including the Systematic Uncertainties

I convolute likelihood functions with the Gaussian systematic uncertainties to estimate the exclusion and discovery cross sections with systematic uncertainties. The width of the Gaussian systematic at any value of resonance mass is given by the exclusion (discovery) cross section in Fig. 4.9 times its fractional uncertainty given in Fig. 4.10.

After convoluting the systematics uncertainties, the previously 5σ discovery cross section with statistical errors only degrades and becomes significantly less than 5σ. I increase the cross section of the resonance until the discovery likelihoods with systematics are once again 5σ away from zero. Fig. 4.13 shows the resulting exclusion and discovery likelihoods for a 2 TeV resonance and 1 fb^{-1} of data. In this particular sample, systematics increases the exclusion cross section by 15% and discovery cross sections by 70%. Clearly, systematic uncertainties have a much greater effect on the discovery likelihoods than the exclusion likelihoods. This could be understood as follows: When there is no signal in the data, statistics dominate the uncertainty in the measurement of a signal cross section. When there is a large signal at the level of discovery, systematics dominate the uncertainty in the the measurement of the signal cross section.

I convolute all exclusion likelihoods with the Gaussian systematic uncertainties and find the new exclusion cross sections for each integrated luminosity. The value of the 95% CL excluded cross section increases by 10% at low resonance mass and 25% at the highest resonance mass, independent of integrated luminosity, except for the mass regions just above the prescale thresholds. Similarly, for each integrated luminosity, all discovery likelihoods are convoluted with the Gaussian systematic uncertainties and find the new discovery cross sections. The value of the 5σ discovery cross section increases by 50% at low resonance mass and 110% at the highest resonance mass,

independent of integrated luminosity, except for the mass regions just above the prescale thresholds.

Table 4.5 lists the cross section sensitivities with both statistical and systematic uncertainties. In Fig. 4.14, these sensitivities are compared to the lowest order predictions for the resonance cross sections in seven different models. For any resonance model, I can read off the expected mass range for either a 95% CL exclusion or a 5σ significance discovery. The mass sensitivities are tabulated in Table 4.6.

4.9 Summary

In three instantaneous luminosities, 10^{32}, 10^{33}, and 10^{34} $\mathrm{cm}^{-2}\mathrm{s}^{-1}$, and the corresponding integrated luminosities of 100 pb^{-1}, 1 fb^{-1}, and 10 fb^{-1}, the overall sensitivity to narrow resonances decaying into dijets is investigated. This is a generic resonance search, not concentrating on any particular model. The CMS sensitivity to narrow resonances is estimated in the presence of systematics. The cross section for a narrow dijet resonance that the CMS can expect to discover at a 5σ significance or to exclude at a 95% confidence level has been presented for each integrated luminosity and for each accessible resonance mass.

I compare the cross section sensitivities with the expected cross sections from models of excited quarks, axigluons, colorons, E_6 diquarks, color octet technirhos, W', Z', and Randall-Sundrum gravitons to determine the mass range for which we expect to be able to discover or exclude these models of dijet resonances. The mass ranges are listed in Table 4.6.

The resonances with higher cross sections have a naturally higher probability of being discovered. For excited quarks, axigluons, colorons, E_6 diquarks, and color octet technirhos, I find that a 5σ discovery of a multi-TeV dijet resonance is possible for all the luminosities considered. The first three models are produced via the color interaction, and E_6 diquarks are produced from the valence quarks of each proton, giving large cross sections. For W', Z', and the Randall-Sundrum graviton, I find that a 5σ discovery cannot be projected with confidence for any of the luminosities

considered. The first two of these models employ electroweak couplings, and the Randall-Sundrum graviton is generally considered likely for similar strengths of coupling, and all three of these models include one or more partons that are not valence quarks of the proton. Nevertheless, for all the models considered, there is some range of mass that can be excluded at 95% CL if the data are in good agreement with the QCD expectations.

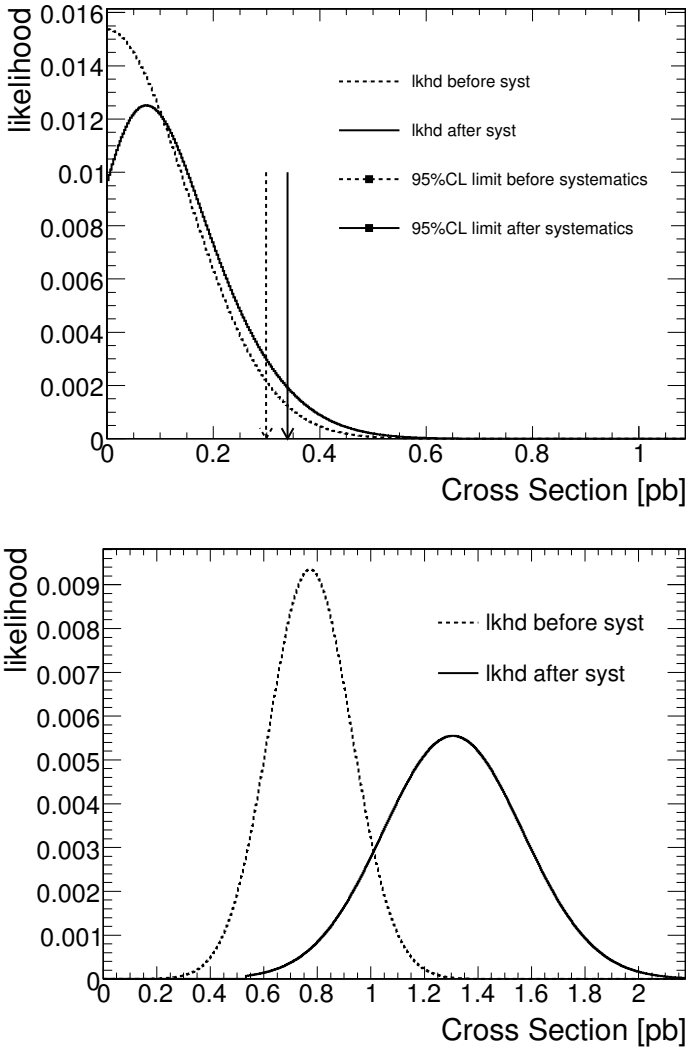

Figure 4.13: Likelihoods for observing a narrow dijet resonance of mass 2 TeV/c^2 in a 1 fb^{-1} data sample that contain only the QCD background (top) and a data sample that also contains a resonance with a significance of 5σ (bottom). The likelihoods with statistical uncertainties only (dashed curve) are compared to the likelihood with both statistical and systematic uncertainties (solid curve).

M	95% CL Exclusion (pb)			5σ Discovery (pb)		
TeV/c^2	100 pb^{-1}	1 fb^{-1}	10 fb^{-1}	100 pb^{-1}	1 fb^{-1}	10 fb^{-1}
0.7	26	26	26	150	150	150
0.8	8.4	8.4	8.4	30	30	30
0.9	6.5	6.5	6.5	23	23	23
1.0	5.1	5.1	5.1	19	19	19
1.1	4.2	4.0	4.0	15	15	15
1.2	3.4	3.1	3.1	13	13	13
1.3	2.9	1.5	1.5	11	7.7	7.7
1.4	2.4	0.79	0.77	9.2	2.9	2.9
1.5	2.1	0.66	0.65	7.9	2.5	2.4
1.6	1.8	0.56	0.56	6.9	2.1	2.1
1.7	1.6	0.49	0.49	6.1	1.9	1.8
1.8	1.4	0.44	0.40	5.4	1.7	1.5
1.9	1.2	0.38	0.37	4.8	1.5	1.5
2.0	1.1	0.34	0.32	4.4	1.3	1.3
2.1	0.95	0.30	0.11	3.9	1.2	0.50
2.2	0.86	0.27	0.085	3.6	1.1	0.33
2.3	0.77	0.24	0.076	3.3	0.95	0.30
2.4	0.70	0.22	0.068	3.0	0.86	0.27
2.5	0.64	0.19	0.061	2.8	0.78	0.24
2.6	0.58	0.18	0.055	2.5	0.71	0.22
2.7	0.54	0.16	0.050	2.4	0.66	0.20
2.8	0.49	0.14	0.045	2.2	0.60	0.18
2.9	0.45	0.13	0.042	2.1	0.56	0.17
3.0	0.41	0.12	0.038	1.9	0.51	0.15
3.1	0.37	0.11	0.034	1.8	0.48	0.14
3.2	0.34	0.10	0.032	1.7	0.44	0.13
3.3	0.31	0.093	0.029	1.6	0.41	0.12
3.4	0.29	0.087	0.027	1.5	0.39	0.11
3.5	0.27	0.080	0.025	1.5	0.36	0.10
3.6	0.25	0.074	0.023	1.4	0.34	0.10
3.7	0.24	0.068	0.021	1.3	0.31	0.089
3.8	0.23	0.064	0.020	1.3	0.30	0.084
3.9	0.22	0.060	0.018	1.2	0.28	0.078
4.0	0.21	0.055	0.017	1.2	0.26	0.073
4.1	0.20	0.053	0.016	1.1	0.25	0.069
4.2	0.19	0.049	0.015	1.1	0.24	0.064
4.3	0.18	0.046	0.013	1.1	0.23	0.060
4.4	0.17	0.044	0.013	1.1	0.22	0.057
4.5	0.16	0.041	0.012	1.0	0.21	0.053
4.6	0.16	0.039	0.011	1.0	0.20	0.050
4.7	0.15	0.036	0.010	0.99	0.19	0.048
4.8	0.14	0.034	0.010	0.98	0.18	0.045
4.9	0.14	0.032	0.0090	0.96	0.17	0.043
5.0	0.13	0.030	0.0081	0.98	0.17	0.040

Table 4.5: Cross section sensitivity to dijet resonances with 100 pb^{-1}, 1 fb^{-1}, and 10 fb^{-1}. For each mass of narrow dijet resonance considered, I list the cross section that we expect to be able to exclude at 95% CL and the cross section that we expect to be able to discover with 5σ significance.

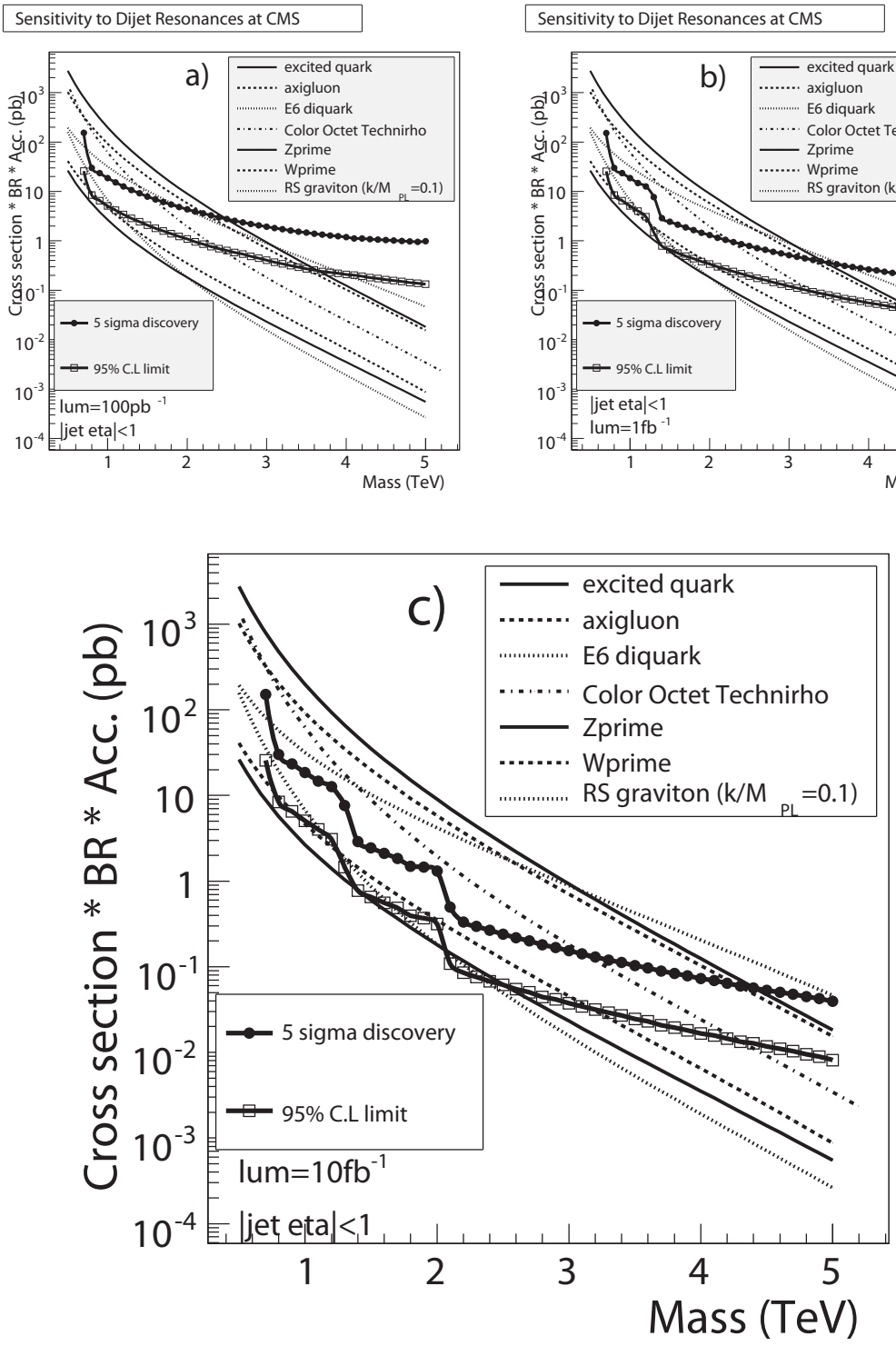

Figure 4.14: Dijet resonance sensitivity for 100 pb^{-1}(a), 1 fb^{-1}(b), and 10 fb^{-1}(c). The cross section of a resonance signal that could be discovered with 5σ significance (solid circles) or excluded at 95% CL (open boxes) is compared to the cross section for various resonance models. These sensitivities contain both statistical and systematic uncertainties.

Resonance Model	95% CL Excluded Mass (TeV/c^2)			5σ Discovered Mass (TeV/c^2)		
	100 pb^{-1}	1 fb^{-1}	10 fb^{-1}	100 pb^{-1}	1 fb^{-1}	10 fb^{-1}
Excited Quark	0.7 - 3.6	0.7 - 4.6	0.7 - 5.4	0.7 - 2.5	0.7 - 3.4	0.7 - 4.4
Axigluon or Coloron	0.7 - 3.5	0.7 - 4.5	0.7 - 5.3	0.7 - 2.2	0.7 - 3.3	0.7 - 4.3
E_6 diquark	0.7 - 4.0	0.7 - 5.4	0.7 - 6.1	0.8 - 2.0	0.8 - 3.7	0.8 - 5.1
Color Octet Technirho	0.7 - 2.4	0.7 - 3.3	0.7 - 4.3	0.7 - 1.5	0.7 - 2.2	0.7 - 3.1
Randall-Sundrum Graviton	0.7 - 1.1	0.7 - 1.1 1.3 - 1.6	0.7 - 1.1 1.3 - 1.6 2.1 - 2.3	N/A	N/A	N/A
W$'$	0.8 - 0.9	0.8 - 0.9 1.3 - 2.0	0.8 - 1.0 1.3 - 3.2	N/A	N/A	N/A
Z$'$	N/A	N/A	2.1 - 2.5	N/A	N/A	N/A

Table 4.6: Sensitivity to dijet resonances with 100 pb^{-1}, 1 fb^{-1}, and 10 fb^{-1}. For each resonance model, I show the range of masses we expect to be able to exclude at a confidence level of 95% or greater and the range of masses we expect to be able to discover with a significance of 5σ or greater. Multiple entries indicate multiple mass regions to exclude the resonance for the same integrated luminosity. All estimates are with both statistical and systematic uncertainties.

CHAPTER 5
THE ANALYSIS OF 2006 COMBINED ECAL+HCAL TEST BEAM DATA

5.1 Introduction

In this chapter, I present the analysis results of the CMS combined (ECAL+HCAL) calorimeter test beam data collected at CERN in the summer of 2006. Our analysis consists of two parts: measurement of the CMS calorimeter response to beam particles [37, 38] and the response to high energy jets, based on test beam data [39].

5.2 The Calorimeter Response To Single Particles

5.2.1 The H2 Beam Line and Particle Identification

The test beam experiment was conducted at the H2 beam line, which is pictured in Fig. 5.1. The beam line provides 400 GeV/c protons from the Super Proton Synchrotron (SPS). To produce different particles such as pions and electrons, a production target (T2) was placed at 590.9 m. Striking protons produce various particles of momentum between 10 and 350 GeV/c. Maximum usable momentum for electrons is 100 and for pions 350 GeV/c. To produce very low energy (VLE) particles with momentum range between 1 and 9 GeV/c, another target T22 was placed 97 m upstream of the calorimeters. The produced particles were forced to follow a dog-leg path for momentum selection and particle identification, as shown in Fig. 5.1.

In the beam line, there were six wire chambers (WC1 through WC3 and WCA through WCC). They provided the tracking information of particles. The wire chambers had a spatial resolution ~ 350 μm in both $x-$ and $y-$coordinates. Four scintillation counters (S1 through S4) were used for triggering. The beam trigger typically consisted of the coincidence S1·S2·S4, which defined a 4×4 cm^2 area on the front face of the calorimeter. The S4 counter was used to eliminate multi-particle events off-line since it gave a clean pulse height distribution of single and multiple particles in the beam. Four beam halo counters (BH1 through BH4) were used to veto beam halo and wide angle particles that originated in the beam line. Each measured 30×100

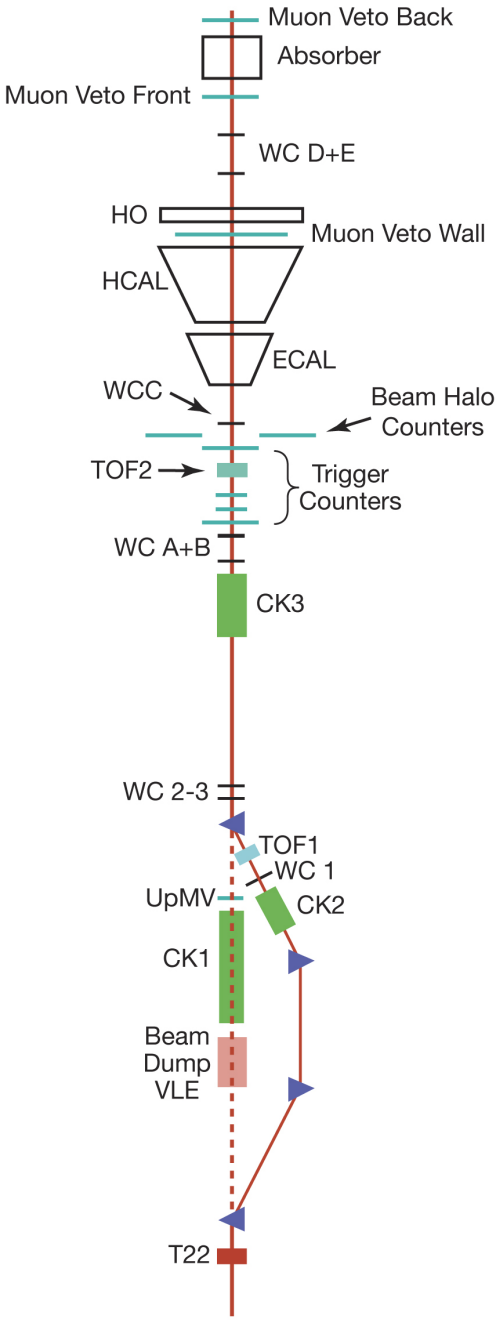

Figure 5.1: The CERN H2 beam line and the experimental setup are shown schematically. In the very low energy (VLE) mode, the tertiary target (T22) and a beam dump were inserted into the beam line and the low energy particles were steered through the dog-leg.

cm^2; they were arranged such that the beam passed through a 7×7 cm^2 opening.

To identify particles in the VLE mode, two Cherenkov counters (CK2 and CK3), two time-of-flight counters (TOF1 and TOF2), and muon counters (Muon Veto Wall, Muon Veto Front, and Muon Veto Back) were used.

The CK2 is a 1.85-m long Cherenkov counter filled with CO_2. It was used to tag electrons in the VLE mode. At the 0.7 bar, no other charged particles except electrons gave a signal. The CK3 was filled with Freon134a. The CK3 pressure was set to 0.88 bar at low beam momenta ($p_b \leq 3$ GeV/c) to tag electrons. At higher momenta the CK3 was kept at the 1.2 bar to identify pions.

Kaons, protons, and antiprotons were identified using time-of-flight counters (TOF1 and TOF2) after electrons and pions were selected by using the CK2 and CK3. Time-of-flight counters were separated by $\sim$ 55 m. Each plate measured 10×10 cm^2. Time resolution was $\sim$300 ps. Protons and kaons were successfully separated from pions up to 7 GeV/c. Fig. 5.2 and Fig. 5.3 display the identified particles in 3 and 8 GeV/c negative hadron beams.

To tag muons, Muon Veto Front (MVF), Muon Veto Back (MVB), and Muon Veto Wall (MVW) counters were used. The MVF and MVB were (80×80 cm^2) scintillation counters. They were placed well behind the calorimeters. The MVW consisted of eight individual scintillation counters, each measuring 30 × 100 cm^2, placed between the HB and HO. They were used to tag low momentum (2-5 GeV/c) beam muons. The MVW was also used to study the details of late developing showers (see Section 5.2.2).

In the test beam, one ECAL super module (EB), two HCAL barrel (HB1 and HB2) wedges, four HCAL endcap (HE) segments, and an HO detector were used. The whole calorimeter system was placed on a rotating platform, as shown in Fig. 5.4.

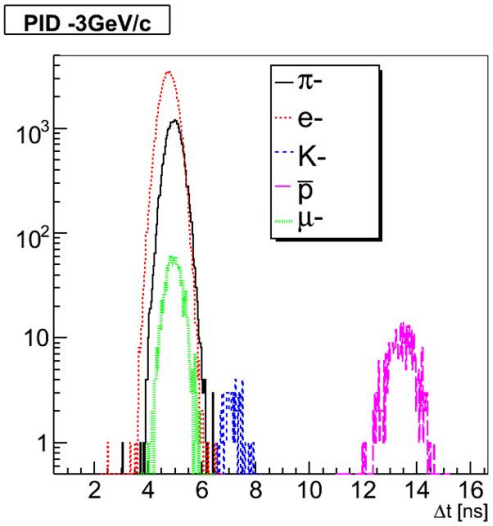

Figure 5.2: The particle identification was carried out with two Cherenkov counters (CK2 and CK3), two time-of-flight counters (TOF1 and TOF2), and muon veto wall counters (MVB) in the VLE mode. The 3 GeV/c negative beam is shown as an example above.

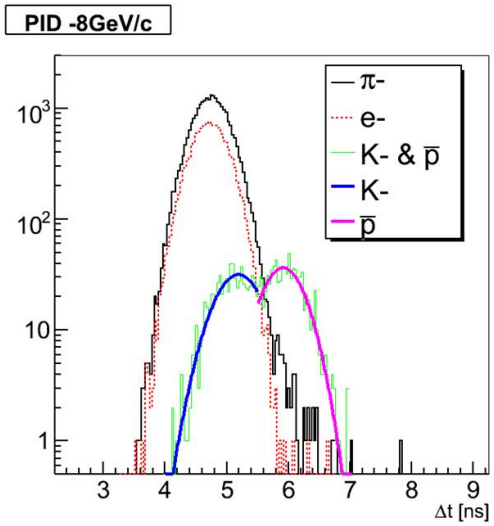

Figure 5.3: The same as Fig. 5.2 but for a 8 GeV/c negative beam (see text for details).

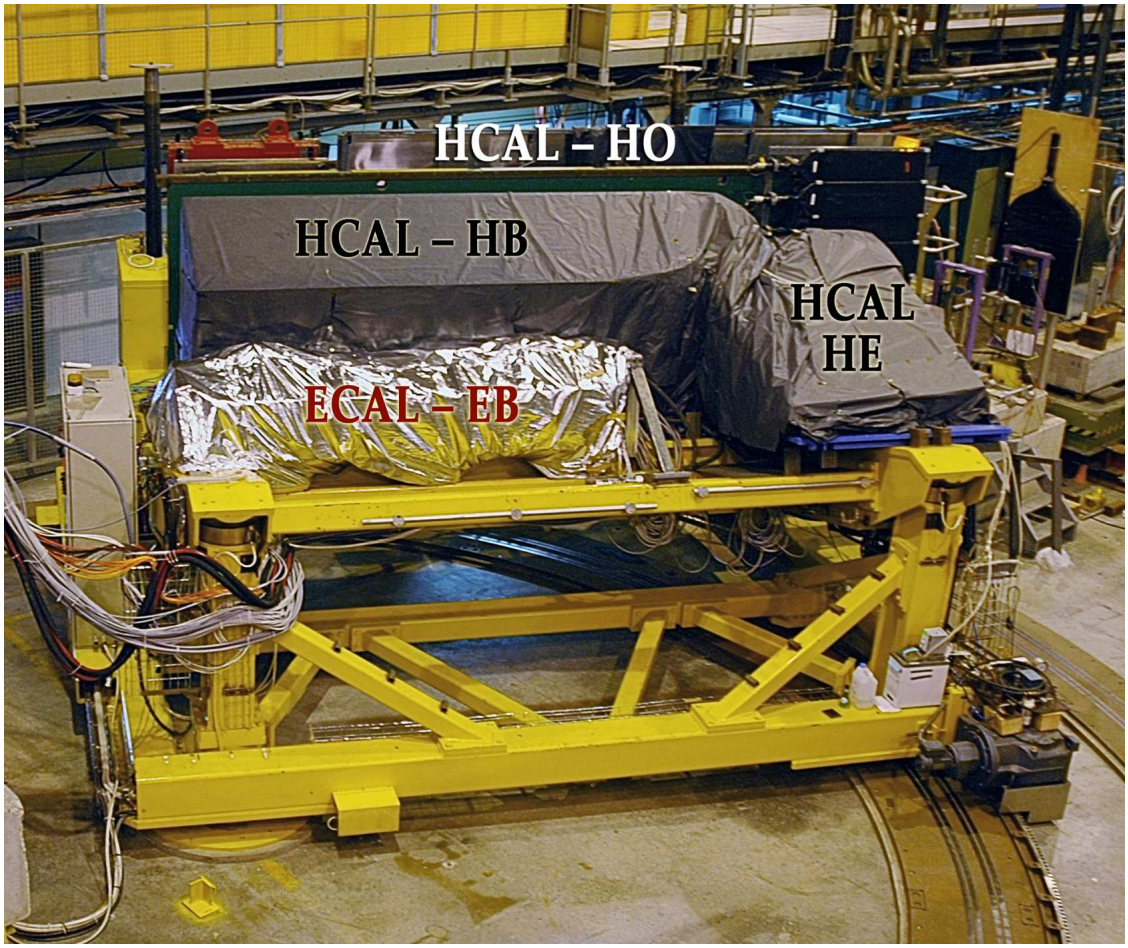

Figure 5.4: EB, HB, and HE calorimeters are shown on a rotating platform at the H2 beam line.

5.2.2 The Response of the Combined Calorimeter System to Particles

The response of a calorimeter to a particle is measured as the ratio of the collected signal from the calorimeter over the initial energy of the particle, normalized to 1 for electrons. To measure the response correctly, one has to calibrate the calorimeters. Both the EB and HB were calibrated using 50 GeV/c electrons. The HB calibration was carried out before the EB super module was mounted in front of it. It is possible to use pions to calibrate the HB; however, we preferred to use electrons, instead. The reason will be explained later in this section.

The EB signal was collected from 7×7 crystals around the beam position. The HB signal was collected from 3×3 towers. Muon-Veto-Walls (MVW) were used to reconstruct the leakage energy behind the HB in case of high energy particles. Indeed, one has to use the Hadron Outer (HO) calorimeter to measure it in the CMS. However, we utilized the MVW to measure the energy leakage since the beam spot we analyzed is covered more by the MVW than by the HO in this experiment.

Fig. 5.5 shows the EB, HB, and total signals, including the leakage for the 5 and 100 GeV/c π^- beams. The left plots (a) and (d) show the EB signals. The first peak in these plots is caused by the pions that start showering late and deposit most of their energy in the HB. The second peak indicates the pions that start showering early and deposit some fraction of their energy in the EB. The middle plots (b) and (e) show the signal distribution from HB. The peaks indicate the early (first peak) and late (second peak) showering pions.

Fig. 5.6 shows the combined response of the CMS EB+HB calorimeters to a variety of particles in a wide range of momenta ($1 \leq p_b \leq 350$ GeV/c) as a function of beam momentum. At 5 GeV/c, the antiproton response is $\sim 70\%$ of the electron response. Pion and proton responses are 62% and 47% of the electron response, respectively. Although these particles have the same momenta, the available energy that is converted to the calorimeter signal is different for each one of them. To first order, for pions and kaons, the available energy is their kinetic energy plus the rest mass; for protons, it is only the kinetic energy. On the other hand, for antiprotons, the

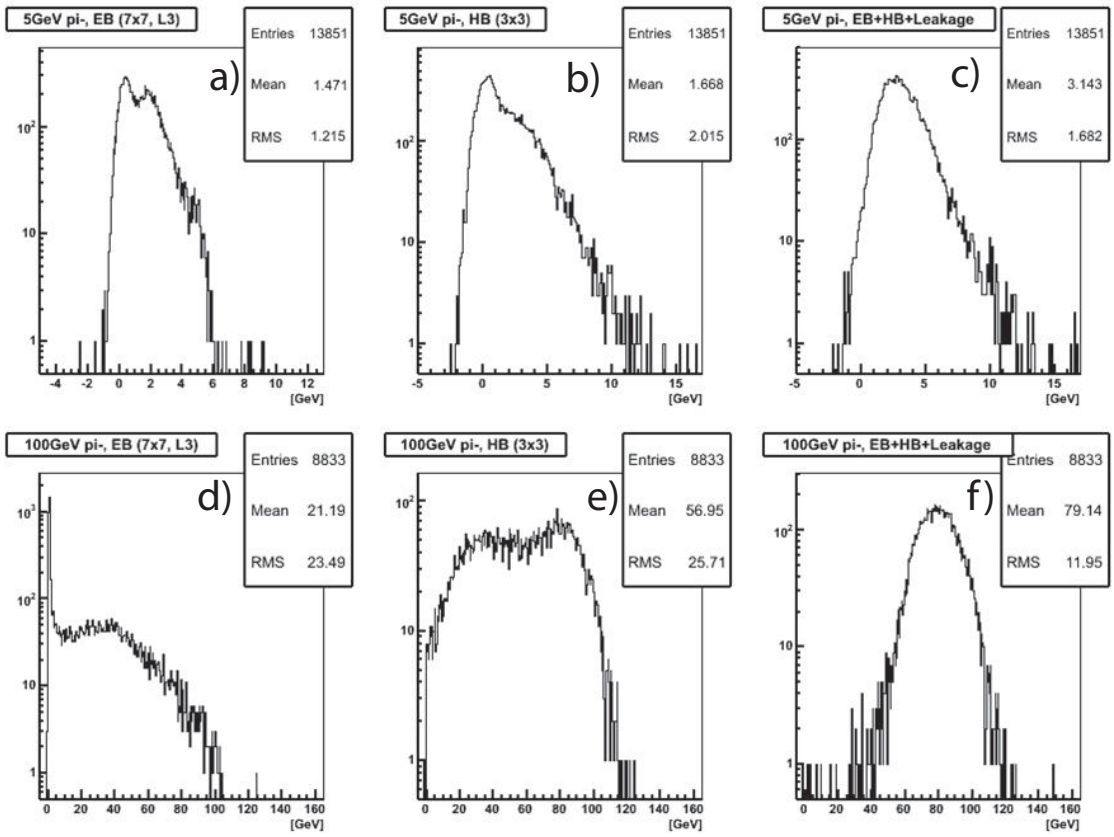

Figure 5.5: The response functions for 5 and 100 GeV/c negative pions are shown above for the EB (a and d), HB (b and e), and the sum of all signals from the combined system (c and f), which also includes the energy leakage from the back of the HB.

available energy for a calorimetric signal equals the kinetic energy plus twice the rest mass of proton because an antiproton annihilates with a proton, giving a measurable signal. In Fig. 5.7, the same data are plotted against the available energy for signal production.

Before I present the response differences to electrons, muons, and hadrons, it is important to note that if we had elected to calibrate the EB with electrons and the HB with penetrating pions, the total calorimeter response would be systematically larger compared to what is shown in Fig. 5.7. Because the weight to be used for the HB signal would be greater than the unity, this would increase the nonlinearity of the

system. Since high energy pions on average deposit more energy in the HB, they are more affected by this than are low energy pions. Second, this approach would have introduced an undesired bias in the reconstructed energy, depending on the starting point of the showers. Pions that shower early and pions that shower late have a different fraction of energies deposited into the HB. Thus, this method would increase the difference between the responses to early and late starting showers. Third, pion calibration of the HB is only correct at the pion energy at which the calibration is performed. Additional corrections for pions of other energies would have been needed.

As shown in Fig. 5.7, the response of the calorimeter to electrons is linear within $\pm 2\%$ over the full momentum range of 1 to 100 GeV. A 2 GeV muon generates 70% response with respect to an electron. A 5 GeV generates 38% response. As the momentum of a muon increases, the calorimeter response decreases because a muon acts more like a minimum ionizing particle at high momentum. On the other hand, the muon with 2 GeV momentum deposits most of its energy in the calorimeter. We couldn't observe a signal for a 1 GeV muon because it ranges out in the calorimeter absorber. Fig. 5.8 shows the signals observed by one MVW counter for four low energy pion beams. At 1 GeV/c, there is no muon behind the calorimeters. At 2 GeV, in addition to the minimum ionizing particle (*mip*) signal, we observe some energy leakage. The energy leakage is due mainly to neutrons exiting the back of the HB. At 9 and 50 GeV, leakage in the form of *mip*s and neutrons is clearly increased.

A detailed analysis of the combined calorimeter response to hadrons shown in Fig. 5.7 is presented below:

The response to π^+ is systematically larger than that to the π^- as the energy decreases. This can be understood from the characteristics of the charge exchange reactions, $\pi^+ + n \rightarrow \pi^0 + p$ (I) and $\pi^- + p \rightarrow \pi^0 + n$ (II). In these reactions, a large fraction of the pion energy is carried by the final-state π^0, which develops electromagnetic showers. Therefore, the calorimeter response to pions interacting this way is close to 1. Since the target material ($PbWO_4$) contains about 50% more neutrons than protons, the relative effect of reaction (I) will be larger than that of

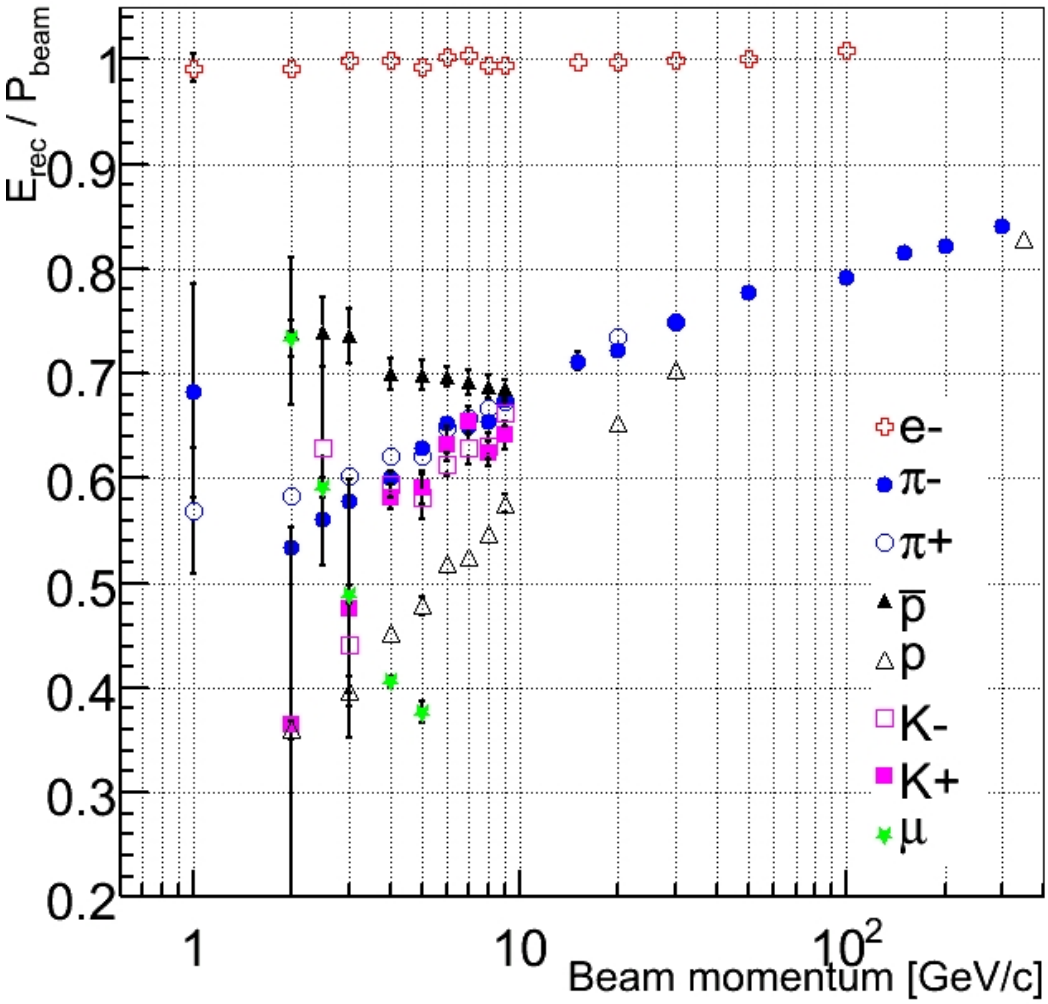

Figure 5.6: The response of the combined calorimeter systems to eight different particles is shown as a function of the beam momentum. Both the EB and HB are calibrated with 50 GeV/c electrons.

reaction (II); therefore, the calorimeter response to π^+ should be expected to be larger than the π^- response.

The response to pions is systematically higher than the proton response. This effect can be explained by the fact that proton-induced showers, on average, favor the production of leading baryons instead of π^0s due to the baryon number conservation

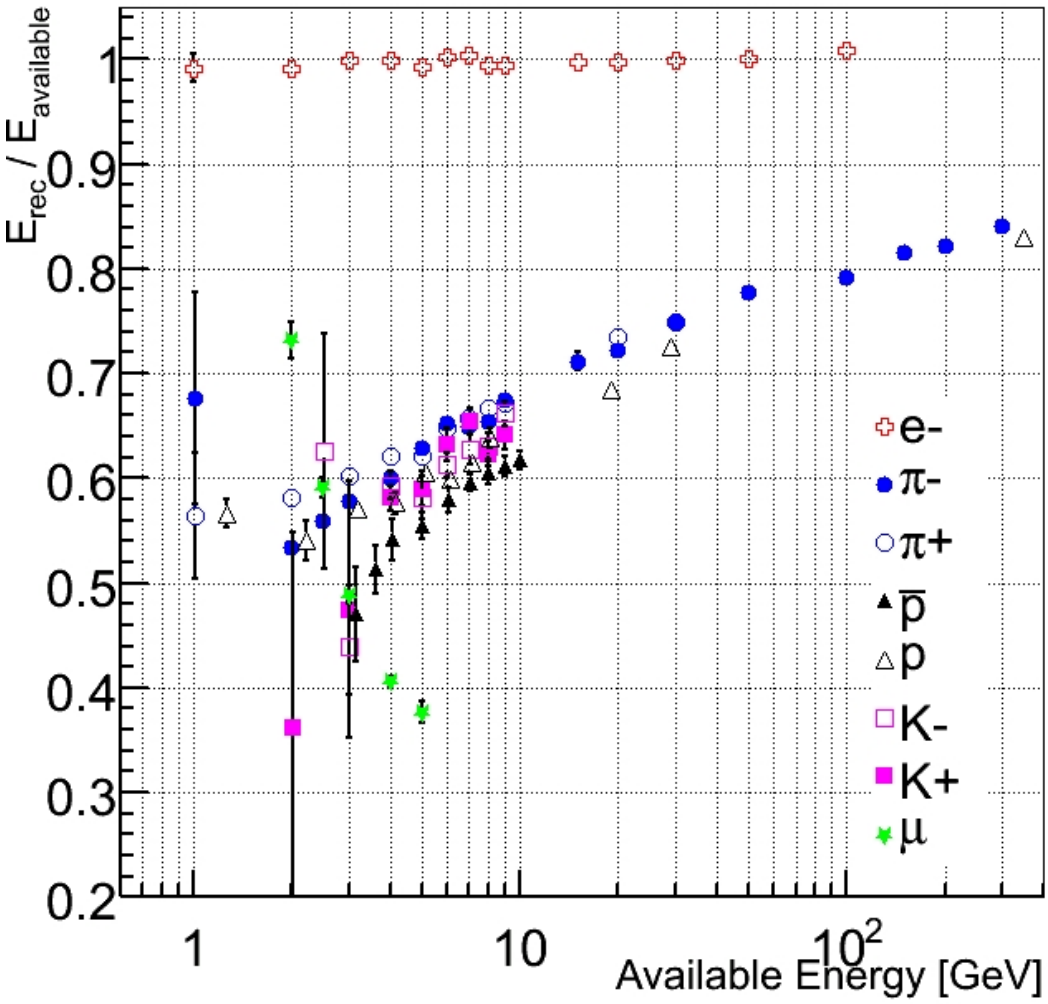

Figure 5.7: The same data as in Fig. 5.6 but the calorimetry response is plotted against the available energy.

requirement, while pion-induced reactions have leading π^0s more often.

The antiproton response is systematically smaller than the pion response (Fig. 5.7). Antiprotons are more likely to start showering in the EB compared to pions due to their bigger total cross section. Pions, on average, deposit a larger fraction of their energy in the HB. Since the e/h value of the HB is smaller than that of the EB, the pions benefit more from the increased response to the non-em shower components.

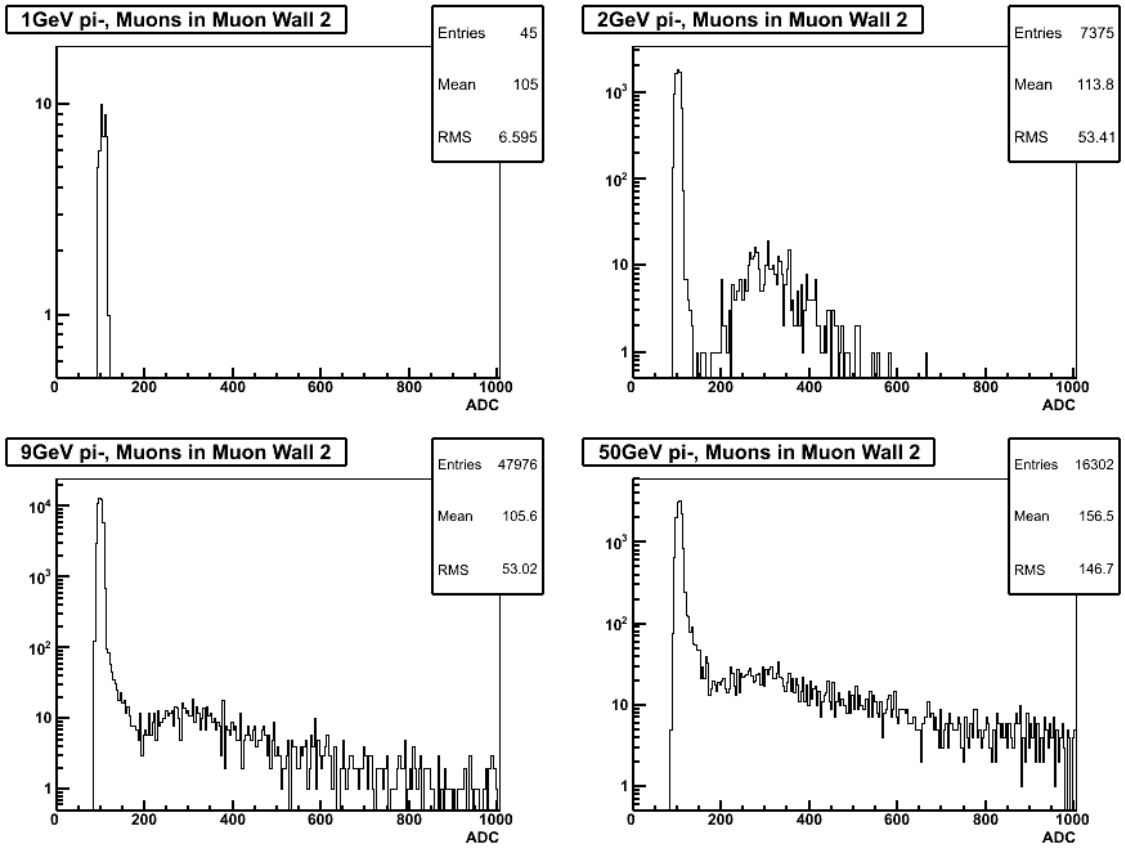

Figure 5.8: The signal distribution from a MVW clearly demonstrates that muons with less than 2 GeV range out in the calorimeters. As the beam energy is increased, the energy leakage also increases, as evidenced by the high-side tail of the pedestal peak.

The response to kaons is, on average, lower than the pion response. We surmise that kaon-induced showers preclude the production of leading π^0s due to strangeness conservation and therefore limit the average em shower fraction. Our statistics are insufficient to verify the latter effect.

5.2.3 Average Energy Sharing between the EB and HB

Fig. 5.9 shows the average energy sharing between the EB and HB for pions and (anti)protons. At low energies, a significant fraction of the available energy is deposited in the EB. A 2 GeV pion, on average, deposits 60% of its energy in the EB.

The EB calorimeter represents a significant absorber in front of the HB ($\sim 1\lambda_{\text{int}}$).

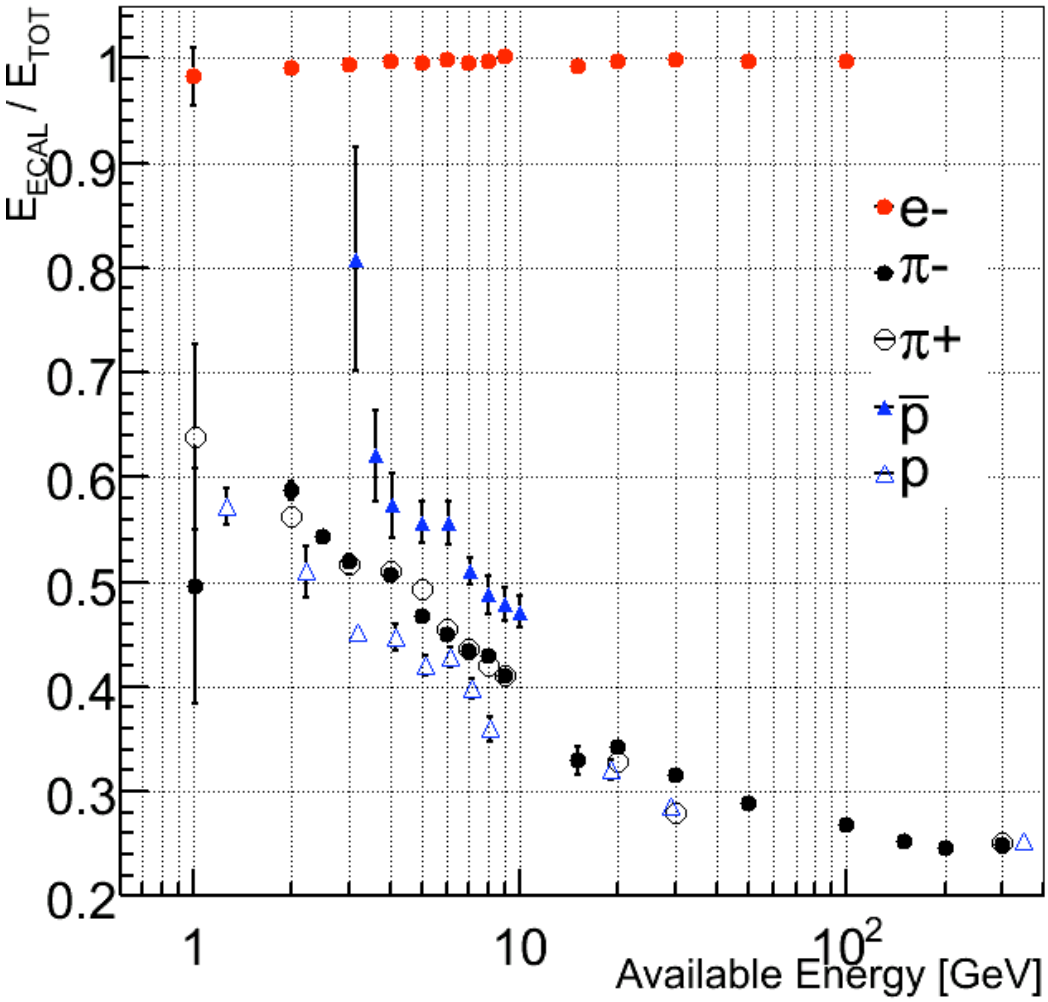

Figure 5.9: The fraction of energy deposited in the EB is plotted against the available energy for electrons, charged pions, and (anti)protons. The total energy is the sum of energies observed by the EB, HB, and muon veto wall.

As shown in Fig. 5.9, antiprotons deposit more energy than pions in the EB. Antiprotons start their shower earlier than do pions, and antiprotons and protons have larger inelastic cross sections than pions. This is illustrated in Fig. 5.10, which shows that 41% of the pions penetrate the EB without starting a shower versus only

35% for protons. The effective thickness of the EB is thus $1.05\lambda_{\text{int}}$ for protons and $0.89\lambda_{\text{int}}$ for pions. Therefore, a larger fraction of the antiproton energy is deposited in the EB.

On the other hand, although protons start their showers as early as antiprotons, they deposit less energy in the EB due to baryon number conservation. Proton-induced showers should contain a baryon in the final state that limits π^0 production.

5.2.4 The Response to "Early" and "Late" Pions

The EB and HB are non-compensating calorimeters with different e/h ratios and the HB compensates better than the EB. In order to study the effects of the very different e/h values of the EB and HB, we subdivide our pion event samples into "early" and "late" starting showers. Pions that constitute the *mip* peak in the EB signal distribution are distinguished as the late showering pions. These pions deposit a larger fraction of their energy in the HB, leaving a *mip* signal in the EB. The rest of the pions are the ones that deposit most of their energy in the EB because they start their showers early in the EB.

Fig. 5.11 shows the calorimeter response to these two classes of pions together with the overall pion response. The response is not shown for the late events below the 5 GeV/c point because the *mip* peak was not clearly resolved in the EB signal distribution for them. The late showering pions have a higher response than other pions because they deposit most of their energy in the HB, and their response is determined by the more compensating HB calorimeter. Early showers have a lower response than other pions because the EB is less compensating. The discrepancy between the early and the late showers reflect the different e/h values of the calorimeters.

It is important to note that pion response is observed to increase in the reverse direction at low energies for early developing showers (see Fig. 5.11). The minimum response is observed at 4 GeV, and at lower energies the response increases. A similar effect was observed by the ZEUS Collaboration [40], which also saw the response of their uranium/scintillator calorimeter increase for energies below 5 GeV. The ex-

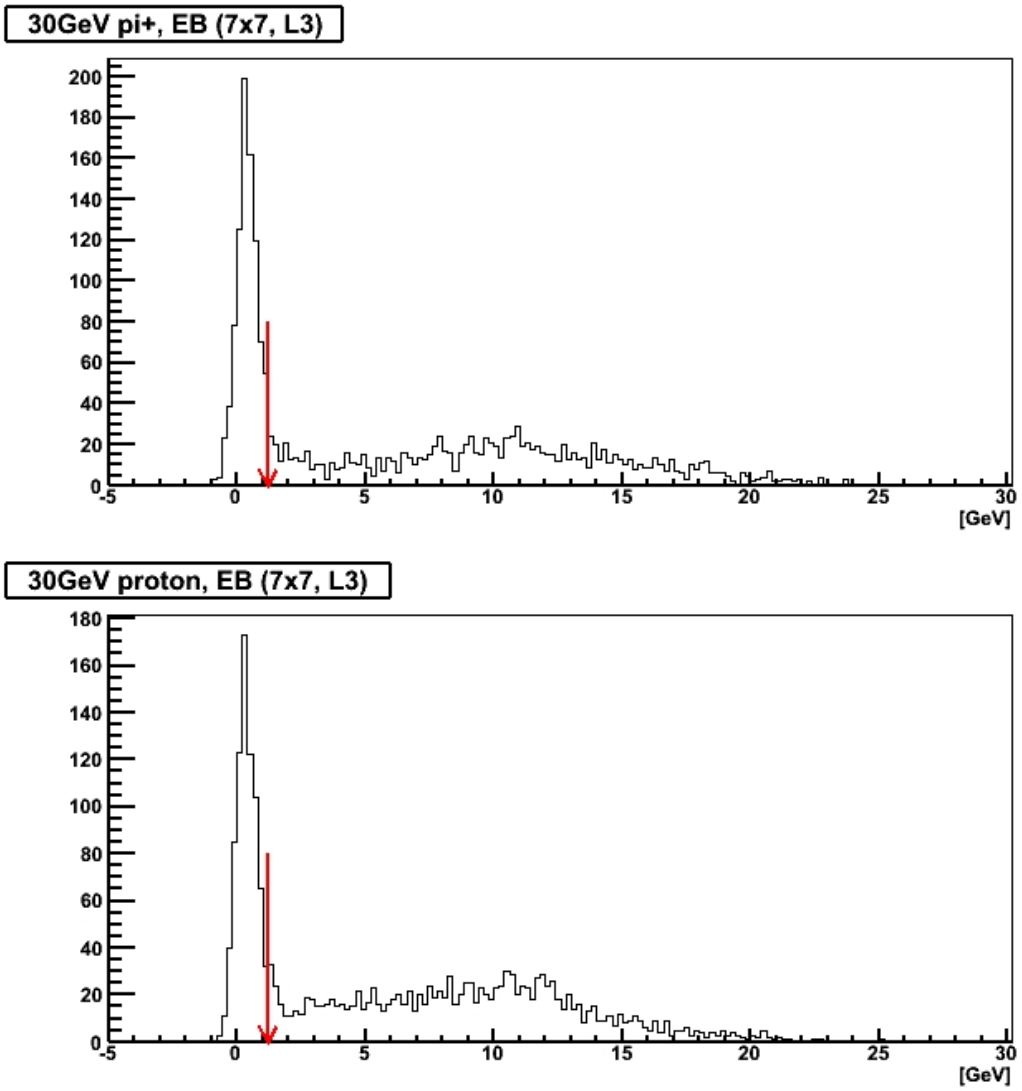

Figure 5.10: The signal distributions from the EB are shown for 30 GeV/c pions (top) and protons (bottom). The arrow indicates where the cut is applied (1.2 GeV) to separate the penetrating pions and protons from the interacting ones. Forty-one percent of the pions are penetrating or deposit energy in the EB that is consistent with a *mip* signal. However, only 35% of protons deposit comparable energy.

planation for this phenomenon is that particles range out at lower energies without inducing any nuclear reaction. The calorimeter will respond to such non-interacting particles in the same way as it responds to muons. Below 2 GeV, where all such particles are completely stopped in the calorimeter, the response is equal to that of

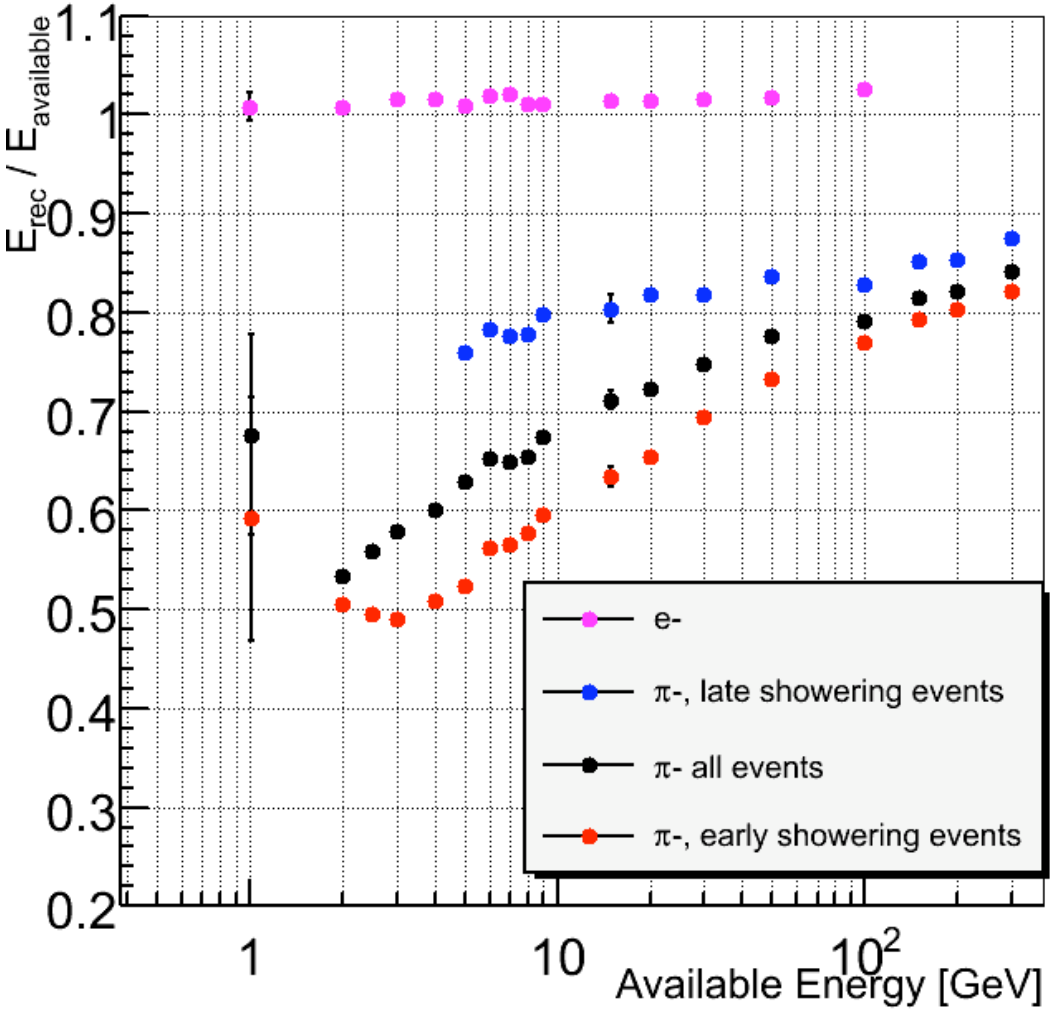

Figure 5.11: The response of the combined calorimeters is shown against the available energy for pions and electrons. The marked difference in response for the early and late developing showers initiated by pions is discussed in the text.

electrons in the EB and even larger than that (by a factor *mip/e*) in the HB.

5.2.5 The Raw Energy Resolution

The raw energy resolution of the combined CMS calorimeter system is shown in Fig. 5.12. Black circles represent the energy resolution for all negatively-charged pions. As explained in the previous section, we divide our pion sample into early and

late showering categories and compute energy resolutions based on the *rms* and mean values of these distributions. Early showering events that deposit a good fraction of their energy in the EB give markedly better energy resolution at low energies compared to all events. As the energy increases, the difference in energy resolution between the early and late developing showers is reduced except when the leakage fluctuations for the late developing showers degrade the resolution at the highest energies. Addition of the MVW signal improves the resolution at a few percent level but does not fully recover it.

5.3 The Calorimeter Response High Energy Jets

Here, I present the computed CMS calorimeter response to jets using the test beam data. The jet response is defined as the average calorimeter signal per unit energy, normalized to 1 for electrons, as in Section. 5.2.2. I first generate PYTHIA jets and replaced the stable particles in a jet by the test beam particles, thereby constructing the calorimeter signal for the jet. Repeating this procedure for many iterations, I derive the average calorimeter signal per unit energy, based purely on the test beam data. I report the jet response in a wide jet energy range: 10 GeV to 4 TeV.

Section 5.3.1 presents the Monte Carlo jet data and their analyses. In Section 5.3.2, the detailed procedure of the jet reconstruction is described. I compare the data based jet response to that of the CMSSW in Section 5.3.3. Finally, I use data to reconstruct and correct the jets in the Z' example ($Z' \rightarrow jj$).

5.3.1 Monte Carlo Jet Data

We simulate six samples of QCD jet events within transverse momentum ranges: $120-170$, $380-470$, $800-1000$, $1400-1800$, $2200-2600$, and $3000-3500$ GeV/c, using CMSSW_1_2_0, producing 1600 events from each P_T range. A midpoint cone jet algorithm with $R = 0.5$ is used to reconstruct jets at the particle level. We require jets in the central region, ($|\eta| < 1.3$), and reject low P_T jets (< 10 GeV/c). The total number of jets is $32,749$.

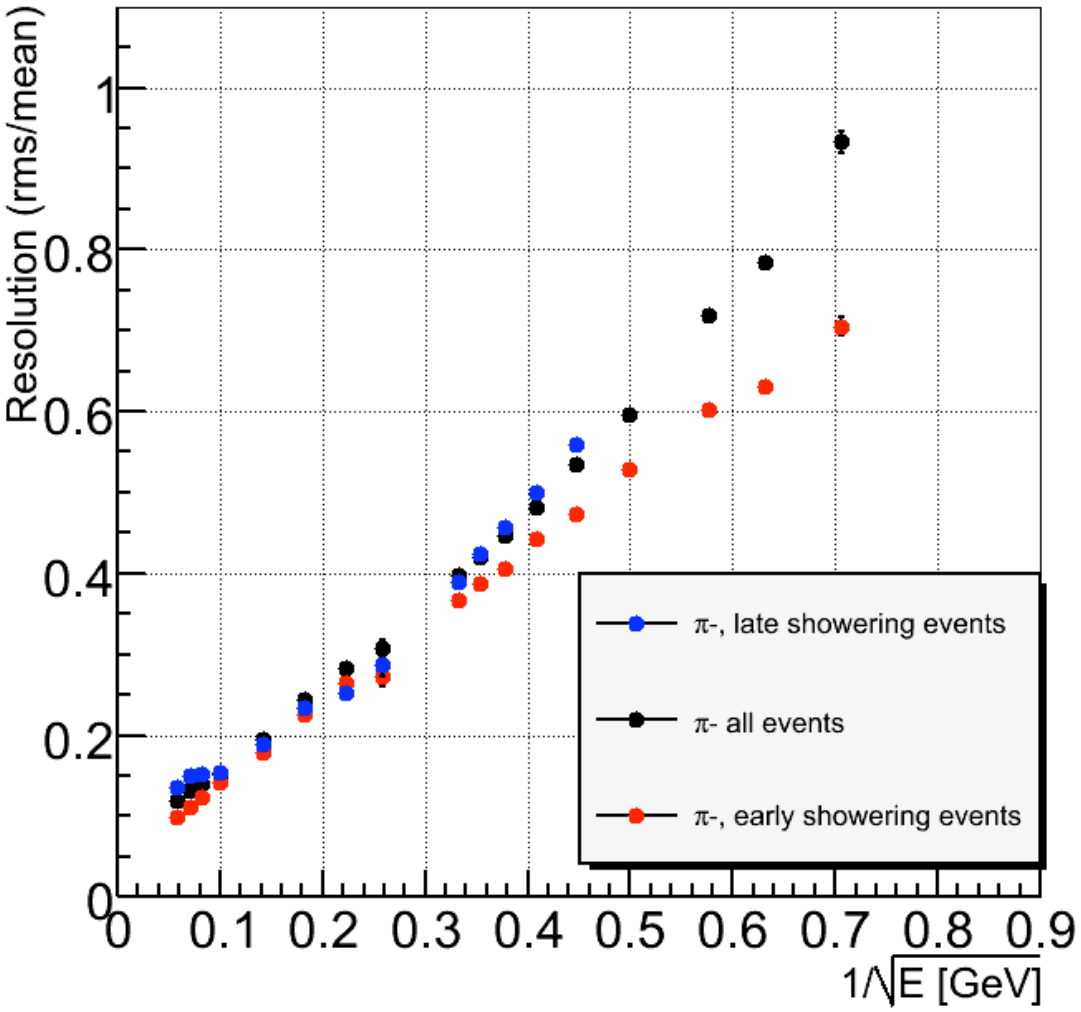

Figure 5.12: The raw energy resolution of the combined CMS calorimeters for negatively charged pions based on the test beam data in 2006 is shown above. Full circles represent data from all pions that pass the event selection criteria. The full and open triangles indicate early and late showering events in the calorimeter (see text for details).

Fig. 5.13 displays the average fraction of particle types in a jet. The stable particles that make the jets are mostly photons (44%), which come from π^0 decays, and charged pions (37%). The rest are kaons (5%), neutrons (3%), protons (3%), neutral kaons (2%), and others comprising less than 1%.

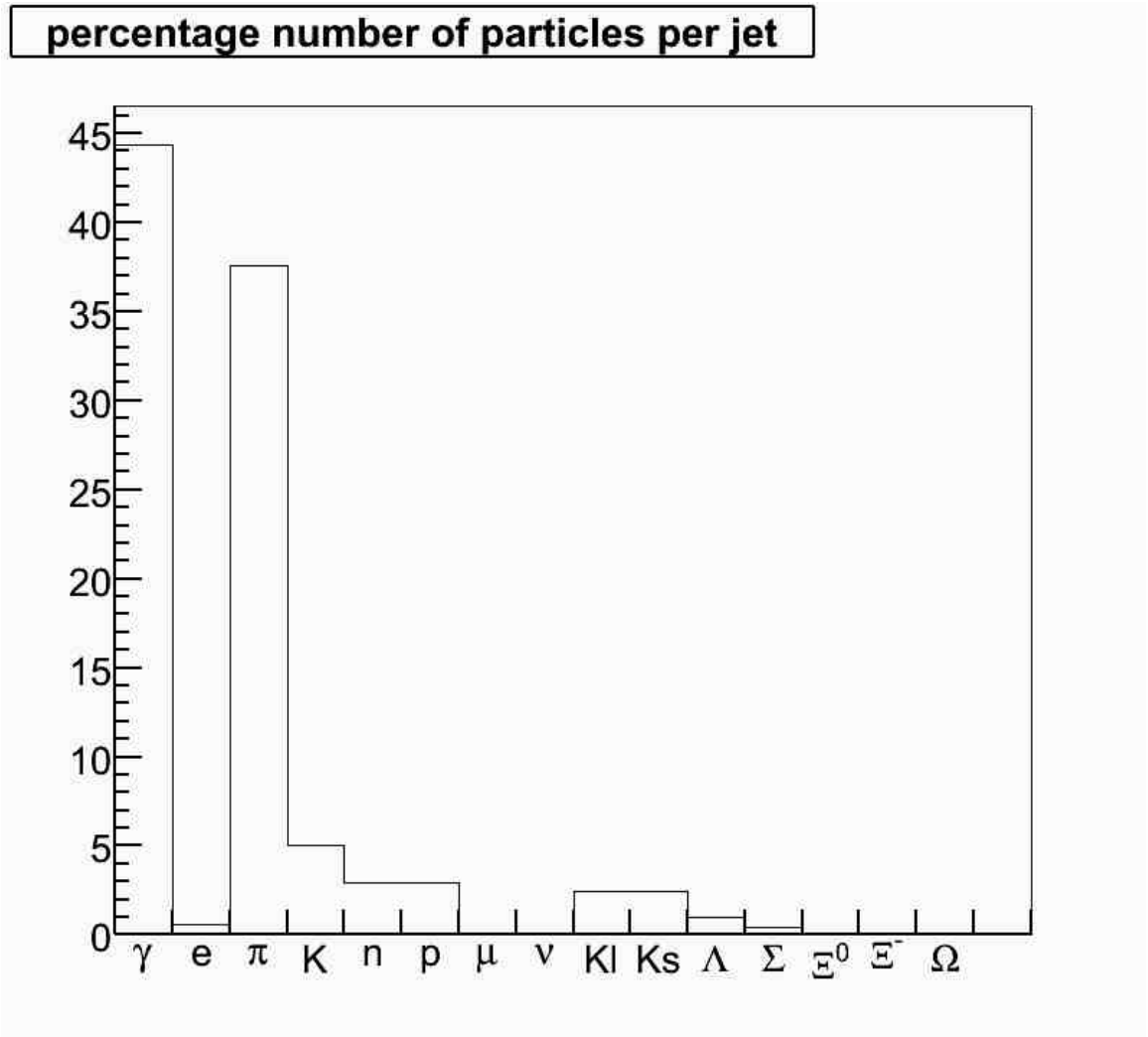

Figure 5.13: The average percentage of stable particles in a jet is shown.

5.3.2 The Response of the CMS Combined Calorimeters to Jets

To obtain the calorimeter response to a Monte Carlo jet, we pursue the following procedure: For each stable particle in a jet, we look for the same particle in the test beam database with the same available energy. Electrons, pions, kaons, protons, antiprotons, and muons were experimentally studied in 2006 and are available in the database [37]. If the jet particle does not exist in the database, we select a beam particle that approximates the particle. For example, a photon in a Monte Carlo jet is replaced by an electron. An antiparticle is replaced by an antiproton. Table 5.1

shows this particle selection. Although the replacement of particles that do not exist in the test beam database is approximate, our jet reconstruction results are insensitive to this procedure because the fraction of these particles is less than 5% in a jet.

Particle	**Replaced by**
e^+ or e^-	e^-
π^+ or π^-	π^{+-}
p	p
$\bar{p}$	$\bar{p}$
K^+ or K^-	K^{+-}
$\mu^\pm$	if ($p < 5$ GeV/c) μ, else $E_{mip} = 2.75$ GeV
γ	e^-
n	p
$\bar{n}$	$\bar{p}$
${K_L}^0$	K^+
${K_S}^0$	π^-
$\Sigma^\pm$	$\pi^\pm$
$\Omega^\pm$	$\pi^\pm$
Λ^0	π^-
$\bar{\Lambda}^0$	$\bar{p}$
Ξ^0	π^-
$\bar{\Xi}^0$	$\bar{p}$
Ξ^-	π^-
$\bar{\Xi}^-$	$\bar{p}$
$\nu^\pm$	0

Table 5.1: Replacement of various jet particles with the available TB particles is shown.

If the available energy of the jet particle exactly matches the energy of the corresponding test beam particle, we pick a random beam event from the database. If the available energy of the jet particle does not match any energy points in the test beam database, we use the nearest energy point and interpolate. If the particle in a jet exceeds the maximum energy for the corresponding test beam particle, we extrapolate. The extrapolated response is assumed to scale as $1 - (\frac{E}{E_0})^{m-1}$ [41] where E is the available energy; E_0 and m are parameters obtained from the fit, and they are different for each particle. The number of such cases is very few. The maximum momenta for electrons and pions in the test beam are 100 and 300 GeV/c respec-

tively. Particle momenta are rarely greater than these values in the jet energy region from 10 GeV to 4 TeV. In the end, we sum the calorimeter signal of each jet particle to obtain the combined calorimeter signal of the corresponding jet. This procedure is repeated 1000 times to obtain an average signal to a particular jet.

Fig. 5.14 shows the calorimeter signal distribution for a 100 GeV Monte Carlo jet after it is reconstructed 1000 times using the test beam data. The mean value of the distribution is ($\sim$ 82 GeV). The width of the distribution reflects the energy resolution of the entire calorimetry system, and several phenomena contribute to this width. For example, the calorimeter response is higher for a leading charged pion if it showers in the HB as opposed to in the EB. The EB ($PbWO_4$) is highly non-compensating, whereas the HB (scintillator+brass sandwich) is comparatively less so [21, 23]. In addition, the calorimeter response depends on the particle types, especially at low energies ($<$ 10 GeV), *e.g.* the π^+ response is larger than π^- due to charge exchange reaction, and the response to pions is systematically higher than that of protons [37].

The calorimeter resolution (RMS/Mean) for a 100 GeV jet is measured to be $\sim$ 8% (See Fig. 5.14). On the other hand, it is $\sim$ 15% for a 100 GeV negatively-charged pion (See Fig. 5.5). The worse resolution for pions is due to the large fluctuations in the energy sharing between electromagnetic and hadronic calorimeters for pions compared to that of jets.

The average calorimeter signal per unit energy as a function MC jet energy for 32,749 jets is plotted in Fig. 5.15. The error bars are the RMS of the calorimeter signal distribution for each jet. Fig. 5.16 is obtained by rebinning the data in Fig. 5.15. This is the most significant result of this study, and it shows the CMS calorimeters response to jets between 10 GeV and 4 TeV as a function of the Monte Carlo. As observed, the jet response increases from 0.68 at 20 GeV up to 0.86 at 4 TeV.

The measured calorimeter response to hadrons increases below 2 GeV [37]. The increase in the jet response below 20 GeV (see Fig. 5.16) is primarily due to this phenomenon. In 10-20 GeV jets, 76% of the particles are $<$ 2 GeV. In 300-500 GeV

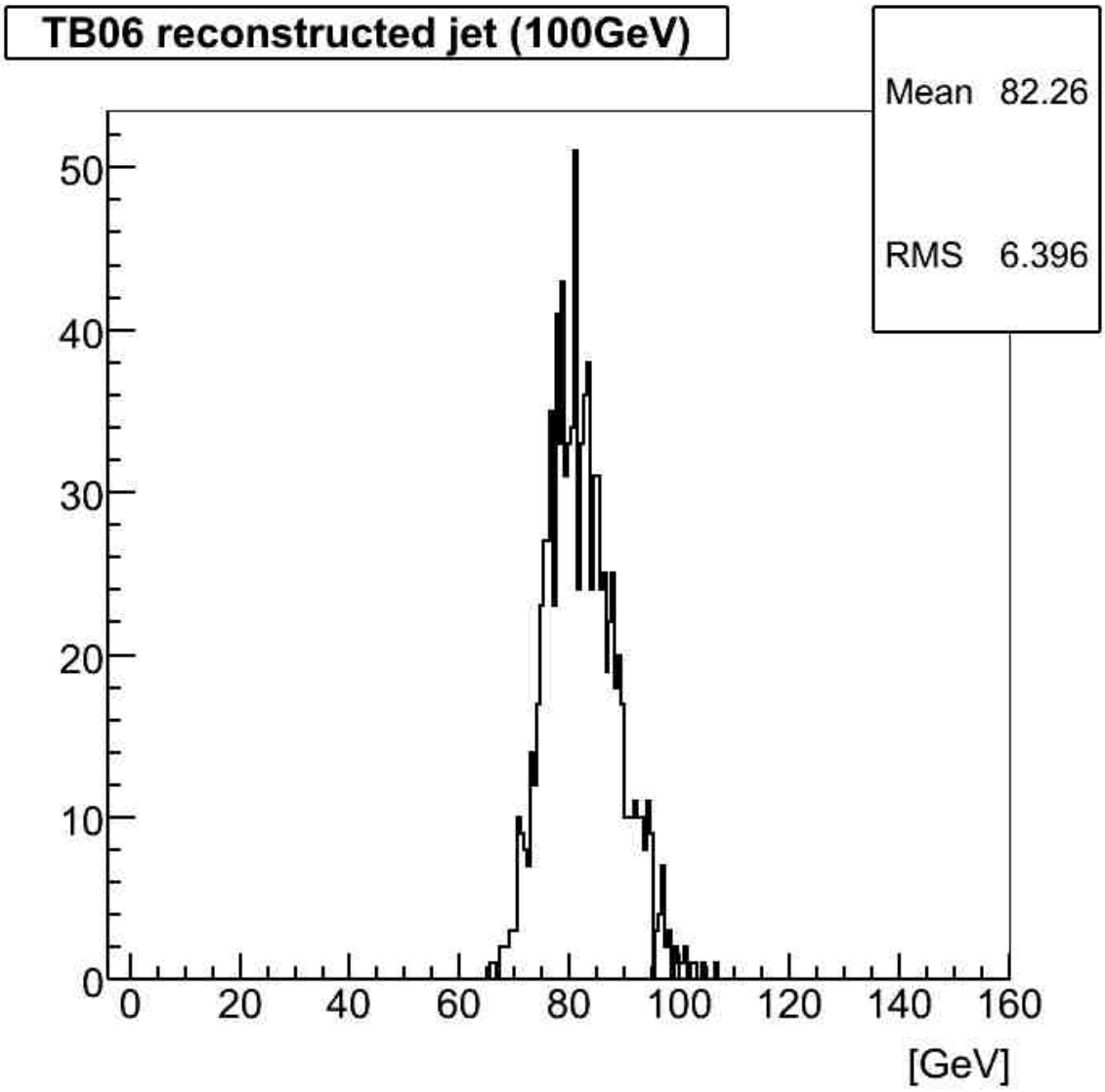

Figure 5.14: The distribution of calorimeter signals for a 100 GeV Monte Carlo jet is shown.

jets, this fraction decreases to 36%.

The jet response curve shown in Fig. 5.16 is the basis of our jet energy correction. The jet energy is obtained by multiplying the measured signals (converted to GeV on the basis of the electron calibration constants) by the inverted jet response. We verified the validity of this approach by reconstructing the jet energy on the basis of the measured signals of the individual jet fragments, converting these signals to energy units and adding up these energies. For the conversion of the particle signals to

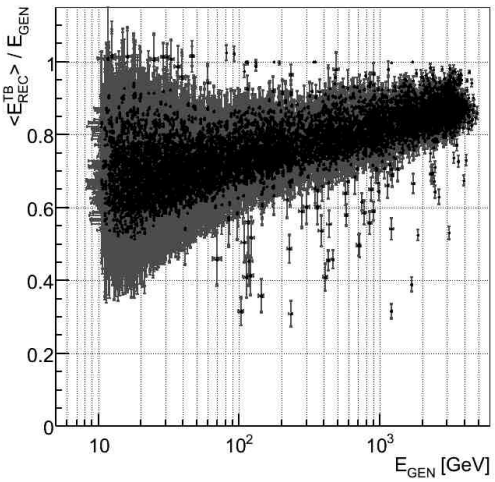

Figure 5.15: The test beam based calorimeter response to jets is shown as a function of generated jet energy.

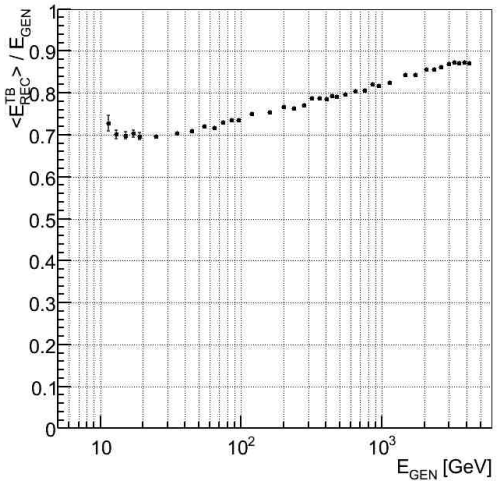

Figure 5.16: The average calorimeter response to jets as a function of generated jet energy is obtained after rebinning the left figure in wider energy bins. The data points in the same bin are averaged.

particle energies, we used a parameterization of the form $1-(\frac{E}{E_0})^{m-1}$ [41], which gives a reasonable description of the energy dependence of the single-hadron response down to $\sim$ 2 GeV. The values of E_0 and m were determined from the fits to the experimental data (see Fig. 5.17). For energies below 2 GeV where the fits did not describe the experimental data well, the correction factors were found by interpolating between the measured data points. The results of this procedure are shown in Fig. 5.18. The jet energy is well reconstructed down to $\sim$ 20 GeV. Small ($\sim$ 2%) deviations at lower energies are due to the large contribution of very soft jet fragments.

We use the curve in Fig. 5.16 to correct jet energy. The black histogram in Fig. 5.19 is the signal distribution of 100 GeV Monte Carlo jet after it was reconstructed using test beam data. The red histogram shows it after it was corrected using test beam based jet energy correction. As observed, the mean value of the distribution shifts to

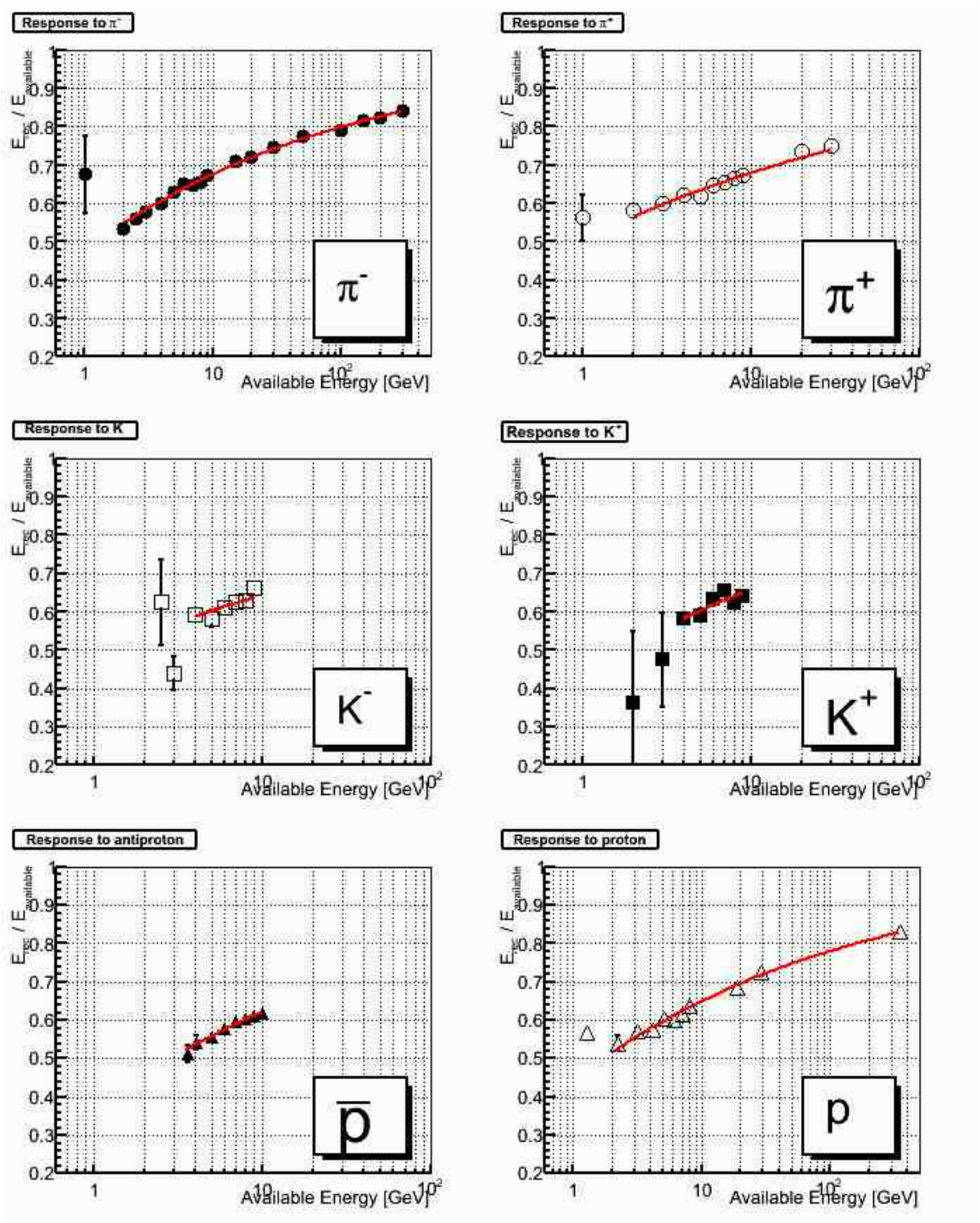

Figure 5.17: Calorimeter response to beam particles is fitted with parametrization of the form $1-(\frac{E}{E_0})^{m-1}$ [41]. Parameters E_0 and m are obtained from the fits and are different for each particle type.

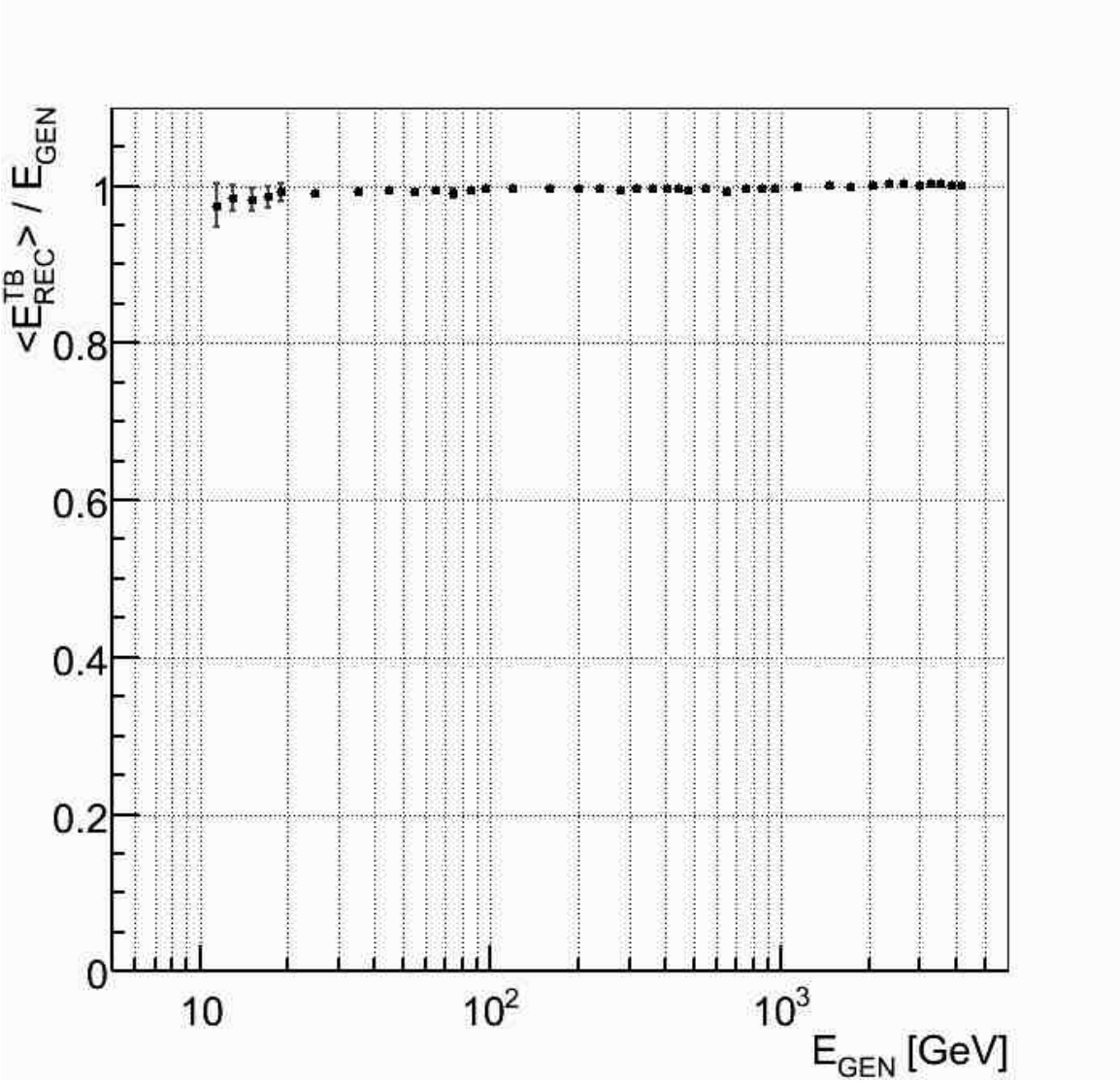

Figure 5.18: The average calorimeter response to jets after the correction scheme is applied to the test beam particles as described in the text. The linear response at one confirms the validity of our jet reconstruction based on test beam data.

$\sim$ 100 GeV, as it should.

The comparison of jet and pion responses is displayed in Fig. 5.20. The calorimeter response to jets is lower than that of single pions down to 10 GeV. Typically, a large fraction of jet energy ($\sim$ 25%) is carried by a single leading particle, and the rest of the energy is shared among many others, thereby reducing the amount of energy per particle. The calorimeter response to hadrons drops from $\sim$ 0.85 at 300 GeV

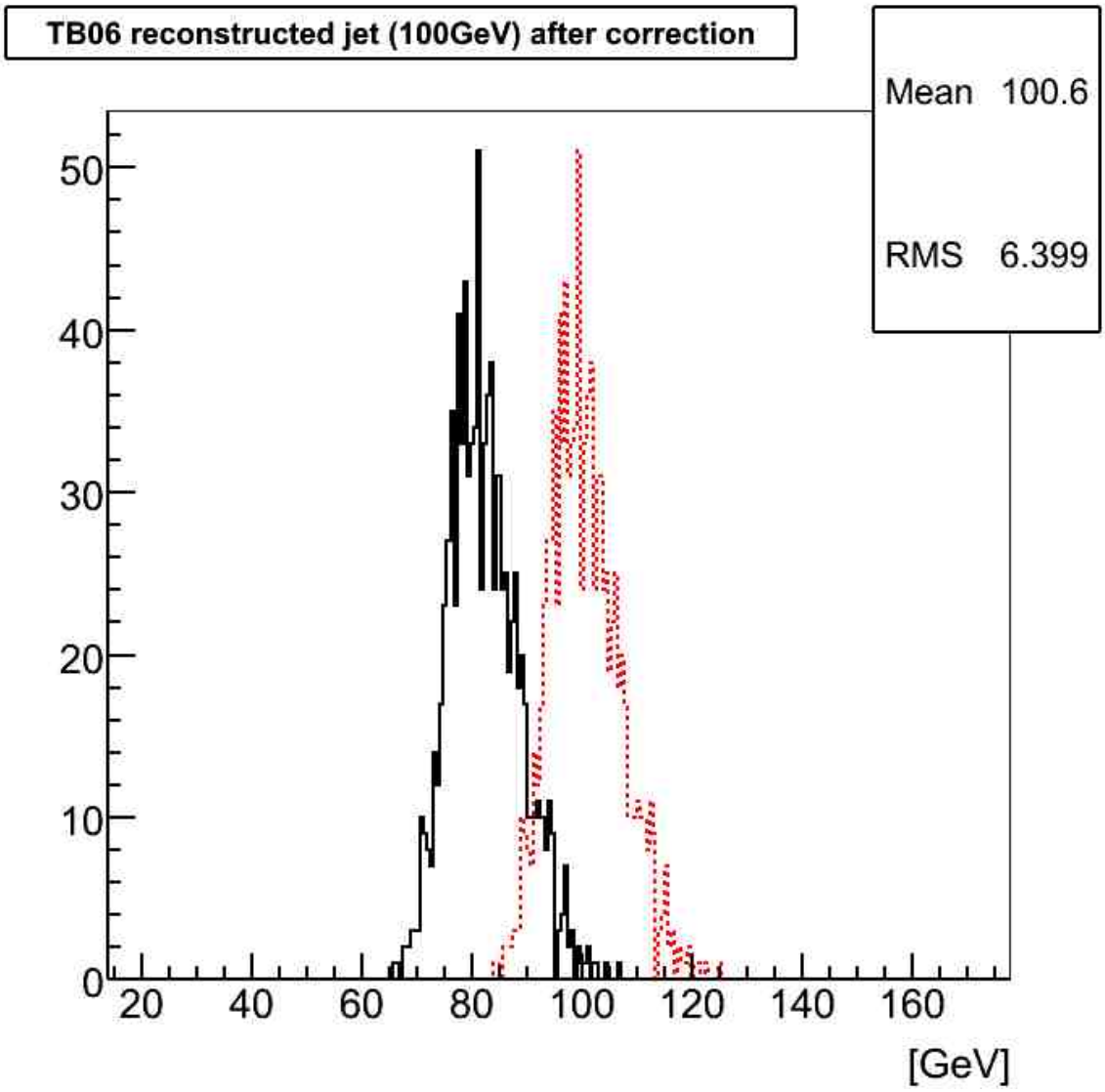

Figure 5.19: The calorimeter signal distribution for a 100 GeV MC jet (solid), as shown in Fig. 5.14, is corrected by the test beam based jet energy correction curve (dashed).

to $\sim$ 0.55 at 2 GeV. Thus, there is a natural suppression of response for the lower energy particles in a jet. This induces a diminished response to jets when contrasted with single pions, as shown in Fig. 5.20.

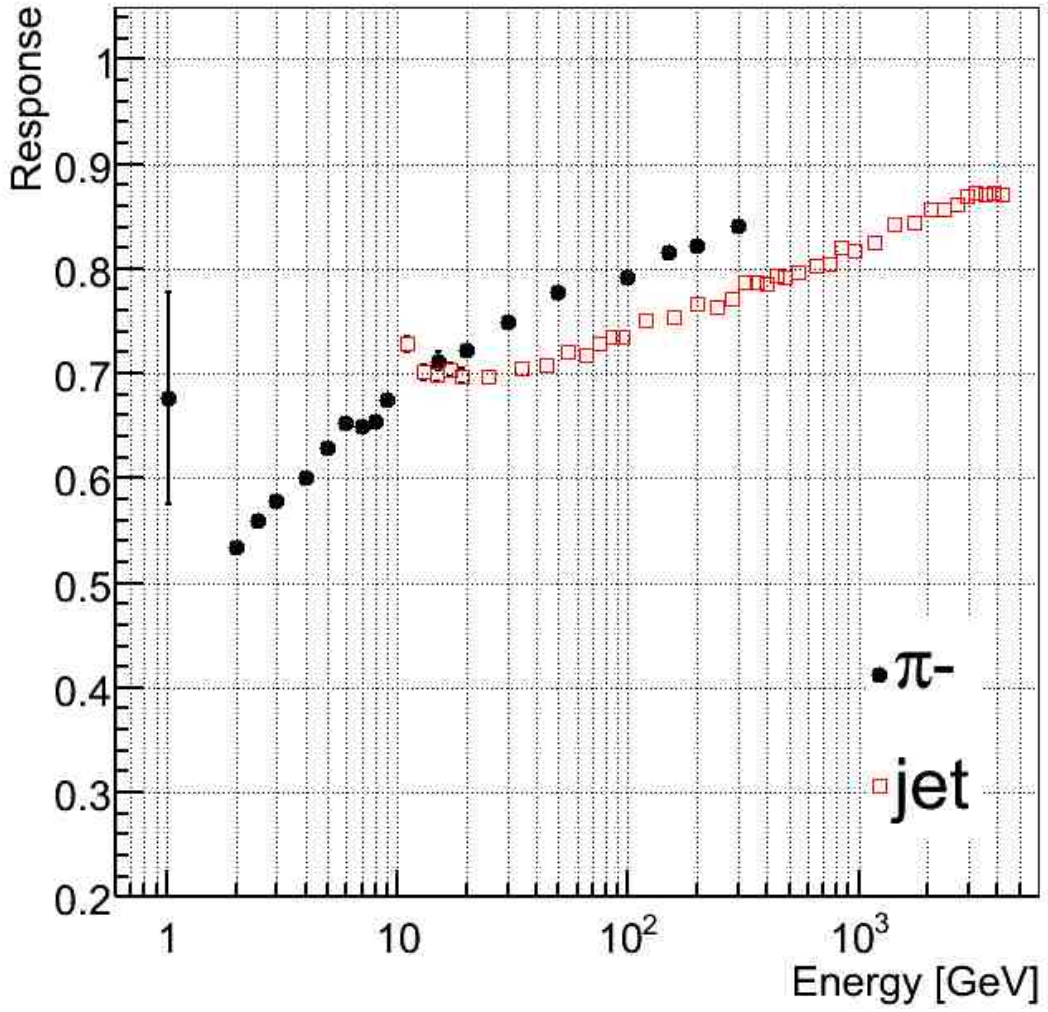

Figure 5.20: The jet response is lower than the charged pion response because a jet consists of mostly low energy (< 10 GeV) particles, and the low calorimeter response to these particles reduces the jet response with respect to charged pions.

5.3.3 Test Beam Based Jets *vs* CMSSW Jets

We use the same dataset of the generated jets that we used for the reconstruction of the test beam based jets to compute the jet response in CMSSW. We define the CMSSW jet response as the ratio of transverse energy of a calorimeter jet (CaloJet) to the transverse energy of the corresponding generated jet (GenJet). Fig. 5.21.a contrasts jet responses from the test beam and the simulation. The jet response from

the test beam is higher than the one from the simulation. The difference, about 50% at low and 5% at very high energy, is caused by the different conditions of the test beam setup and the CMSSW default settings.

1. There is a 4-T magnetic field in the simulation whereas there is none in the test beam. Fig. 5.21.b shows that removing the magnetic field has a 20% effect on simulated jet response at low energy and a few percent effect at high. This is expected because the magnetic field bends the particles, possibly causing them to stray outside of the jet cone. Its effect is larger at low energy jets since it bends the low momenta particles more strongly than the high momenta ones.

2. Contrary to the test beam, the simulation incorporates the full CMS tracker which introduces mass in front of the calorimeters. Fig. 5.21.c shows less than a 5% effect on the simulated jet response after the tracker material is removed in the simulation.

3. The simulation applies thresholds for calorimeter cells and towers to suppress the noise contribution. These thresholds require the energy sum of 5×5 EB cells to be greater than 0.2 GeV, and each HB tower energy to be greater than 0.9 GeV (Scheme B) [36]. We apply the same cell and tower thresholds to the test beam data as in the simulation code. Fig. 5.21.d shows that noise thresholds have about a 12% effect on the test beam based jet response. Applying thresholds to the calorimeter cells and towers reduces the signal collected from them and in turn reduces the jet response.

Fig. 5.21.e shows the comparison of the jet response distributions after bringing the conditions closer in the test beam and simulation. The agreement is good for 100 GeV and above. The jet response from the simulation is still lower at lower jet energies. The difference between them is about 11% when the jet energy goes down 50 GeV and about 25% at 10 GeV.

The increasing disagreement at low energies between the jet responses from the test beam and the simulation needs to be further investigated. A comparative study of the test beam and the simulation may help expose the origins of the disagreements.

5.3.4 The Application of the Test Beam Based Jet Response

We test the energy correction technique based on the test beam data on a physics process that includes jets. We use dijet data from 700 GeV/c^2 Z' decay produced with CMSSW_1_2_0. We use $|\eta| < 1$ cut for the two leading jets, which are the jets with the highest transverse momentum in an event. Midpoint cone jet algorithm with $R = 0.5$ is used to reconstruct jets. Fig. 5.22.a shows the dijet mass distribution for $M_{Z'} = 0.7$ TeV at the generated level. Fig. 5.22.b shows the dijet mass distribution when the jets are replaced by the jets constructed from the test beam data. Fig. 5.22.c shows the dijet mass distribution after the jet energies are corrected by test beam based jet energy corrections. As seen, the mean of the dijet mass distribution is 607 GeV at the generated level. After the jets are reconstructed from the test beam data, the mean is 478 GeV. Finally, after the jet energies are corrected by the test beam based jet energy correction, the mean of the distribution becomes 613 GeV, which is very close to the mean value in the generated dijet distribution. We conclude that the corrections based on the test beam work well, as expected.

5.3.5 Summary

We evaluate the CMS central calorimeter response to Monte Carlo jets (10 GeV to 4 TeV), using the 2006 test beam data. We compare the data based jet response with that of CMSSW_1_2_0. We observe a good agreement for jets with energy greater than 100 GeV. The test beam based jet response is higher than the CMSSW based one at low energies. We propose that a comparative study of the CMSSW response and test beam response to single particles may help resolve this disagreement. Lastly, we present the reconstruction and correction of dijet mass distribution of Z' resonance from the test beam based jets.

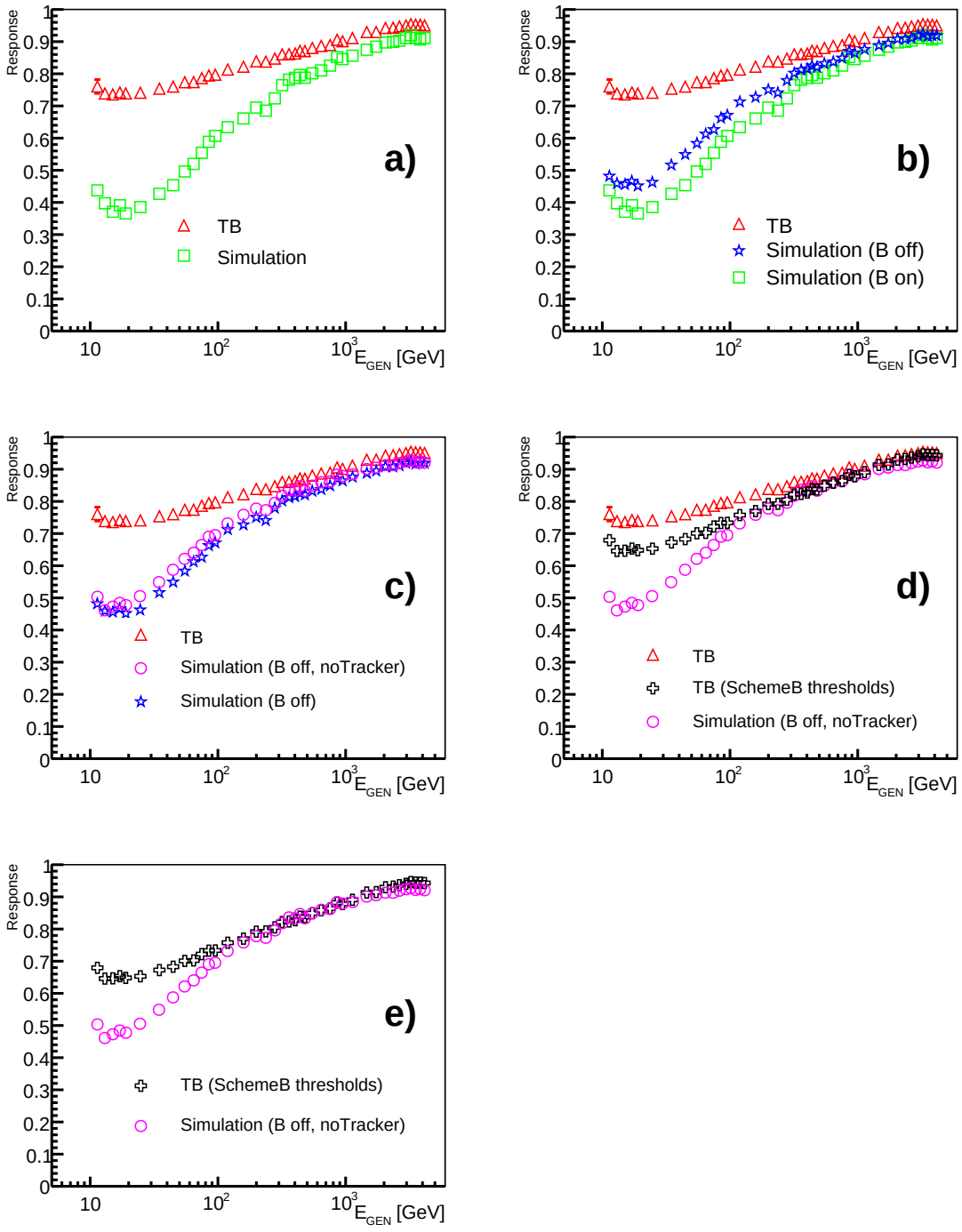

Figure 5.21: The jet response from the test beam is compared with the jet response from the CMSSW.

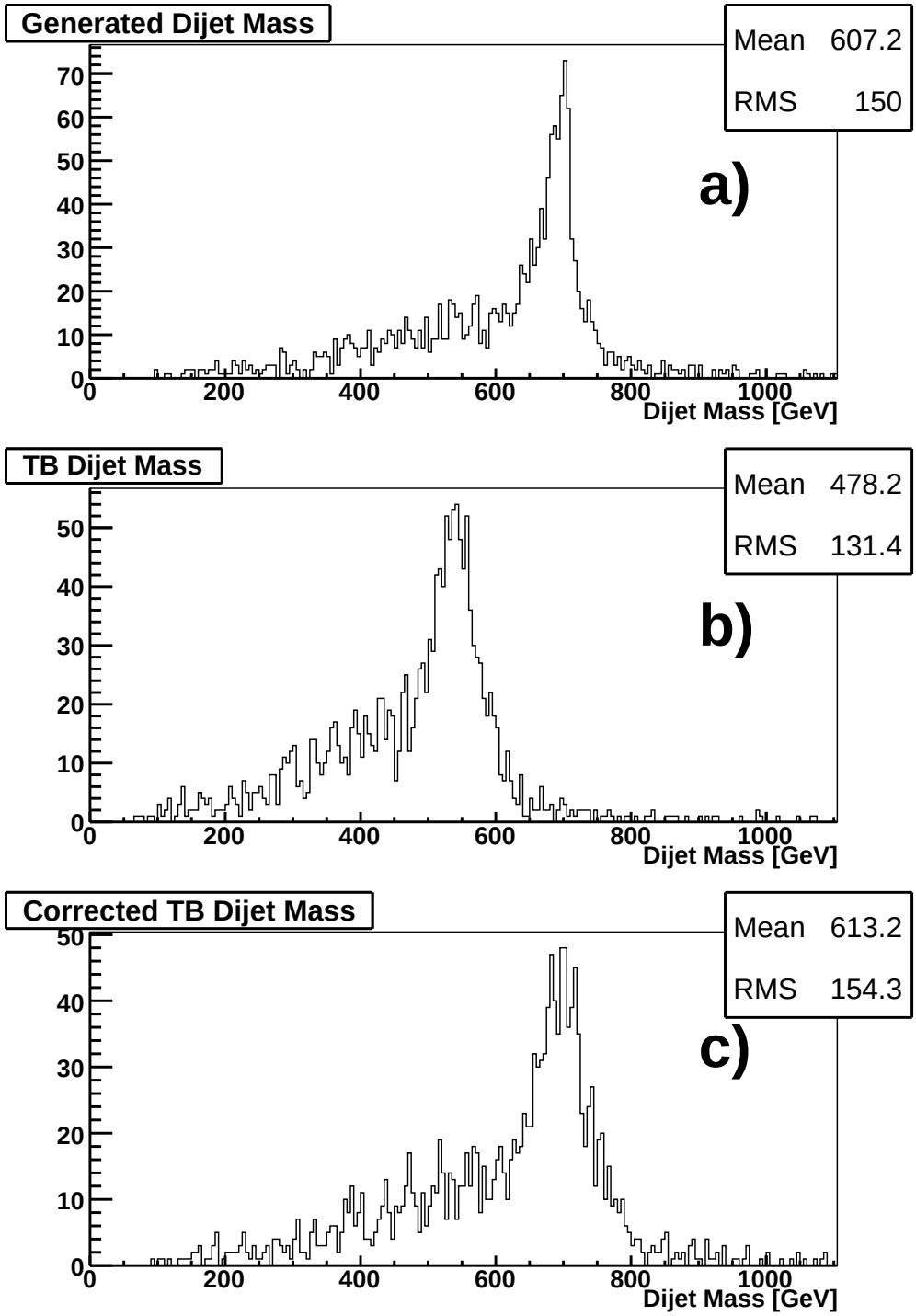

Figure 5.22: The top plot (a) shows the dijet mass distribution of $Z'(700\,\mathrm{GeV})$ at the generated level. The middle plot (b) displays it after the jets are reconstructed using test beam data. The bottom plot (c) shows the invariant mass peak after all corrections.

CHAPTER 6
SUMMARY

The CMS will start taking data in the second half of 2008. It will probe TeV energy scale for new physics beyond the Standard Model. I present the study of searching for new resonances that decay to two jets. My goal is to perform a generic search that will encompass all the narrow resonances. I present the cross section for a narrow dijet resonance that CMS can expect to discover at 5σ significance or to exclude at a 95% confidence level for integrated luminosities of 100 pb^{-1}, 1 $\text{fb}^{-1}$and 10 fb^{-1}.

I compare the exclusion and discovery cross section limits with the resonance cross sections predicted by the theoretical models. I determine the mass region for the exclusion or discovery of these particles. I find that a 5σ discovery of a multi-TeV dijet resonance is possible for an axigluon and excited quark produced via the color interaction or for the E_6 diquarks produced from the valence quarks of each proton because of their large cross sections. However, a 5σ discovery cannot be projected with confidence for a W' or Z' produced by the weak force and for the Randall-Sundrum produced by the gravitational force due to their low cross sections. On the other hand, 95% CL exclusion mass regions can be measured for all resonances at high luminosities.

I also present the analysis results of the 2006 combined calorimeter test beam data. I measure the CMS barrel calorimeters' response to a variety of beam particles in a wide momenta range from 1 to 350 GeV/c. Using single particle response information, I develop a novel algorithm to compute the CMS calorimeter response to high energy jets. I obtain jet energy correction based on the test beam data. The results are compared with the corrections obtained from Monte Carlo.

BIBLIOGRAPHY

[1] K. Gumus, N. Akchurin, S. Esen and R. M. Harris, *CMS Sensitivity to Dijet Resonances*, CMS NOTE-2006/070.

[2] F. Abe et al. Phys. Rev. D **55**, 5263 (1997).

[3] J. Pumplin et al. JHEP, **07**, 012 (2002).

[4] LHAPDF code available online at `http://vircol.fnal.gov/`.

[5] P. Frampton and S. Glashow, Phys. Lett. B **190**, 157 (1987).

[6] G. Katsilieris, O. Korakiantitis and S. Vlassopulos, Phys. Lett. B **288**, 221 (1992).

[7] J. Bagger, C. Schmidt and S. King, Phys. Rev. D **37**, 1188 (1988).

[8] E. Simmons, Phys. Rev. D **55**, 1678 (1997).

[9] J. L. Hewett and T. G. Rizzo, Phys. Rept. **183**, 193 (1989).

[10] U. Baur, I. Hinchliffe and D. Zeppenfeld, Int. J. Mod. Phys. A **2**, 1285 (1987), Fermilab-Conf-87-102-T; U. Baur, M. Spira and P. M. Zerwas, Phys. Rev. D **42**, 815 (1990).

[11] Thomas G. Rizzo, Phys. Rev. D **48**, 4470 (1993).

[12] Kenneth Lane and Stephen Mrenna, Phys. Rev. D **67**, 115011 (2003).

[13] T. Affolder et al. Phys. Rev. D **61**, 091101 (2000).

[14] E. Eichten, I. Hinchliffe, Kenneth D. Lane and C. Quigg, Rev. Mod. Phys. **56**, 579 (1984).

[15] Review of fundamental particles can be found at `http://pdg.lbl.gov`.

[16] L. Randall and R. Sundrum, Phys. Rev. Lett. **83**, 3370 (1999); Expressions for calculating the Randall-Sundrum Graviton cross section were determined from J. Bijnens, P. Eerola, M. Maul, A. Mansson, T. Sjostrand, Phys. Lett. B **503**, 341 (2001).

[17] O. Bruening, P. Collier, P. Lebrun, S. Myers, R. Ostojic, J. Poole and P. Proudlock, *LHC Design Report*, CERN-2004-003 (2004), available online at `http://ab-div.web.cern.ch/ab-div/Publications/LHC-DesignReport.html`.

[18] J. M. Campbell, J. W. Huston and W. J. Stirling, Rep. Prog. Phys. **70**, 89 (2007).

[19] CMS collaboration, `http://cmsinfo.cern.ch`.

[20] CMS Collaboration, *The Tracker Project Technical Design Report*, CERN/LHCC 1998-006 (1998).

[21] CMS Collaboration, *ECAL Technical Design Report*, CERN/LHCC 1997-033 (1997).

[22] S. Abdullin et al. Eur. Phys. J. C, **53**, 139 (2008).

[23] CMS Collaboration, *The Hadron Calorimeter Technical Design Report*, CERN/LHCC 1997-031 (1997).

[24] CMS Collaboration, *The Magnet Project, Technical Design Report*, CERN/LHCC 1997-10 (1997).

[25] CMS Collaboration, *The Muon Project, Technical Design Report*, CERN/LHCC 1997-32 (1997).

[26] CMS Collaboration, *Level-1 Trigger Technical Design Report*, CERN/LHCC 2000-038 (2000).

[27] CMS Collaboration, *DAQ and High-Level Trigger Technical Design Report*, CERN/LHCC 2002-026 (2002).

[28] CMS Collaboration, J. Phys. G: Nucl. Part. Phys. **34**, 995 (2007).

[29] V. M. Abazov et al. Phys. Rev. D **69**, 111101 (2004).

[30] A. Heister, O. Kodolova, V. Konoplianikov, S. Petrushanko, J. Rohlf, C. Tully and A. Ulyanov, *Jet Reconstruction and Performance in the CMS Detector*, CMS NOTE-2005/005.

[31] S. Esen and R. M. Harris, *Jet Triggers and Dijet Mass*, CMS NOTE-2006/069.

[32] B. Abbott et al. Phys. Rev. Lett. **82**, 2457 (1999).

[33] The Bayesian technique with a binned likelihood is discussed in the Review of Particle Physics, Phys. Lett. B592, 1-1110, (2004). The statistics discussion is available online at `http://pdg.lbl.gov/2005/reviews/statrpp.pdf` where the relevant pages are 4-5 and 13-15.

[34] A. L. Read, Nucl. Inst. Meth. A, **425**, 357 (1999).

[35] Robert M. Harris, *Discovery Mass Reach for Excited Quarks at Hadron Colliders*, published in "Snowmass 1996, New directions for high-energy physics", FERMILAB-CONF-96-285-E.

[36] CMS Collaboration, *CMS Physics Technical Design Report Volume 1*, CERN/LHCC 2006-001 (2006).

[37] N. Akchurin et al. *The Response of CMS Combined Calorimeters to Single Hadrons, Electrons and Muons*, CMS NOTE-2007/012.

[38] S. Abdullin et al. *The CMS Barrel Calorimeter Response to Particle Beams from 2 to 350* GeV/c, Euro. Phys. J. C, (to be published).

[39] N. Akchurin et al. *The Response of the CMS Barrel Calorimeters to Jets*, (to be published as CMS NOTE).

[40] A. Andresen et al. Nucl. Instr. and Meth. A **290**, 95 (1990).

[41] D.E. Groom in *Proc. Seventh Inter. Conf. on Calorimetry in High Energy Physics, Tucson, Arizona, 2007*, availablev online at `http://calor.pg.infn.it/calor1997/calorimg/friam/Groom.pdf`.